UNIVERSITY OF SOUTHAMPTON

FACULTY OF NATURAL AND ENVIRONMENTAL SCIENCES

SCHOOL OF CHEMISTRY

Nanostructured Palladium Hydride Microelectrodes: from the Potentiometric Mode in SECM to the Measure of Local pH during Carbonation

Mara Serrapede

Thesis for the degree of Doctor of Philosophy

March 2014

UNIVERSITY OF SOUTHAMPTON

ABSTRACT

FACULTY OF NATURAL AND ENVIRONMENTAL SCIENCES
SCHOOL OF CHEMISTRY

Doctor of Philosophy

NANOSTRUCTURED PALLADIUM HYDRIDE ELECTRODES: FROM THE POTENTIOMETRIC MODE IN SECM TO THE MEASURE OF LOCAL PH DURING CARBONATION.

By Mara Serrapede

The detection of local variations of the proton activity is of interest in many fields such as corrosion, sedimentology, biology and electrochemistry. Using nanostructured palladium microelectrodes Imokawa *et al.* fabricated for the first time a reliable and miniaturized sensor with high accuracy and reproducibility of the potentiometric-pH response. In absence of oxygen, the nanostructured palladium hydride tips are sensitive only to the activity of the protons close to their local environment and they have an almost Nernstian theoretical response with a slope of −58.7 mV/pH (25°C) from pH 2 to 14. In the bulk, the lifetime of the palladium hydride sensor is 60 times longer when the solution is saturated with argon than with oxygen. Besides, the open circuit potential (OCP) recorded during the discharge of the hydride is more positive in an oxygenated solution. To unravel the influence of oxygen on the potentiometric response of these tips, we carried out a series of potentiometric and amperometric scanning electrochemical microscopy (SECM) experiments over a range of tip-substrate distances against an inert substrate. Potentiometric SECM experiments in aerated solutions demonstrate that the duration of the hydrogen discharge and tip potential depend on the tip-substrate distance: the closer the tip is to an inert substrate, the longer the lifetime of the sensor is, and the more cathodic the open circuit potentials are. Linear sweep voltammetry (LSV) near the OCP values reveals that the polarization resistance decreases when the tip approaches the substrate. These trends are confirmed by Tafel plots recorded over a range of tip-substrate distances. Potentiometric and amperometric measurements are found to be in good agreement. These results can be analysed in terms of a mixed potential theory as used in corrosion. They reveal that in the potentiometric mode, despite being held at zero current, the tips promote the reduction of oxygen which in turns leads to the rapid discharge of hydrogen from the palladium hydride. The closer the tip is to the substrate, the smaller is the flux of oxygen, the longer is the duration of the discharge and the more negative is the OCP. This dissertation will therefore show that even in a potentiometric SECM experiment where the tip is supposed to be a passive probe, hindered diffusion can affect the tip potential and produce a dependence on the tip-substrate distance. In aerated solutions, a simple correction can be made to bulk experiments. In this study the exceptional potentiometric properties of pH microprobes made with nanostructured palladium hydride microelectrodes are reported to demonstrate their application by monitoring pH variations resulting from a reaction confined in a porous medium. Their properties were validated by detecting pH transients during the carbonation of $Ca(OH)_2$ within a fibrous mesh. Experimental pHs recorded *in situ* were in excellent agreement with theoretical calculations for the CO_2 partial pressures considered. Results also showed that the electrodes were sufficiently sensitive to differentiate between the formation of vaterite and calcite, two polymorphs of $CaCO_3$. These nanostructured microelectrodes are uniquely suited to the determination of pH in highly alkaline solutions, particularly those arising from interfacial reactions at solid and porous surfaces.

List of contents

List of figures

DECLARATION OF AUTHORSHIP

I, Mara Serrapede, declare that the thesis entitled:

“Nanostructured palladium hydride electrodes: from the potentiometric mode in SECM to the measure of local pH during carbonation”

and the work presented in the thesis are both my own, and have been generated by me as the result of my own original research. I confirm that:

§ this work was done wholly or mainly while in candidature for a research degree at this University;

§ where any part of this thesis has previously been submitted for a degree or any other qualification at this University or any other institution, this has been clearly stated;

§ where I have consulted the published work of others, this is always clearly attributed;

§ where I have quoted from the work of others, the source is always given. With the exception of such quotations, this thesis is entirely my own work;

§ I have acknowledged all main sources of help;

§ where the thesis is based on work done by myself jointly with others, I have made clear exactly what was done by others and what I have contributed myself;

§ parts of this work have been published as: Serrapede et al.,” Scanning Electrochemical Microscopy: Using the Potentiometric Mode of SECM To Study the Mixed Potential Arising from Two Independent Redox Processes”, Analytical Chemistry, Vol 85, 2013.

Signed: ………………………………………………………………………..

Date:…………………………………………………………………………

Acknowledgments

I would firstly like to acknowledge my supervisor Dr. Guy Denuault to whom I am immensely grateful for his encouragement through this research and for being one of the kindest people I have met in my all life. I would like to thank him for the helpful discussions we have had in the lab and for the valuable advice he gave to me during the dark periods of this PhD.

I would like to acknowledge the assistance of other people who have contributed their time and expertise. I would especially like to thank Prof. Andrea E. Russell and Prof. Derek Pletcher for their advices and useful discussions. Particular thanks also go to Dr. Thomas Esterle and to Dr. Maciej Sosna who have kept an eye on me since the first day of my PhD.

I would also like to thank the Denuault group members that in these three years have made my time in the lab an enjoyable experience. My thanks go to Gianluca, Nawal, Aziz, Ana, Sam, Leila, Mandeep and Kelly. I am especially grateful to Mandeep and Aziz for their collaboration in acquiring data shown in figure 3.5 and to Gianluca for the nice time spent in millions of experiments relevant for the chapter 5.

Special thanks go to my friends and mates that made this period a great experience of life. My thanks go to Laura, Fivi, Martina, Marta, Clem, Boris, Victor and Rob. I loved their jokes from all around the world.

I would like this opportunity to express my sincere thanks to my parents and family in Italy who have been extremely supportive throughout my entire academic career.

At last, I would say a huge thank to Lorenzo without whom I would not have completed this PhD.

List of symbols

Symbol	Meaning	Unit of measure
a	microdisc radius of electrodes	µm
a_i	activity of the species i	
c_i	concentration of the species i	mol cm^{-3}
d	distance	µm, cm
D_i	diffusion coefficient of the species i	$cm^2\ s^{-1}$
$E_{1/2}$	half wave potential	V
E^{o}	standard redox potential	V
E_{DL}	potential in the double layer capacitance region	V
E_L	potential to load palladium with hydrogen	V
F	Faraday constant (96.485)	C mol^{-1}
f	(i) resonant frequency of a piezoelectric	Hz
	(ii) F/RT	s A J^{-1}
	(iii) fugacity of molecular hydrogen	bar
i_{lim}	limiting current	A
I_s	ionic strength	M
i_T	limiting current recorded by a tip	A
$i_{T\infty}$	limiting current in the bulk recorded by a tip	A
Q_i	charge density of the event i	C cm^{-2}
j_i	current density of the event i	A cm^{-2}
K_i	equilibrium constant of the reaction i	
k_i	rate constant of the reaction i	
n	number of electrons transferred in a redox reaction	
q_a	anodic charge on chronoamperograms and voltammograms	C
q_c	cathodic charge on chronoamperograms and voltammograms	C
R	gas constant (8.314)	J mol^{-1} K^{-1}
R_f	roughness factor	
RG or R_g	normalized radius of the electrode (a/r_g)	

r_g	radius of the glass sheath for a microdisc	µm
t_i	time needed to achieve the event *i*	s
T	absolute temperature	K
α	phase in a solid solution	
β	phase in a solid solution	
β_i	symmetry coefficient of the species *i*	
η	overpotential	V
Θ	(i) surface coverage	mol cm^{-2}
	(ii) tilt angle between tip and substrate	°
ν	scan rate	mV s^{-1}

Abbreviations

Symbol	Meaning
CE	counter electrode
DL	double layer
EQCM	electrochemical quartz crystal microbalance
ESEM	environmental scanning electron microscope
EDX	energy dispersive X ray analysis
FWHM	Full Width Half Maximum
GSEI	gaseous secondary electron detector used in ESEM
HER	hydrogen evolution reaction
HRR	hydrogen reduction reaction
HS	hollow site hydrogen
ISE	ion-selective electrode
ML	monolayer
LVE	limited volume electrode
OCP	open circuit potential
OER	oxygen evolution reaction
ORR	oxygen reduction reaction
OTP	on top position hydrogen
RE	reference electrode
SHE	standard hydrogen electrode
SCE	saturated calomel electrode
SECM	scanning electrochemical microscope scanning electrochemical microscopy
SMSE	saturated mercurous sulphate electrode
STP	standard temperature and pressure
WE	working electrode

1. Introduction

The aim of this project is to develop the understanding of the carbonation processes in lime based mortars. The study presented in this thesis focuses on the development and application of microelectrodes to monitor the proton activity during the carbonation reaction. The main objectives of this study are to develop an experimental approach that can be used to monitor the reaction processes when growing carbonate crystals at the solid-liquid interface and to develop the knowledge of the electrochemical sensors used for those measurements. This research is carried out through collaboration between the Department of Architecture and Civil Engineering of the University of Bath and the Electrochemistry group of the University of Southampton.

Lime has been used as an inorganic binder in construction for thousands of years, examples of its use have been found in Palestine and Turkey dating from 12000 BC and lime mortars were widely also used by the Romans. The manufacturing techniques and the design of mortars to obtain materials with different performances are well understood, but the carbonation mechanism in lime mortars is still under observation. Some results have been published about the influence of various parameters on the growth kinetics of $CaCO_3$ crystals on an electrode.[1-12]

The origin of the precipitation of calcium carbonate has been studied using impedance spectroscopy[2, 3], thermal and gravimetric techniques[4, 11-14] and Raman spectroscopy[6, 8, 10, 12]. The chemical reactions which lead to $CaCO_3$ precipitation have been well described[5, 15, 16], and are reported in the reactions (1-4) below:

$$Ca(OH)_2 \rightleftharpoons Ca^{2+} + 2OH^- \quad (1)$$

$$CO_2 + OH^- \rightleftharpoons HCO_3^- \quad (2)$$

$$HCO_3^- + OH^- \rightleftharpoons CO_3^{2-} + H_2O \quad (3)$$

$$Ca^{2+} + CO_3^{2-} \rightleftharpoons CaCO_3 \quad (4)$$

However, this mechanism does not include the amorphous intermediate phases with the formula $Ca_{1+x}CO_3(OH)_{2x}\,yH_2O$ ($x > 0.05$, $y = [0.6; 0.8]$)[17]. The existence of these phases suggests that the mechanism is more complicated than generally described.

The pH is the most important parameter to characterize the state of the solution with respect to the various calcocarbonic *equilibria*. The fundamental phenomena that lead to the nucleation and subsequent growth of the $CaCO_3$ involved in the carbonation, have been studied and postulated, but no one has reported the proton concentration at the interface because of the difficulties encountered. In the field of calcium carbonate precipitation, the interfacial pH is of major importance and the main aims of the project are to determine the pH in the small volume of water sitting on top of lime crystals and to monitor how the carbonation reaction occurs. The rate of carbonation has traditionally been studied using an external approach, the simplest being the application of phenolphthalein as pH indicator to a surface and the assessment of compositional changes using thermogravimetric analysis[14, 18]. Other approaches have used the changes in weight and carbon dioxide uptake[19]; however these methods do not give detailed information on the surface reactions.

In this project, the procedure proposed to measure the pH is to use electrodes as passive probes. Those will be held with a micro-positioner in a configuration analogous to the scanning electrochemical microscope (SECM) in order to get precise spatial information. With this technique, it is possible to perform electrochemical measurements very close to the interface of interest (order of μm) using micrometre size sensors.

1.1. The carbonation reaction

1.1.1. The theory about the carbonation

On exposure to air, lime reacts with atmospheric carbon dioxide (CO_2) to form calcium carbonate. This process is known as *carbonation* and is responsible for the hardening of the mortar. $Ca(OH)_2$ is alkaline, whereas $CaCO_3$ is mildly acidic. Since the cement industry is several orders of magnitude larger than the lime industry, it is not surprising that research on carbonation is mainly published on cement mortars. Upon hydration, 16 to 20% of Portland cement is converted to portlandite[20], which is the active binder in lime mortar. Cement, in fact, is the building material made by grinding calcined limestone and clay to a fine powder, which can be mixed with water and poured to set as a solid mass or used as an ingredient in making mortar or concrete. Mortar is the workable paste used to bind construction blocks together and fill the gaps between them. The blocks may be stone, brick, cinder blocks, etc. Mortar becomes hard when it sets, resulting in a rigid aggregate structure. Modern mortars are typically made from a mixture of sand, a binder such as cement or lime, and water. While portlandite is the name of the particular structure of $Ca(OH)_{2.}$

The subsequent carbonation process is the same in both and much of the research findings are therefore transferable from cement to lime. The carbonation process can be described overall by the chemical process[21]:

$$Ca(OH)_2 + CO_2 \rightarrow CaCO_3 + H_2O \qquad \Delta H = 74\ kJ\ \text{mol}^{-1} \quad (5)$$

The carbonate weighs about 35% more than the hydroxide from which it was formed. There is also an increase in the volume of solids. $Ca(OH)_2$ (portlandite, which has a specific gravity of 2.24 g cm^{-3} and molar volume of 33.0 cm^3 mol^{-1}) is converted into $CaCO_3$ (calcite, or the more unusual crystalline forms vaterite and aragonite, which has a specific gravity of 2.71 g cm^{-3} and molar volume 36.9 cm^3), resulting in an 11.8% increase in the volume of solids. This increase in volume is accommodated by the pores of the mortar and tends to reduce access to CO_2. The heat generated by the reaction, 74 kJ mol^{-1}, may marginally contribute to evaporation of water from the pores, which can have the effect of reducing the rate of carbonation since water is the primary vehicle for carbonation. $Ca(OH)_2$ is accessed by the CO_2 in its dissolved state[22-24]. There are five stages involved: (i) diffusion of gaseous CO_2 through the pores of the mortar, (ii) dissolution of $Ca(OH)_2$ in the pore water as in equation (1), (iii) dissolution of the CO_2 in the pore water as described in equation (2), (iv) chemical equilibration of dissolved CO_2 in the pore water as expressed in equation (3) and (v) precipitation of $CaCO_3$ as shown in equation (4). Since carbonation only occurs in solution, low relative humidity will inhibit the reaction. The carbonation process is not only limited by pore blocking. It has been shown that even after carbonation has apparently completed, there are still small amounts of uncarbonated portlandite present [25]. Studies on medieval mortars have revealed the continuing presence of residual portlandite. Cultrone *et al* [26] proposed that carbonation is limited by the heat generated by the portlandite-calcite reaction, but it is more plausible that some portlandite crystals can be covered by an impervious layer of insoluble calcite, thereby blocking the access of CO_2 to the portlandite core [27, 28]. Swenson and Sereda [29] used optical extensometry and chemical analysis to demonstrate that particles of lime can be coated with calcium carbonate. This results in moisture being trapped inside the coating. When the moisture outside the coating dries out, a moisture gradient is created which is sufficient to produce cracking. A sequence of deposition of calcite, slowing of the reaction, drying and cracking continues until the build-up of the coating eventually stops the reaction and no further carbonation takes place, trapping some uncarbonated lime inside the coating. Theoretically, the size of the portlandite crystals has an impact on the rate of carbonation since the smaller the crystal, the higher the surface area is and the faster the access of CO_2 will be. The smaller particle size of aged lime putty also means that it retains a larger quantity of water which improves the workability[30]. The disadvantage of this higher water retention is that aged lime putty mortars show more shrinkage cracks than dry hydrate mortars [31].

1.1.2. The measurement of the carbonation

Although a wide range of methods are available to measure the carbonation, the traditional method of detecting this process is to spray a freshly broken surface of mortar with phenolphthalein. Where the surface is stained deep pink it indicates the presence of the highly alkaline portlandite, whereas uncoloured areas indicate that the portlandite has carbonated into neutral calcite. The implication often drawn from this is that there is a sharp boundary between carbonated and uncarbonated material. It has been demonstrated that a carbonation front develops which moves through the material as carbonation progresses[21]. Until now little research has been conducted into the measurement of the shape of this front. Parrot[32] used a range of different indicators to measure different levels of pH through concrete. Dewaele *et al* [33] measured changes in permeability across the front, and Lo and Lee[34] used FTIR to measure changes in the intensity of the characteristic peak C-O bonds stretching which is associated with changes in $CaCO_3$ content. Houst and Wittmann[35] used a homemade machine consisting of an induction oven and an infra-red analyser to measure the concentration of the thermal evolution of CO_2. This was done to a resolution of 0.2-0.5 mm on concrete specimens. Except for qualitative techniques such as phenolphthalein staining, quantitative measurements are generally based on average measurements[36] that often give misleading results. Portlandite is a strong alkaline material whereas calcite is neutral. This change in alkalinity can be used to detect the change in state from fresh lime to carbonated lime using a range of different techniques.

(a) Chemical indicators

In 1828 Vicat [37] described the use of ‘slightly moistened test paper’ to produce *‘…an evidence of the breadth of the carbonated parts.’*. Phenolphthalein is an indicator which changes from clear to a deep pink above a pH of about 9.3, and it is the most common method used to detect carbonation in both lime mortars and concrete. Indicators do not change colour sharply at one particular pH, but rather over a narrow range. For phenolphthalein, this range is between 8.3 and 10.0. When applied to a freshly broken specimen of lime mortar, a stained area is seen which marks the ‘un-carbonated’ material. This colour change is used to measure the ‘carbonation depth’. A phenomenon which is occasionally observed in lime mortars is the presence of Liesegang patterns: this is a quasi-periodic self-organising precipitation of a sparingly soluble product in the wake of a moving reaction front[38]. As the carbonation front progresses through the mortar, under certain circumstances the carbonation product will be more concentrated at some distances from the surface than at others, these are characterized in lime mortars by concentric rings of stained and unstained material most often seen when the binder is an aged lime putty. The pale rings represent areas of mortar with a higher level of carbonation than the areas to either side. Other indicators have been experimented with to detect carbonation in concrete but with little success[32]. The problem with many of these indicators is that they are not readily visible and the pH at which the colour change occurs in other indicators is not at the right level to show carbonation satisfactorily.

(b) Chemical titration

Chemical titration can be used to measure the $Ca(OH)_2$ content of mortars[39, 40]. This method involves the mixing of ground material in a fixed concentration of portlandite solution for 24 hours followed by titration with nitric acid (HNO_3) until a pH of 12.0 is attained. The amount of HNO_3 required can be used to calculate the amount of hydroxide contained in the solution.

(c) Gravimetry

Lime mortar increases appreciably in mass as it carbonates. Medici and Rinaldi[41] used gravimetry to establish the weight of $CaCO_3$ that was formed at a particular point in time. The mortar under study was a dry hydrate/sand mortar in a high CO_2 environment, forcing complete carbonation within a period of 7 days. This technique requires the use of micro-balances in an enclosed controlled atmosphere in order to eliminate errors due to differences in absorbed water at different weighing times. For this reason the technique is most commonly used with small cement or lime paste samples[42]. The technique is effective with forced carbonation experiments, where the experiment may last a few hours or days. It is not appropriate for long-term studies of carbonation in atmospheric conditions. The information gained from gravimetry provides bulk carbonation data and it is not possible to establish anything about the movement of the carbonation front through the material in terms of rates of progression or shape of the carbonation front.

(d) Velocity of ultra-sound

This non-destructive technique has been pioneered by Cazalla *et al.*[31, 43]. The carbonation process is characterized by an increase in the velocity of longitudinal ultrasonic waves and is related to the degree of compactness. The greater the longitudinal velocity, the greater the decrease in the total anisotropy of the samples is. The advantage of this method is that it is non-destructive, and a large number of measurements can be taken rapidly. This technique does not give absolute data, but rather gives a measurement of the changes in mechanical properties taking place within the mortar. Cazalla promotes this technique as a quick and inexpensive, non-destructive method for comparing the performance of different materials.

(e) Thermogravimetry

Thermogravimetry (TG) is frequently used for the compositional analysis of materials because it measures the weight loss resulting from the thermal decomposition of a sample[44]. TG is a technique that gives results that are intrinsically quantitative because it is based on those reactions that take place with a change in weight. Thus the measured weight loss reflects the overall reaction taking place. As with all analytical techniques the procedure requires careful planning and control. The requirements for a successful TG analysis include: (i) a good knowledge of the material being analysed, (ii) awareness that a dependency exists between the components in the mixture, (iii) good instrument condition with a sufficient pre-analysis purge in order to remove any gasses present in the furnace that may react with the sample, (iv) proper selection of parameters like temperature halts, gradients, atmospheres. The basic technique can be improved using the thermogravimetry derivative because the first derivative of the TG data can be very revealing in identifying the onset and finishing temperatures for individual mass changes. Typically, for calcium carbonate samples four distinct phases of weight loss can be identified: (i) loss of physically adsorbed water from 20 up to 110 °C, (ii) the thermal breakdown of iron impurity always present in the aggregates between 250 and 300 °C, (iii) thermal breakdown of the $Ca(OH)_2$ into CaO and water (dehydroxylation) between 400 and 475 °C and (iv) the thermal breakdown of $CaCO_3$ into CaO and CO_2

(decarboxylation or calcination) between 800 and 900 °C. The knowledge of the stoichiometry of these reactions allows an accurate quantification of the weights of material originally present in the sample under investigation. The shape of the decarboxylation curve can also be used to identify different crystalline forms of $CaCO_3$ as amorphous carbonate, calcite, aragonite and vaterite.

(f) Raman spectroscopy

The Raman Effect was discovered in 1928 and has been used ever since to characterize materials. The Raman spectroscopy involves the excitation of the molecules in a specimen using a monochromatic-laser beam. The spectra of the resulting emissions are characteristic of particular molecules[45, 46]. Only recently, the technique has been applied to lime mortars[42, 47]. There is a general carbonate peak at 1085 cm^{-1} that clearly identifies the presence of $CaCO_3$. Calcite, vaterite, and aragonite signals overlap closely, but they all have distinctive spectra in the 700 – 800 cm^{-1} region that allow the forms to be differentiated[48]. $Ca(OH)_2$ produces a strong peak at 3620 and 3640cm^{-1} [49]. The Raman signal is produced by exciting the material using a laser beam with a diameter of approximately 4 μm[42]. The resulting data are very informative about the functional groups under the laser spot, but if the material under investigation is inhomogeneous, it can be misleading. The presence of a range of different constituents in the mortar can produce strong fluorescence[50]. This can cover the true Raman signals which tend to restrict the use of Raman to pure pastes rather than multi-phase materials such as mortars.

(g) X-Ray diffraction (XRD)

The dimensional structure of crystalline materials consists of regular repeating planes of atoms that form a crystal lattice. When a focused X-ray beam interacts with this lattice, part of the beam passes through, part is absorbed, part is refracted and scattered and part is diffracted. The part that is diffracted is characteristic of the mineralogical structure of the sample. The angle between the incoming X-ray beam and the detector is varied during an X-ray scan, and the resultant signals are measured in 'counts per second' (cps) and can be displayed graphically against the angle formed between source, sample and detector. This angle is referred to as 2θ. The distances between the planes of the atoms that make up the sample can be measured by applying Bragg's Law:

$$n\,\lambda = 2\,d\sin\theta \tag{6}$$

where n is an integral multiple of λ, the wavelength of the incident X-ray beam, d is the distance between adjacent planes of atoms (referred to as the 'd-spacings') and θ is the angle of incidence of the X-ray beam. In order for the diffraction patterns to occur, the X-ray beam reflected from the upper atom and the X-ray beam reflected from the lower atom must be in phase which allows them to reinforce each other. This requires the beam distance between the reflection planes to be an integral multiple of the wavelength of the beam. Since the beam has to travel twice this distance the integral multiple wavelength of the beam when the phases of the beams coincide and reinforce each other is equal to $2\,d\sin\theta$. Since λ and θ are known, it is possible to calculate the d-spacings. An X-ray scan will produce a set of d-spacings which are a characteristic fingerprint of the minerals present in the sample. XRD is a reliable technique that is widely used for characterisation of mortars[51]. It has also been used to investigate carbonation in new materials, particularly for the measurement of the relative proportions of calcite and portlandite[26, 31, 36]. This technique is capable of identifying the form and size of portlandite crystals in lime putty[52]. The phase analysis of calcium carbonate can also be identified using XRD - allowing differentiation between calcite, aragonite and vaterite[48]. However, XRD does not easily quantify the relative proportions of different materials. Firstly, the signals for each material have to be separated and, secondly, relative intensities are not directly proportional to relative quantities[53]. In general, researchers use XRD to detect the presence of a certain material, rather than their quantity[36].

(h) Optical microscopy (OM)

Crystalline materials can be identified with the use of polarisation and fluorescence microscopy (PFM). When a beam of light enters an anisotropic crystal, it is split into two beams of polarised light with different refractive indices. When viewed through a microscope between crossed polarisers, characteristic interference patterns can be observed which allow the crystals to be identified. In addition, voids can be seen and counted if the specimen is impregnated with a fluorescent resin. This procedure gives insight into the pore structure[53, 54]. Preparation of slides is time consuming and problematic for friable materials, such as lime mortars. However, once prepared, they can be quickly examined, photographed and analysed.

(i) Scanning electron microscopy (SEM)

SEM offers the opportunity to examine materials at far greater magnifications than can be achieved using optical microscopy (OM). Environmental SEM (ESEM) gives the opportunity for low-vacuum analysis of wet or larger samples, and is suitable for examination of the carbonation front in lime mortars. Individual crystals can be examined[55, 56], as can the bonding between carbonated binder and filler. Pores in the structure, through which CO_2 gains access to uncarbonated $Ca(OH)_2$ can also be examined[57]. Once a suitable subject has been located in the specimen, ESEM photomicrographs can be rapidly taken for subsequent analysis. Back-scatter mode SEM used on polished specimens allows the internal structure of mortar to be clearly seen[58]. Combined with digital image analysis, the porosity and the pore size distribution can be visualized[59]. Energy dispersive X-ray analysis (EDX) allows the identification of the elemental composition of an area of a specimen under SEM examination. The difficulty with this system is that elements lighter than oxygen are difficult to detect quantitatively without a standard. It is therefore difficult to differentiate between $Ca(OH)_2$ and $CaCO_3$ since the difference between them is carbon (atomic weight 12) and hydrogen (atomic weight 1), both of which have lower molecular weights than oxygen (atomic weight 16).

(j) Fourier transform infrared spectroscopy (FTIR)

Infrared spectra of the characteristic peak of the C-O bonds stretching can be detected using FTIR[34]. This technique appears to be considerably more sensitive than the phenolphthalein staining test. The technique involves taking powdered samples at 1.5 mm depth increments. The IR spectrum of each powder sample is mixed with KBr in the proportion of 1:10 to facilitate quantitative measurement of carbonation depth. Samples are dehumidified for 1 day prior to testing in order to minimize moisture effects. Each sample is scanned 50 times with a 4 cm^{-1} resolution in the range 400-4000 cm^{-1}. The characteristic peak of the C-O functional group is in the range 1410 - 1510 cm^{-1}. This technique is able to produce data which identifies the presence of carbonation in concrete more accurately than phenolphthalein staining.

(k) Using a pH meter

In theory, the pH of mortar could be measured using a pH electrode. The overall pH of mortars has been measured in order to establish the susceptibility of the environment to fungal growth[60]. This technique involved suspending a 10 mm x 10 mm x 3 mm specimen of mortar in a fixed volume of distilled water for 2 days, followed by the measurement of the pH with an electrode. Given that the resolution of this system is 3 mm, this approach would not offer any advantages over phenolphthalein staining, and the test takes much longer to perform.

1.2. The basic theory on potentiometric probes

Potentiometric ion selective electrodes (ISE) are passive probes which, contrary to voltammetric sensors, do not convert the analyte in the sample. The response of an ISE depends linearly on the logarithm of the activity of the primary ion in presence of other ions. The cell potential is the sum of a number of local potential differences generated at the interfaces within the cell and measured between the two (reference) electrodes. At no current flowing, the cell potential, E_{cell}, is given by:

$$E_{cell} = E_{ISE} - E_{ref} + E_{jnc} \tag{7}$$

where E_{ISE} is the potential of the ion-selective electrode, E_{ref} the potential of the reference electrode and E_{jnc} the liquid junction potential arising at the interface of the sample solution and the internal electrolyte solution of the reference electrode. In analytical applications, one chooses electrolyte combinations to eliminate liquid junction potentials.

In ISE potentiometry, the cell potential reflects the dependence of the membrane potential on the primary ion activity. According to the Teorell-Meyer-Sievers[61, 62] theory, the sum of three different potential contributions, the phase boundary potentials generated by ion-exchange process at both interfaces, $(\Phi_1 - \Phi_{m,1})$ and $(\Phi_{m,2} - \Phi_2)$, and the inter-membrane diffusion potential, $(\Phi_{m,1} - \Phi_{m,2})$, constitutes the membrane potential.

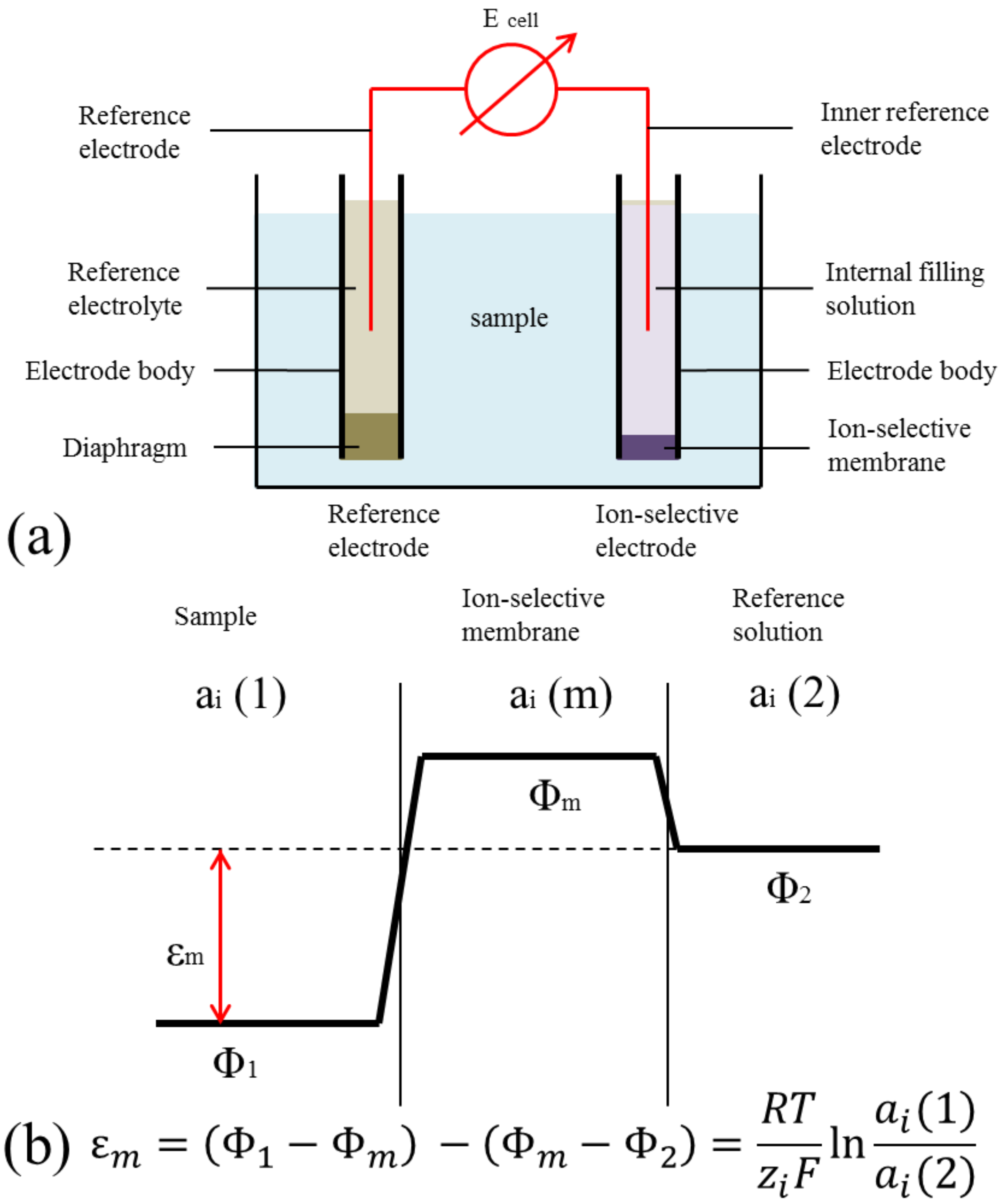

Figure 1.1 (a) Schematic diagram of ISE circuit. (b) Potential profile across an ion-selective membrane of fixed sites, symmetrically bathed with the sample and the reference solution. Reproduced from[63].

If the membrane composition is constant and there are no concentration gradients within the membrane, then the membrane diffusion potential is zero and the membrane potential can be described by phase boundary potentials. This approach is used to treat the response of ISE made with a range of membranes. For an ideally selective electrode, the measured cell potential is described by the Nernst equation:

$$E_{cell} = constant \pm 2.303 \frac{RT}{z_i F} \log(a_i) \tag{8}$$

where a_i refers to the activity of the primary ion i in the sample solution, z_i is the charge of the primary ion i, R is the gas constant, T the absolute temperature, and F the Faraday constant. $2.302\frac{RT}{z_iF}$ is the Nernstian slope, which is equal to $\frac{59}{z_i}\ mV$ at 25°C. The constant term includes all primary ion i activity independent terms.

In practice, however, deviation from the ideal electrode behaviour is common, and an additional contribution to the total measured ion activity has to be considered due to the presence of the interfering ion j in the sample solution. Under these conditions, the ISE potential can be approximated by the Nicolsky-Eisenman equation[64]:

$$E_{cell} = constant\ \pm 2.303\ \frac{RT}{z_iF}\log\left(a_i + \sum_{j \neq i} K_{ij}^{pot}(a_j)^{z_i/z_j}\right) \tag{9}$$

where a_j and z_j are the activity and charge of interfering ion j. the weighting factor $K^{pot}{}_{ij}$ is the selectivity coefficient. Naturally if the value of $K^{pot}{}_{ij}$ is small, the contribution of the interfering ion to the total cell potential is negligible. The selectivity coefficients can be determined potentiometrically and are tabulated. Their values are used as guideline when designing ISE-based potentiometric experiments[63].

1.3. pH measurements with potentiometric sensors

Although the most common technique for measuring pH in laboratory and industries is based on the use of the pH glass electrode[65-67], developed 100 years ago by Haber and Klemensiewicz[68], there are various sensors to measure the pH. Several inconveniences in the use of glass pH electrode have stimulated the research in other methods to measure the pH. The pH sensitive glass can be easily damaged; major cracks are obvious, but minor damage can be difficult to detect. The glass can become old and exhibit a slow response. The deposit on the glass electrode surface will also slow and alter the response. The damage of the glass is especially critical during pH measurements in living organism using catheter type electrodes. The miniaturization of electrodes also requires non glass sensing devices. The non-glass pH sensitive electrodes can be divided in several groups. There are sensors based on antimony and other metal oxides, ion sensitive field effect transistors, and various polymeric membranes loaded with ion carriers[69].

1.3.1. Conventional ionophore based pH electrodes

The first pH sensing electrode based on ion carriers can be found in the literature between the late seventies and early eighties of 1900. The main interest was to exchange the glass membrane in microelectrodes dedicated to intracellular measurements with liquid or plastic membranes that possess less electrical resistance and are less fragile. Good reviews have been written by Buhlmann, Pretsch and Bakker[70, 71]. The sealing of pH glass membranes to bevelled silica pipets poses many technical problems. In contrast, liquid membrane microelectrodes[72] are much easier to prepare and do not suffer from the disadvantages of tip geometry as the glass membrane electrode preparation technique. For this purpose, classical electrically charged ion carriers have been introduced for use in polymeric membranes[73-76]. However the selectivity against other ions was not satisfactory. One of the first work in this field was a H^+ sensitive microelectrode based on a neutral ion carrier belonging to the class of lipophilic amines, tri-n-dodecylamine (TDDA)[77, 78]. The selectivity with respect to Na^+, K^+, Mg^{2+} and Ca^{2+} is sufficient for extra- intracellular H^+ ion activities being less or equal to $3.2\ 10^{-6}$ (pH 5.5) at typical ionic backgrounds. Electrodes with tip diameters around 1 mm have an electrical resistance around $10^{11}\ \Omega$ and a 90% response time less than 5 s. An example of intracellular application of these electrodes can be founded in the pH determination of *xwnopus laevis* oocytes[78] and in other cells[79]. Plastic electrodes have been developed for measuring pH in the human gastrointestinal tract[80]. The electrodes have plastic hydrogen ion sensitive membrane sealed to length of fluid filled PVC tubing. These electrodes have a potentiometric response of -52 to -58 mV/pH unit change in the range pH 4-9, with a diminished response outside this range. They have low resistance and a fast response time of 1 second to reach 90% of their maximal response. The electrodes can be passed down the biopsy channel of an endoscope to obtain mucosal pH readings under direct vision. Those readings are comparable to those obtained with the glass electrodes. Neutral ion carriers selective for H^+ ion were used in polymeric membranes for blood pH measurements[81] and in sensors for a variety of other assays[82-86] including potentiometric pH detection in suppressed ion chromatography[87]. A dual lumen catheter electrode design suitable for the simultaneous measurement of partial pressure of CO_2 and pH in flowing blood was described: the probe was fabricated from a single segment of dual-lumen silicone rubber or polyurethane tubing that was impregnated with the proton ionophore tridodecylamine[88]. The impregnation step imparts H^+ permselectivity to both inner and outer walls of the tubing. By filling each lumen with a suitable buffer/electrolyte solution and an Ag/AgCl reference electrode wire, simultaneous potentiometric detection of both P_{CO2} and pH was achieved. Careful optimization of incorporated proton carrier (tridodecylamine), plasticizer (o-nitrophenyl octyl ether), and lipophilic counteranion sites (tetrakis[3,5-bis(trifluoromethyl)phenyl] borate) within the tubing walls yielded catheter electrodes with resistance values of 10-20 MΩ and relatively high stability in flowing blood. Results from continuous measurements of p_{CO2} and pH during long-term 30-65 h blood loop experiments demonstrated that, after an initial conditioning period, the catheter exhibits low drift rates and yields continuously measured values in good agreement with those obtained on discrete samples with a commercial blood gas analyser. In vivo evaluation of the catheter sensors, performed by implanting silicone rubber dual-lumen probes in the arteries of anesthetized dogs, indicated that the proposed catheter design can closely follow p_{CO2}/pH changes induced in the animals during 6-13 h of continuous monitoring. Although the obtained selectivities are impressive, the sensors have a narrower operational range in comparison to glass pH electrodes and the cation interference imposes limitations in their use at high pH values, while the anion interferences set a limit at the lower pH values. The pH range for the application of a hydrogen ion selective sensor depends on the acidity constant (pK) of the ionophore incorporated to the membrane.

Eleven neutral hydrogen ionophores possessing a basic nitrogen atom for ion selective electrodes for a distinct pH range were proposed[89]. The pK of the nitrogen atom determines the position of the dynamic range of the electrode. A small value of pK shifts the dynamic range to smaller pH values and vice versa. For gastrological applications the pK value between 4 and 5 seems to be optimal. To reduce cation interferences, the ionophores should contain neither additional coordination centres such as amide, ester or ether functions, nor structural groups that might form chelate rings upon coordination with the cation. The ionophore should be of high lipophilicity, electrically neutral and in the unprotonated form. The potentiometric response of several ion selective polymer membranes prepared with aminated and carboxylated PVC were examined and compared to those observed with the non derivatised polymer[90]. The presence of carboxyl or amine functional groups within the membranes is shown to have little effect on the response and selectivity of the tridodecylamine based membrane. Blank aminated PVC membranes respond to pH in analogous manner to that of underivatised PVC membranes containing tridodecylamine, while blank carboxylated PVC membranes exhibit little or no proton response. The implication of the findings is discussed in terms of the charged and uncharged nature of the functional groups within the membrane phase as well as the potential advantages of using functionalised PVC to fabricate biosensors. The ion-exchange properties of carboxylated PVC are described and interpreted by theory and experiments for H^+ membrane sensitive sensors[91]. A PVC matrix membrane pH electrode based on neutral carrier containing tertiary amino and azo groups was developed by Yuan *et al.*[92]. This electrode has an excellent pH response with a much wider linear range (1.7-13.2) as compared with previously described sensors. The sensor has a near Nernstian slope of -57.4 mV/pH. The electrochemical impedance spectra of electrode membranes were also studied [92]. The bulk resistances increased with increasing pH in the pH region less than 2.0, whereas in the range 2.0-3.0 the resistance decreased with increasing pH and it remained almost constant in the pH range 3.0-4.5. In the range 4.5-5.0, the resistance increased with increasing pH and remained almost constant in the pH range 5.0-7.0. It has been proposed that failure of the Donnan exclusion starts at pH less than 2.0. At pH more than 5.0, the charge transfer is mainly controlled by the tertiary amino groups of the incorporated ionophore, whereas in the pH range 2.0-5.0 the charge transfer is contributed by azo groups of the ionophore. The reported electrodes[92] were used for blood serum analysis and for hydrofluoric acid titration. Polymeric membranes containing electrically charged H^+ carriers were compared by Mi *et al.*[93] with tridodecylmethylammonium chloride based membranes. The electrodes were stable and exhibited lifespan of over half a year. Derivatives of dibenzylamine have been used as neutral carriers in liquid membranes electrodes for the pH range from 2 to 10[94]. Especially octyldibenzylamine based electrode gave a better linear response to pH than other alkyldibenzylamines. The hydrogen ion selective PVC membrane electrode based on calix[4]arene was also reported by Kuruoglu *et al.*[95]. The electrode showed a near Nernstian response in the pH range 2-11.5 with good selectivity and long lifetime. Recently, fluorophilic ionophores for potentiometric pH determination with fluorous membranes of exceptional selectivity were developed by Boswell *et al.*[96]. These electrodes are the first fluorous ionophore based sensors described in the literature. Their selectivity is not only better than of similar sensors with nonfluorous membranes but it is also comparable to the best ionophore based pH sensors ever reported. These membranes are hoped to be more biocompatible than other matrices. The binding properties of neutral or charged H^+ selective chromoionophores in solvent polymeric membranes were characterised in situ by the so-called sandwich membrane method[97]. The pK_a values of all investigated ionophores in membranes containing dioctylsebacate as plasticiser are 2-3 order of magnitude smaller than of those containing nitrophenyloctyl ether. The quantitative structure activity relationship for neutral carriers used to prepare hydrogen ion sensors was studied by Cao *et al.*[98]. Series of synthesised carriers were taken as the training set and a new carrier was proposed and synthetized, (4-hydroxybenzyl)-didodecylamine. The pH electrode based on this carrier had a wide pH linear response range of 2.0-12.5 and showed a near Nernstian response slope of -57.2 mV/pH. The sensor also had low resistance, short response time, high selectivity and good reproducibility. Moreover the sensor was successfully applied to determine the pH value of blood serum samples.

Ion-selective microelectrodes have found some applications also in scanning electrochemical microscopy because of the micrometre dimension, the high selectivity and low detection limit[63]. The pH probes based on H^+ sensitive liquid membranes have been used in pH microscopy where pH profiles have been measured in corrosion studies[99, 100] and in measuring biological activities[101, 102].

1.3.2. Ionophore based pH electrodes with solid contact

A good review concerning solid contact ion-selective membrane electrodes is given by Bobacka *et al.*[103]. Elimination of the internal filling solution from conventional ion selective electrodes results in more durable and easier to miniaturise systems. Research and development of solid contact electrodes started in the early seventies with the invention of the coated-wire electrode[104]. The main disadvantage of this structure is poor potential stability resulting from the blocked interface between purely electronic conductor (metal) and the purely ionic conductor (ion-selective membrane). Introducing an additional material showing mixed electronic and ionic conductance between both faces improves the potentiometric stability of the sensor. Various arrangements were used including Ag/AgCl, Ag/AgCl/hydrogel, redox self-assembled monolayers, carbon based composites, Ag-based composites and conducting polymers such as polypyrrole (Ppy), polythiophen (POT) and polyaniline (PANI). Ppy doped with various anions was used as a solid contact in pH electrodes based on polymer membranes containing tertiary amine ionophores. Electropolymerised PANI was applied as a solid contact on plasticised PVC based membranes selective to pH[105]. The PANI is pH sensitive itself. PANI protonated (doped) with phosphoric acid dihexadecyl ester was used both as ion-to-electron transducer and as pH-sensitive component in plasticised PVC based membranes[106]. Membranes containing 50% (w/w) PANI and 50% plasticised PVC showed the best pH sensitivity among the others. Several hydrogen ion-selective electrodes containing various alkyldibenzylamines[107], tetrabenzylethanediamine[108] and PANI as solid contact have been prepared. A solid-state pH electrode was developed by using electrochemically synthesised Ppy doped with cobalt bis(dicarbollide)[109]. The electrode showed a quasi Nernstian response (-50 mV/pH) from pH 3 to 12. Electrodeposited polymers based on various monomers containing amino groups such as 1,3-diaminopropane, diethylenetriamine, pyrrole, p-phenylenediamine and aniline were studied as pH sensors, showing a linear response in the range from pH 2 to 11[110]. Polypyrrole-based pH sensors were miniaturised by Lakard *et al.*[111]. A solid-state pH nanoelectrode was constructed by electrodeposition of PANI onto an ion-beam conically etched carbon fibre with a tip diameter of *ca* 100-500 nm[112]. The electrode had a slope of about -60 mV/pH in the range 2.0-12.5. The selectivity coefficients in the logarithm scale were around -12 with respect K^+, Na^+, Ca^{2+} and Li^+. A solid-state pH microelectrode based on PANI electrodeposited on a microband electrode was used for *in situ* pH measurements of self-oscillating Cu(II)-lactate system[113]. A silicon substrate was used to construct a pH sensitive microelectrode with ion-selective PVC membrane on top of a polypyrrole layer doped with cobalt bis(dicarbollide)[114]. A microfluidic device was developed for measurements of pH, Ca^{2+} and K^+ concentrations with solid-state ion-selective electrodes incorporated in the channel[115]. A thick film H^+ and K^+-selective sensor arrays based on solvent polymeric neutral carrier membranes containing layers of silver, silver chloride and hydrogel was described by Cosofret[116]. The preliminary in vivo experiments were performed to monitor H^+ and K^+ distribution in the beating pig heart to determine the unique ionic conduction responsible for ventricular fibrillation in the setting of acute regional myocardial ischemia. Construction of various planar solid state microelectrodes as well as reference electrodes for flow analysis was reviewed by Maminska [117].

1.3.3. Ion-selective field effect transistors (ISFET) pH sensors

In general, an ISFET is a modification of the field effect transistor used in many amplified circuits. In the ISFET, the metal gate, which is normally used as input, is replaced by an ion-sensitive membrane, the measured solution, and reference electrode.

The ISFET combines in one device the sensing surface and a signal amplifier which produces a high current, low impedance output and allows the use of connecting cables without excessive shielding. The ISFET theory and practice was widely discussed by Bergveld[118]. The same author first described the application of field effect transistors as transducers in electrochemical sensors and their application in medical research[119]. In the mid-eighties silicon chip pH sensors began appearing on the laboratory pH market. The small size, accuracy, fast response time and batch fabrication capability made the sensor ideal for medical applications. The ISFET pH sensors are now available for laboratory and industrial pH applications in a variety of configurations including 316 alloy stainless steel probes. The sensing surface of the ISFET can be silicon oxide and silicon nitride. In contact with aqueous solution the surface OH groups are in equilibrium with the OH^- and H^+ ions from the solution. Alternative hydrogen ion sensitive coatings include aluminium oxide, zirconium oxide or tantalum oxide[118, 120]. The use of such dense hard materials as sensor surfaces makes ISFETs especially durable. However, in the case of biomedical instrumentation, often arises the problem of the biocompatibility. The pH sensors of the ISFET may also be a part of multifunctional analyser: a small combined ISFET pH electrode incorporating a reference electrode was located in the gastric corpus under fluoroscopic control[121]. The pH monitoring was performed over 21 hours and it showed an early morning rise in pH with three meal associated pH peaks lasting for about 2-3 hours [121]. The construction was inexpensive and disposable. The majority of works on pH ISFETs has been done with devices whose gate has been overlayered with solid-state insulators formed by either vacuum deposition or chemical vapour deposition. Another possible application is to use pH neutral carriers as a part of ISFET devices[122].

1.3.4. Metal and metal oxides pH electrodes

Requirements for precise and accurate pH measurements (mainly in biological research) as well as new technologies lead to the construction of pH sensors based on metal-metal oxide equilibria. This allowed to study in detail chemical parameters in smaller organs and organisms. Several researchers became interested in metal pH sensitive electrodes to overcome difficulties in making pH glass microelectrodes.

Antimony

Antimony and tungsten were the first metals that have been used[67, 123]. Because of its relatively low melting point, ease of fabrication and availability of substrate of high purity, antimony became the most common substance used for making metal pH microelectrodes. At the real beginning, the tip of the electrode was as small as 1 mm and the pH range was found being nearly Nernstian in the range from 6.5 to 8 after very careful calibration procedure[124]. The biomedical use of polycrystalline antimony pH electrode was hampered by oxygen dependence and low pH resolution (0.1 pH) [125, 126]. The pH resolution was improved by using highly purified crystallographically orientated monocrystalline antimony[125]. The sensitivity of metal-metal oxide electrodes to various buffer containing complexing components as well as to the redox potential has been studied[127]. Single-use commercially available antimony pH catheter sensors were recently compared with a glass electrode in a wireless pH monitoring system[128]. The nadir oesophageal pH values were recorded during the orange and cranberry juice swallows and were used to determine the accuracy of both electrodes in vivo. An approach named "capillary melt method" was developed to produce micro antimony wires, and the wire surface was then oxidized in nitrate melt at high temperature to obtain an antimony/antimony oxide electrode[129]. It was shown that the oxide layer on the wire surface is porous and consists of Sb_2O_3 crystal phase. The oxide layer is dense and uniform, with high physical and chemical stability. The pH electrode made using this method showed good sensing performance in buffer solutions in the test range pH 2 to 12. The linear relationship has a slope of -54.1 mV/pH. The advantages of the electrode are long term stability, fast response, good reproducibility and low cost. This electrode was used for pH measurements in agar medium for tissue culture[130]. When the antimony electrode is applied to SECM[99, 131], the tip-substrate distance was obtained by amperometric approach curve in the conventional mode, since special pre-oxidation is not necessary before the pH measurement. Antimony microelectrodes have been used to measure the pH in the vicinity of platinum[131, 132] and copper[133] electrodes during various electrode reactions. The pH profile near a cathode during metal deposition has also been recorded [134, 135]. Other applications were monitoring local pH changes near bilayer lipid membrane[136] and ion-exchange membrane[137]. Recently, antimony tips were employed because the dual-function characteristics of this material allow the combined amperometric/potentiometric operation of the SECM. The applicability of this technique was illustrated by Izquierdo *et al.*[138] considering the galvanic corrosion of a model zinc–iron pair immersed in chloride aqueous solution. Spatially resolved images of pH and oxygen concentration above the metal specimens were obtained in the same experiment. The same authors also studied inhibitors of galvanic corrosion of copper coupled to iron by using benzotriazole[139] and the electrochemical behaviour of magnesium-based materials[140]. The potential determining reaction of antimony electrodes was suggested by Bates[1] and verified by Ha and Wang[129] to arise from a redox reaction between the antimony metal and the surface oxide as shown in equation (10):

$$Sb_2O_3 + 6H^+ + 6e^- \rightarrow 2Sb + 3H_2O \qquad (10)$$

Iridium

A large group of pH electrodes is based on iridium oxide. Sputtered platinum electrodes fabricated on flexible films or platinum wires were used as planar or cylindrical supports[141]. The pH sensing layer consisted of anodically electrodeposited iridium oxide film[126]. Each electrode site was coated with Nafion to decrease the interference of anionic redox species and to protect the electrode surface during *in vivo* measurements. The electrode showed a slightly super-Nernstian response with slope -63.5 mV/pH in the pH range from 2 to 10 for both wire and planar electrodes. The electrodes have a working lifetime of at least 1 month with precision of about 0.02 pH unit and fast response time. They showed very low sensitivities for different species, such as Na^+, K^+, Li^+, NH_4^+, Ca^{2+}, Mg^{2+}, dissolved oxygen, lactate and ascorbate, which are all important in physiological applications[141]. A composite scanning micro pH electrode was developed based on iridium oxide produced in a carbonate melt[142]. The potentiometric response was very fast (less than 0.5 s) for a pH change from 1.75 to 13.90. The pH image on the surface of an Al/Cu galvanic couple showed that both anodic and cathodic areas could be sensed well and that the localized corrosion was taking place at the interface between Al and Cu. It developed over time and the pH value around the pitted region decreased gradually. The melt oxidation at high temperature was adopted to prepare Ir/IrO_x pH electrodes, and different carbonates as Li_2CO_3, K_2CO_3, Na_2CO_3 and their mixture were used[143]. The electrodes have a good pH response characteristic such as stability, sensitivity, response time and anticorrosion ability in solution containing fluoride. A surface renewable pH electrode was prepared by using composite electrode technique[144]: iridium oxide micro particles were prepared by hydrolysis of $(NH_4)_2IrC_6$ at elevated temperature. The iridium oxide particles were mixed with dispersed carbon black and then filtered. The mixture was suspended in DMF containing PVC as binder. The mixture was precipitated rapidly by adding large amount of water. The precipitate was grounded and pressure-melted to obtain an iridium oxide composite electrode material. The electrode showed a linear response between pH 1 and 13 with a slope from -50 to -60 mV/pH maintained without appreciable slope drift for 170 days when stored in deionized water. The electrode surface can be renewed by a simple grinding process whenever contaminated or deactivated. Electrochemical, chemical and physical growth of iridium oxide on various substrates and obtained by various methods were recently reported[145-147]. More recently, direct electrochemical deposition of iridium oxide layer has also been reported[148-151]. It has been reported that iridium oxide electrodes tend to show two linear regions of pH response with the transition point around pH 6[148], but most studies do not show this. It is also known that they tend to exhibit super-Nernstian (|slope|>59 mV/pH) pH response. This suggests that the number of electrons transferred for every proton varies, and that it is dependent on the method of preparation, as suggested by Fog and Buck[152] and by Vanhoudt [153]. Sputtering and thermal oxidation methods tend to produce anhydrous iridium oxide IrO_2 and tend to show calibration slopes of -59 mV/pH. The potential determining reactions are thought to be:

$$IrO_2 + H^+ + e^- \rightarrow IrO \cdot OH \tag{11}$$

$$2IrO_2 + 2H^+ + 2e^- \rightarrow Ir_2O_3 + H_2O \tag{12}$$

However, electrochemically oxidized iridium tends to produce iridium oxide that is hydrated to various degrees. These have calibration slopes up to -90 mV/pH suggesting that 1.5 electrons are transferred for each H^+. A possible potential determining reaction for the hydrated iridium oxide is shown in equation (13):

$$2[IrO_2(OH)_2 \cdot 2H_2O]^{2-} + 3H^+ + 2e^- \rightarrow [Ir_2O_3(OH)_3 \cdot 3H_2O]^{3-} + 3H_2O \tag{13}$$

IrO_x was also used as the main pH sensitive material for preparation of low cost solid-state pH sensors[154]. The iridium content was reduced with addition of TiO_2, forming the binary system IrO_x–TiO_2, whose electroanalytical properties were evaluated in comparison with a commercial glass pH electrode. The minimum iridium content which gave suitable results was 30 mol%, and the electrode presented Nernstian and fast response in the pH range from 1 to 13, with no hysteresis effect observed. Besides, the electrode showed high selectivity in the presence of alkali ions as Li^+, Na^+ or K^+. The amount of iridium in the prepared electrodes was very small (<0.1 mg).

Applications of IrO_x microelectrodes include SECM experiments[148] to study the pH profile across a denitrifying biofilm[153], to monitor cell metabolism[155], for the fabrication of a wireless microanalysis system[156] and to study the dissolution of calcite[150].

Ruthenium

The ruthenium dioxide electrode showed a linear response in the pH range from 2 to 12 and was useable for a period of 3 months[157]. It was used for the end-point detection in acid-base titrations. The device was prepared by galvanic deposition of noble metal onto electrodes etched on a copper clad printed circuit board. Screen printed pH electrodes containing RuO_2 have been created by Koncki and Mascini[158] by hand-mixing graphite ink with RuO_2 so that the sensitive layer was sandwiched between a conducting layer of silver ink and an insulating layer with openings to allow contact. The calibration curve for this electrode yielded a slope of -51.2 mV/pH when the graphite ink was doped with 9.8% RuO_2. The sensor showed a good response for pH 2-7, but it deviated from the expected response for pH $\geq$ 8. The response time was also longer for alkaline solutions and reducing agents adversely affected the response of the electrode. Sputtered thin-films of RuO_2 were also reported by Kreider *et al.*[159] in a paper in which they compared the response with that of platinum, palladium and iridium oxides. This study showed that RuO_2 electrodes produced by reactive sputtering at room temperature were performing as well as iridium oxides electrodes. The calibration plot produced a slope of -54 to -59 mV/pH and prolonged exposure in buffered pH 10 solution caused a drop in the sensitivity from -52 to -54 mV/pH. A low cost pH electrode using a thin film of RuO_2-TiO_2 (70-30 mol%) was prepared on a Ti substrate and characterized[160]. The slope of the potential versus pH curve was -56.03 mV/pH and the electrode was insensitive to the presence of Li^+, Na^+ and Ca^{2+} in the solution.

Tin

A tin oxide (SnO_2) membrane was employed in the fabrication of pH electrodes by the sputtering method. The substrate was based on the indium tin oxide (ITO) glass substrate[161]. The SnO2 films were employed to produce an array of sensors in order to reduce the errors on a single sensor[162, 163]. The real time sensing system included eight readout circuits and one data acquisition card.

Tungsten

Several papers present tungsten oxide implementation in solid-state pH electrodes. A tungsten nanoelectrode was produced by etching a wire in 0.1 M NaOH solution at the potential of 0.4 V *vs.* a Ag/AgCl reference electrode for about 100 s and the diameters ranged from 500 to 800 nm. The pH ultramicrosensor was fabricated by producing WO_3 at the W nanoelectrode surface by electrooxidation in 2 M H_2SO_4 solution between 1 and 2 V. At last, Nafion was coated on the surface of the WO_3 to protect the pH ultra-microsensor[164]. The W/WO_3 pH sensor exhibited a good pH linear region from 2 to 12 with a slope of -53.5 mV/pH. The response times ranged from 3 s at about neutral pH up to 15 s at alkaline pH. Interference from various ions, lifetime, stability and reproducibility of the sensor were studied. The sensor was applied to measure the extracellular pH values and to study pH variation at the normal, damaged and recovery endothelial cells[164]. Tungsten pH sensors have also been widely used to monitor localized corrosion[165, 166], in flow injection potentiometry[167]. It has also been used for the pH monitoring of the heat transport circuits of thermal power plants in high temperature aqueous environments[168]. In the latter case, the electrode displayed a good linear response between pH 2-11 at different temperatures. A common agreement in the potential determining reaction has not been found yet. Yamamoto *et al.*[164] proposed:

$$WO_3 + nH^+ + ne^- \rightarrow H_nWO_3 \tag{14}$$

Dimitrakopulos *et al.*[167] proposed a different potential determining reaction based on the dark-brown colour of their oxide layer:

$$WO_2 + 4H^+ + 4e^- \rightarrow W + 2H_2O \tag{15}$$

$$W_2O_5 + 2H^+ + 2e^- \rightarrow 2WO_2 + H_2O \tag{16}$$

Lead

A new highly sensitive potentiometric pH electrode with a response in the acid region has been proposed by Lima *et al.*[169]. It consists of a PbO_2-paraffin matrix deposited on graphite. A direct relationship between the electric potential difference and the solution pH was observed from 1.2 to 7.5 with a slope greater than -100 mV/pH. A high correlation of the results with a conventional glass electrode was observed. A highly sensitive pH electrode based on a PbO_2 film electrodeposited on carbon ceramic electrode was also proposed[170]. For both α and β crystal structures of PbO_2, similar results were obtained[171]. The pH was linear from pH 1.5 to 12.5 with near-Nernstian slope of -64.8

and -57.8 mV/pH for α and β PbO_2 respectively[170]. The lifetime of the electrode was about 1 month. The response time was about 1 s in acidic medium and less than 30 s in alkaline solutions. The pH values measured in complex matrices such as fruit juices were in good agreement with those obtained with conventional pH glass electrode.

Palladium

As previously mentioned, palladium oxide electrodes have been used as potential pH sensors[159]. Several are the paths that can provide the oxidation, such as anodization in molten $NaNO_3$-LiCl[172, 173], high temperature oxidation of Pd wires coated with NaOH[126, 174, 175] and electrolysis in sulphuric acid using a combination of AC/DC potentials[176]. Kim and Lee[173] suggested the potential determining reaction as:

$$PdO + 2H^+ + 2e^- \rightarrow Pd + H_2O \qquad (17)$$

The reported slope values are nearly Nernstian for a pH range typically between 3 and 9.

1.4. The palladium-hydrogen system

Since Graham first observed in 1866 that huge amounts of hydrogen could be stored into a palladium rod, the palladium-hydrogen system has been the subject of many studies[177, 178] and reviews[179, 180]. The palladium-hydrogen system has been widely used as a model system to understand the sorption processes and because it represents a classic example of the removal of gas from a binary solid phase. In addition to academic purposes, it has also been utilised in many applications such as the hydrogenation of edible oil[181], the manufacture of semiconductors and the purification and storage of hydrogen for general chemical purposes or as fuel in fuel cells[182]. From a practical point of view, the large specific gravity and the high cost have been the two main reasons for searching for other hydrogen absorbing substances.

1.4.1. The solid-gas system

Usually, hydrogen is introduced into the palladium lattice *via* the gas phase. For the reaction $H_2 \rightarrow 2H$ to occur, the surface of the palladium needs to be sufficiently clean. The molecular hydrogen initially exhibits Van der Waals attractive interaction when approaching the metal surface, leading to the physisorbed state ($E_{phys} \approx$ -5 kJ/mol H) at a distance from the metal surface approximately equal to the hydrogen molecule radius (≈0.2 nm). Closer to the metal surface, hydrogen has to overcome an activation barrier for dissociation and formation of the hydrogen-metal bond. The height of the activation barrier depends on the chemical composition of the surface. When the hydrogen atom becomes chemisorbed (E_{chem} ≈-50 kJ/mol H_2) it shares its electron with the metal atoms at the surface. These hydrogen atoms have high surface mobility, interacting with each other and forming surface phases[183]. In the next step chemisorbed hydrogen atom can migrate into the subsurface layer and, finally, diffuse into the interstitial sites through the host metal lattice, contributing their electrons to the band structure of the metal[184]. After dissociation on the metal surface, the H atoms generally diffuse rapidly through the bulk metal even at room temperature to form a Pd-H solid solution known as the α-phase. The standard representation of the palladium-hydrogen phase relationship is the hydrogen pressure *vs.* hydrogen content *vs.* temperature plot, often shown in the form of an isotherm, as shown in **Figure 1.2**. The regions where the solid hydrogen content undergoes large changes are shown in the diagram as the area undergoing the black line. In this region, the α and β hydrides coexist below the critical temperature value, T_c, which for the H/Pd system is approximately at 310°C. It can be seen that the lower is the temperature, the larger is the region of coexistence of the two hydride phases. In this region there is a continuous transformation from the α to the β phase as the hydrogen content increases. The constant equilibrium pressure can be explained by the Gibbs phase rule. For a system in equilibrium, the number of degrees of freedom, F, can be expressed as:

$$F = 2 + C - P \tag{18}$$

where F can be seen as the number of intensive variables that can be changed independently without disturbing the number of phases in equilibrium, C is the number of components and P is the number of independent phases present in the system. Only one degree of freedom is permitted in conditions of two components (H and Pd) and three phases (α, β and H_2).

However the isotherms do not show the hysteretic difference in the hydrogen pressure exists between the α→β and the β→α phase transition[179]. When the hydrogen content is increased (absorption isotherm), the pressure measured shows a greater value than when the hydrogen content is being removed (desorption isotherm), shown in **Figure 1.3**. In this example, the combined adsorption/desorption isotherm shows a hysteresis loop for the palladium-hydrogen system at 120°C. There is a marked difference of 30 kPa between the two isotherms, however repeated absorption-desorption cycles have been shown to reduce the extent of the hysteresis as the increased temperature (at T_c there is no hysteresis). This method can be used to determine the critical temperature in metal-hydride systems.

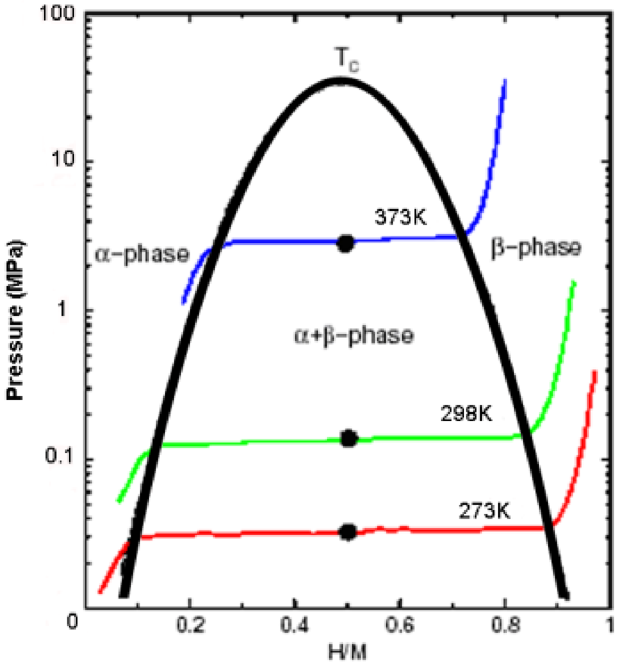

Figure 1.2 Pressure-Composition-Isotherms (PCI) for a hypothetical metal hydride. Taken from[183].

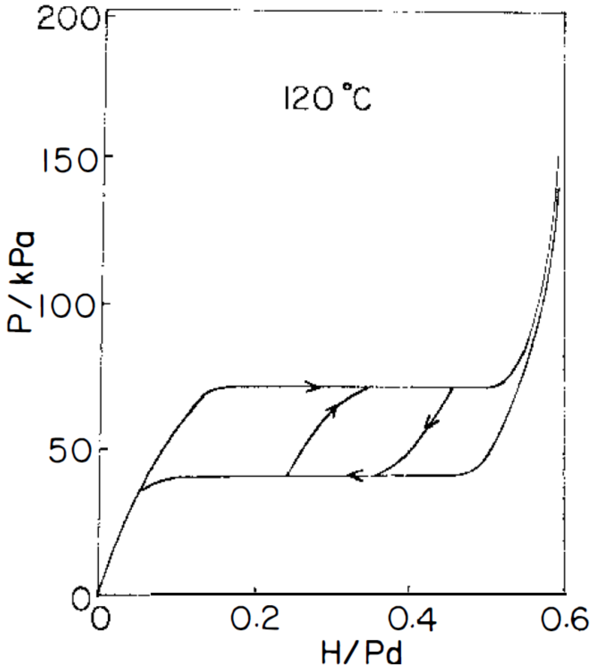

Figure 1.3 A hysteresis cycle shown for palladium-hydrogen at 120°C. A hysteresis scan is also shown starting from the decomposition plateau. Taken from [179].

Studies have also shown that at lower temperatures, hydrogen loading via solution of dissolved hydrogen proceeds at a faster rate than loading via the gas phase[185].

Researchers tried different methods to measure the hydrogen content of the palladium lattice *in situ*. Many different studies have been undertaken with the electrochemical quartz micro balance (EQCM)[186-190], neutron diffraction, extended X-ray absorption fine structure (EXAFS) and X-ray diffraction (XRD)[191] and with in situ resistance measurements (ISRM)[185, 192].

The EQCM is not a valid method for the measurement of absorbed hydrogen because the frequency changes due to two factors, the amount of hydrogen absorbed into the palladium lattice and the stress in the Pd. The stress is affected by different factors including the amount of hydrogen absorbed, the phase of the palladium and the electrode ageing[188].

Some problems have been encountered when measuring the resistance of the palladium film *in situ* and trying to relate this parameter to the measure of the hydrogen content. The inhomogeneous distribution of the hydrogen within the palladium lattice provides error in the measurement of the hydrogen content. These errors are particularly significant in the $\alpha+\beta$ coexistence phase[192].

1.4.2. The phases of the palladium hydride electrode

Palladium hydride electrodes have been extensively used as reference electrodes[193-198] due to the constant potential of the $\alpha+\beta$ transition phase. In palladium-hydride electrodes, it is the electrode itself that carries its own hydrogen supplies; therefore the saturation of the electrolyte with hydrogen is not necessary as for palladium-hydrogen electrodes. As previously mentioned, the potential of the electrode is dependent on the activity of protons in the solution, therefore $\alpha+\beta$ palladium hydride electrodes have also been used as pH sensors[197, 199-204]. The $\alpha+\beta$ palladium hydride pH sensors have been reported to show an almost theoretical potentiometric response with the slope of the potential-pH curve equal to about -59 mV/pH at standard temperature and pressure and they have been applied in experiments where the conventional glass electrode is not applicable such as at high temperatures[204] and in fluoride solution[202].

The palladium hydride electrodes are typically prepared by an activation step in order to obtain a surface with high activity (e.g. by electroplating a Pd black layer[205], oxidising and then reducing the surface or electrodepositing a nanostructured Pd film[206]) and then by loading hydrogen into the palladium by bubbling hydrogen through the solution or by electrolysis. Palladium hydride electrodes with different shapes were created, but only four are the reports about PdH microelectrodes[198, 205-207]. Webster e*t al.* [198] created a 5 µm reference electrode on a chip using standard photolithography and physical vapour deposition to obtain miniaturized Pd metal electrodes that could be fabricated in a single metal patterning step and integrated inside a fluidic sensor assembly. Fleischmann *et al.*[207] reported PdH electrodes prepared by loading bare Pd wires with hydrogen cathodically and afterwards coated the curved part of the cylindrical surface with Lacomit varnish. They reported that the PdH electrode was placed within 20 µm of the working electrode and that it gave a stable potential for periods up to 24 hours. Imokawa *et al.*[206] were the first to report a successful PdH microelectrode in terms of the quality of the potentiometric response (stability, reproducibility, etc.). Using the mesoporous electrodes, (e.g. a thin Pd film over a Au or Pt microelectrode), Imokawa *et al.*[206] made hydrogen loading easier. However, the *lifetime* of the electrodes was shorter than in the other examples due to the small amount of hydrogen loaded.

(a) The hydrogen adsorption process

The hydrogen electrode reaction on the metal surface of palladium is a multistep reaction which can be described by the Volmer-Heyrovsky-Tafel mechanism[208]. The first step is the formation of adsorbed hydrogen on the electrode surface in the Volmer reaction (19): the charge transfer is followed by the adsorption of hydrogen atoms on surface active sites (hollow site for underpotentially deposited hydrogen, HS, or on-top position for overpotentially deposited hydrogen, OTP):

$$H^+ + e^- + M_{surface} \underset{\overleftarrow{k}_{-1}}{\overset{\overrightarrow{k}_1}{\rightleftharpoons}} MH_{ads,OTP} \tag{19}$$

This is followed by hydrogen evolution reaction, HER, according to the electrochemical process, Heyrovsky reaction (20) or the chemical recombination desorption process, Tafel reaction (21):

$$MH_{ads,OTP} + H^+ + e^- \underset{\overleftarrow{k}_{-2}}{\overset{\overrightarrow{k}_2}{\rightleftharpoons}} M + H_2 \tag{20}$$

$$2MH_{ads,OTP} \underset{k_{-3}}{\overset{k_3}{\rightleftharpoons}} 2M + H_2 \tag{21}$$

where k_i are the rate constants and the arrows above them denote potential dependent forward and backward rate constants. These reactions might also be accompanied by the underpotentially adsorption of hydrogen, HS:

$$H^+ + e^- + M_{surface\ voids} \underset{\overleftarrow{k}_{-1,HS}}{\overset{\overrightarrow{k}_{1,HS}}{\rightleftharpoons}} MH_{ads,HS} \tag{22}$$

Lynch and Flanagan[209] postulated the presence of two adsorbed states of hydrogen (weakly and strongly chemisorbed, as in platinum) with different metal-hydrogen bond strengths. It has been suggested that weakly chemisorbed hydrogen might be located in subsurface interstitial sites and thus a precursor to absorbed hydrogen. The hydrogen electrode reaction at palladium is further complicated by extensive permeation of atomic hydrogen into the metal lattice to form α PdH and β PdH. In general, the HS hydrogen is supposed to take part in the absorption reaction[180, 208, 210-212]. In the literature, no consensus has been found about the mechanisms by which hydrogen enters into the metal and in which way the adsorbed hydrogen is an intermediate between the adsorbed and absorbed process. **Figure 1.4** shows a voltammogram recorded at 10 mV s^{-1} after the activation of the H_1-e Pd (the films are termed H_1-e to indicate that they were electrodeposited from the H_1 lyotropic liquid crystalline phase made with the method proposed by Bartlett *et al.*[213]) was completed in order to present the characteristic features of the nanostructure in the hydrogen and oxides region. According to Bartlett[213] and Birry[211], the labelled peaks in the hydrogen region correspond to (a) HS adsorption and (f) desorption of hydrogen, the start of hydrogen (b) absorption and (e) desorption in the α PdH, the start of the hydrogen (c) absorption and (d) desorption for the β PdH. In the oxygen region the peaks can be attributed to (I) the metal oxides formation and (II) the reduction of the oxides. The well resolved pair of peaks a-f corresponds to the formation and removal of adsorbed hydrogen atoms at the Pd surface; this corresponds to the Volmer reaction (19). The evidence for the attribution of these peaks to the hydrogen adsorption is given in an experiment shown in **Figure 1.7** in which an inhibitor for the adsorption of hydrogen is added in the solution in order to suppress the reaction producing the peaks a-f. Despite extensive research conducted with a variety of methods to study the electro-oxidation of Pd, many aspects of the process still remain poorly understood, first of all the type of oxides formed. A critical review on this topic has been written by Grden *et al*.[214]. It is important to notice that the nanostructure is fundamental in the resolution of the peaks related to surface processes: with bulk palladium the potential region of the hydrogen adsorption overlaps with that of hydrogen absorption and the separation of these processes requires special structures of the catalyst. Similar peaks have been observed by Baldauf, Kolb[215, 216] and Czerwinski[180, 217-219] in their studies with ultrathin palladium films (order of 1-500 ML) and for small palladium particles, but they never obtained the same resolution as Attard *et al.*[220] and Bartlett *et al.*[213] observed for catalysts with H_1 structure[213, 221-223].

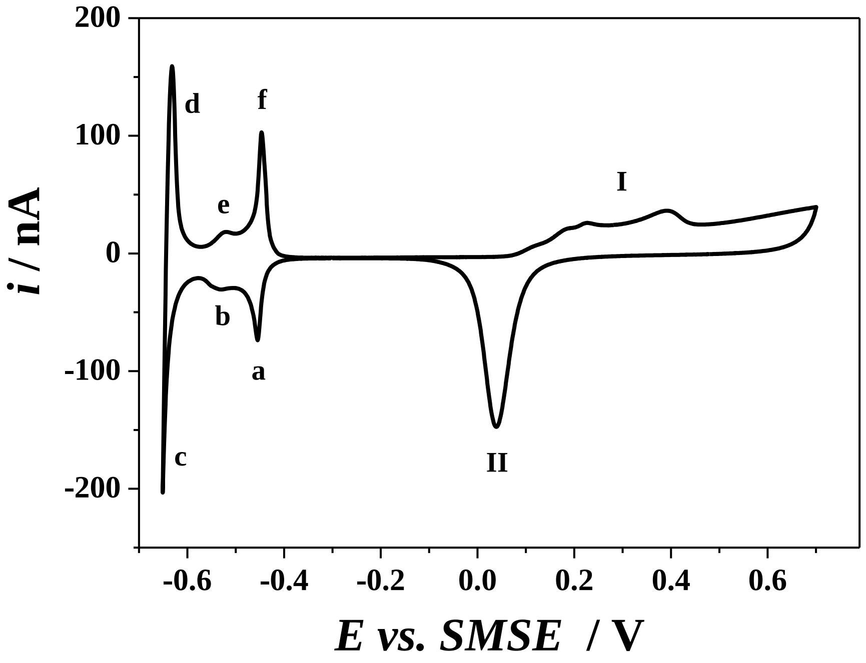

Figure 1.4 Cyclic voltammogram of an H_1-e Pd film (Q_{dep} = 10 C cm^{-2}) deposited on a platinum disc electrode ($2a$ = 10 µm) recorded in 1 M H_2SO_4 at ν = 10 mVs^{-1}. The labelled peaks in the hydrogen region correspond to (a) HS adsorption and (f) desorption of hydrogen, the start of hydrogen (b) absorption and (e) desorption in the α PdH, the start of the hydrogen (c) absorption and (d) desorption for the β PdH. In the oxygen region the peaks can be attributed to (I) the metal oxides formation and (II) the reduction of the oxides[211, 213].

(b) The hydrogen absorption process

The H_1-e Pd electrodes allow the simultaneous study of bulk and surface reactions. As demonstrated by Baldauf and Kolb[216] for ultrathin Pd layers (< 3 ML), hydrogen absorption does not occur, so it is possible to discriminate the signal that originates from the adsorption alone. However, for ultrathin electrodes, the response is significantly influenced by the underlying electrode on the voltammetric profile. The distinction between the peaks related to surface and bulk processes can be made with the help of certain surface poisons which adsorb on the electrode surface and influence the processes of hydrogen adsorption. Baldauf and Kolb investigated the influence of crystal violet adsorption on hydrogen electrosorption in acidic solutions. These studies were continued by Bartlett and Marwan[221, 222], Birry and Lasia[211] and Duncan and Lasia[210, 224, 225]. It has been observed that in the hydrogen adsorption region, currents were strongly decreased due to crystal violet adsorption, while the absorption process became electrochemically more reversible. It was concluded that crystal violet adsorption inhibits hydrogen adsorption, but the kinetics of absorption is significantly enhanced. Birry and Lasia[211] made a comparison of the hydrogen absorption isotherms, expressed as atomic ratio in function of the loading potential $H/Pd(E_L)$, in presence and absence of 10^{-4} M of crystal violet in a solution of 0.1 M H_2SO_4 for different amounts of electrodeposited palladium; they observed that (i) the amount of *H/Pd* is similar for all the layers and practically independent of the presence of crystal violet and (ii) the differences in the isotherms appear at very thin layers (< 20 ML) where the adsorption charges constitute an important part of the H total charge. Nevertheless, in the presence of crystal violet the adsorption charge is negligible, leading to reproducible values of *H/Pd* even for different deposition thicknesses.

Even if the Pd-H system has been studied for years, there is still no agreement about the mechanism of the absorption reaction. Multiplicities of studies in the last 10 years suggest that the hydrogen absorption reaction may proceed by two mechanisms[208]:

i. Indirect absorption mechanism in which hydrogen is first adsorbed on the electrode surface in the Volmer step as OTP (19) and HS (22). The equation (19) is followed by absorption in the subsurface layer at a distance $x = 0$ from the interface and consequently in the bulk of the metal:

$$MH_{ads,OTP} + M_{subsurface} \underset{k_{-4}}{\overset{k_4}{\rightleftharpoons}} MH_{abs,0} + M_{surface} \tag{23}$$

$$MH_{abs,0} \rightarrow MH_{abs,x} \tag{24}$$

where M $_{subsurface}$ and M $_{surface}$ are the empty subsurface and surface sites.

ii. Direct hydrogen absorption in which protons are reduced to form the subsurface absorbed hydrogen (25):

$$H^+ + e^- + M \underset{\overleftarrow{k}_{-6}}{\overset{\overrightarrow{k}_6}{\rightleftharpoons}} MH_{abs,0} \tag{25}$$

This reaction may be accompanied by the hydrogen HS and OTP reactions and the HER.

It is not certain which mechanism is responsible for the hydrogen absorption and if in the hydrogen adsorption Eq. (22) or Eq. (23) are the limiting steps. It is usually assumed that in electrochemical studies the direct path is faster in palladium catalysts. The same authors[210] suggested the scheme of the hydrogen absorption mechanism in palladium reported below:

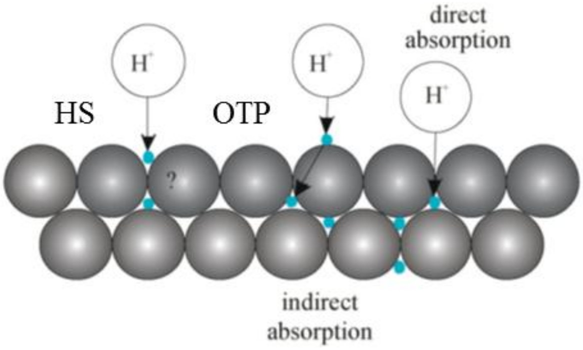

Figure 1.5 Mechanism of the hydrogen absorption in palladium. Taken from[210]

Recently, Lukaszewski and Czerwinski[180] have summarized selected aspects of the electrochemical investigation on hydrogen absorption in palladium limited volume electrodes:

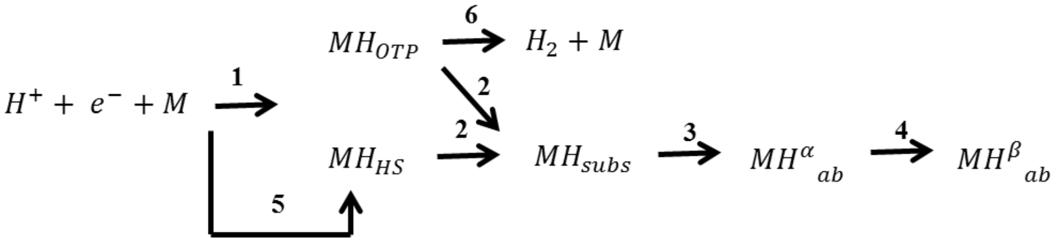

Figure 1.6 The steps of hydrogen electrosorption proposed in Pd LVEs are: (1) Volmer reaction, i.e., charge transfer followed by the adsorption of H atoms on surface active sites (hollow site for H $_{HS}$ or on-top position for H $_{OTP}$); (2) transfer of atomic hydrogen (H $_{HS}$ or H $_{OTP}$) from the surface through the interface to an interstitial position in a subsurface layer (H $_{subs}$); (3) diffusion of hydrogen from the subsurface layer to the bulk of the metal, where a particular phase of absorbed hydrogen is formed; (4) phase transition between the α- and β-phases of absorbed hydrogen; (5) charge transfer followed by the transfer of atomic hydrogen to an interstitial position in a subsurface layer, without the adsorption step (direct absorption); (6) discharge of adsorbed H atoms (only H $_{OTP}$) in an electrochemical process (Heyrovsky reaction) or a chemical recombination process of H atoms (Tafel reaction), both leading to the hydrogen evolution reaction. According to the above scheme, the two main mechanisms of hydrogen absorption can be considered, namely, the so-called indirect absorption path and the direct absorption path.[180]

The peaks (b and c) in **Figure 1.4** are associated respectively with the start of the formation of the α Pd-hydride and β Pd-hydride phases. When the potential is scanned to more cathodic values, it is possible to observe the entire formation of the β Pd-hydride phase (cathodic scan) and its oxidation (anodic scan); this voltammogram is the black one shown in **Figure 1.7**. The recorded voltammograms are extremely helpful in the understanding of the adsorption and absorption processes; therefore they are introduced in the introduction chapter. The behaviour of the H_1-e Pd films in acidic solution has been observed with the addition of 1 mM of crystal violet in order to investigate the absorption process. **Figure 1.7** shows the comparison between voltammograms recorded in the presence, *red*, and absence, *black*, of the poison. In the voltammograms recorded in 1 M H_2SO_4, at the potential -0.46 V on the cathodic scan, the peak corresponds to the formation of the adsorbed hydrogen which is oxidised in the anodic scan at -0.44 V (peaks a-f in **Figure 1.4** or II in **Figure 1.7**). The addition of 1 mM of crystal violet in the solution almost suppresses the presence of this peak confirming that it is due to the formation of adsorbed hydrogen at the metal surface. It is more interesting to observe that in presence of crystal violet (i) the absorption region is significantly shifted to more anodic potentials, (ii) the peaks separation between the reduction and oxidation processes is shorter, (iii) the oxidation peak is much sharper than in absence of the poison and (iv) the charge under the oxidation peak in presence and absence of the poison is not significantly different. These evidences in the voltammograms confirm that the kinetics of the hydrogen absorption in the presence of crystal violet is significantly enhanced and that hydrogen HS is not the only process participating in the hydrogen absorption into the palladium lattice. The fact that the charge under the hydrogen oxidation peak remains unchanged suggests a direct absorption mechanism. The recorded voltammograms are identical to those reported in Marwan's work[222].

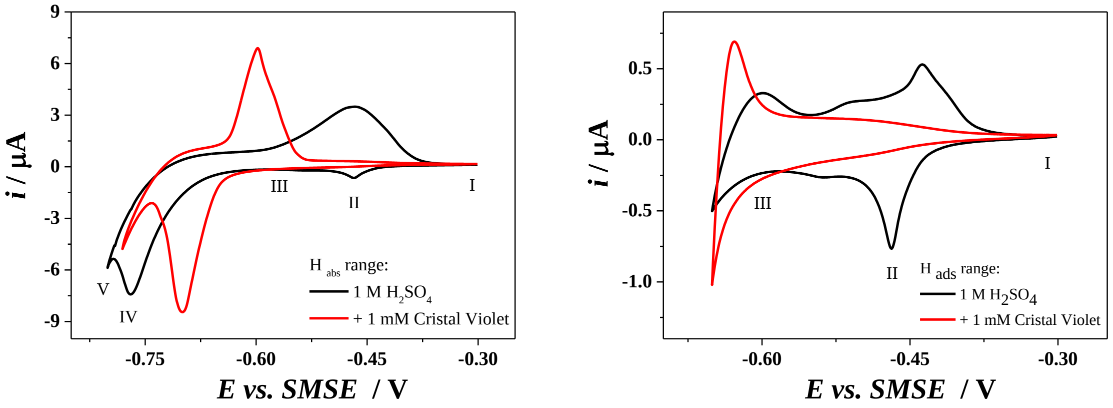

Figure 1.7 Cyclic voltammograms of an H_1-e Pd film (Q_{dep} = 10 C cm^{-2}) deposited on a platinum disc electrode (2a = 25 µm) recorded in 1 M H_2SO_4 at ν = 50 mV s^{-1} without, *black*, and with, *red*, 1 mM crystal violet. (left) potential range for the whole hydrogen region E = [-0.8; -0.3] V[222] and (right) the potential range for the hydrogen adsorption region E = [-0.65; -0.3] V. The labelled peaks in the hydrogen region correspond to (I) double layer zone, the start of hydrogen HS (II), the start of absorption in the α PdH (III) and β PdH (IV) phase, and the hydrogen evolution (V)[211].

(c) The phase transition in the palladium hydride

The most important mechanism in the present study is the phase transition between α Pd-hydride and β Pd-hydride phases. The composition at the solid state of the hydride during the transition from the β to the α phases does not affect the potential of the electrode. Beside, this potential only depends on the pH of the solution:

$$E_{PdH}\,vs.\,SHE = +50\,mV - 59.2\,mV\,pH \qquad \text{at 25 °C} \quad (26)$$

A complete derivation of this equation is presented in chapter 7. From the schemes above, it is clear that the hydrogen electrosorption in palladium is a complex event consisting in several and parallel paths. In the study of hydrogen transport, the interpretation of the current due to the reduction and oxidation of hydrogen usually assumes that a single reaction step is much slower than all the others, so that reaction purely controls the rate of the overall reaction. Depending on the experimental conditions, different steps can be the rate limiting one in the electrosorption process, but a mixed control may occur as well. In the literature, two mechanisms of phase transition have been considered: the first is based on a nucleation and growth model while the second follows a moving phase boundary model. Zhang *et al.* [226] and Lee and Pyun[227] developed a model for the movement of an α-β boundary inside palladium, leading to discontinuous concentration gradients of hydrogen. In these models, the insertion/extraction of ions into/from the metal host lattice leads to different composition between the outer layers and the bulk. In the absorption process at potentials low enough for the β phase to be formed, after a rapid initial formation of the α phase, the β phase appears in the subsurface region with a phase boundary moving from the surface to the bulk of the electrode. It was suggested that in the presence of both α and β phases, the slowest process that controls the rate of the overall electrosorption reaction in ultrathin palladium layers is the phase transition [226, 228]. Numerous studies have been made on the extraction of hydrogen from the metal lattice by anodic polarization. In the present study, only the spontaneous diffusion out of the saturated bulk palladium has been taken into account. This event has been studied by applying zero current at the electrode (*OCP*). This event is produced by a low partial pressure (~ 0 Pa) of hydrogen dissolved in the solution, which shifts the equilibrium between absorbed, adsorbed and gaseous hydrogen in the direction of the desorption[229]. It has been generally observed that traces of oxygen present in the solution may affect this process. This has been confirmed during bulk and SECM experiments reported below in chapter 3 and 4.

It is generally accepted that the absorption into palladium leads to physical changes. In **Table 1.1** the physical proprieties of the palladium hydride are summarised.

Table 1.1 Summary of the physical properties of the palladium hydride.

Properties	Palladium	α phase	β phase
Lattice structure[230]	f.c.c.	f.c.c.	f.c.c.
Lattice constant[231]	3.882	3.882-3.886	4.017-4.031
Diffusion coefficient of hydrogen	-	$\approx 2\ 10^{-7}$ cm^2 s^{-1}	$\approx 2\ 10^{-6}$ cm^2 s^{-1}

The palladium hydrogen electrode therefore exhibits the unique propriety to be able to measure the pH of the surrounding solution. For this reason, we wanted to try it in SECM configuration to track local pH changes.

1.5. Scanning Electrochemical Microscopy

Scanning electrochemical microscopy is a very useful technique for the investigation of surfaces ranging from conductive to insulating properties. The technique employs an ultramicroelectrode (UME), also known as a tip, to scan in close proximity to the surface of interest [232]. The tip current is a function of the solution composition, the distance between the tip and the surface of the substrate and the state of the substrate itself [233]. The beauty of the SECM is that it can be used to obtain valuable information about local surface conductivities, morphologies, concentration profiles, maps of reactive sites. It can be used to modify and structure conducting and insulating surfaces at the micro- and nano-scale [234]. In addition, one of the main point of this technique is that it can be used as an imaging tool: the images can be obtained by monitoring the probe response as it is scanned across the substrate; these images provide information about the chemical and electrochemical activity at the substrate surface, as well as the substrate topography[233].

1.5.1. Historical Background

Bard *et al.*[235-237] in 1989 introduced the principles of scanning electrochemical microscopy. The paper describes the methodology for characterising processes and structural features of a surface immersed in a solution. Studies on electrodes that were moved over a surface and electrochemical scanning tunnelling microscopy studies were published earlier in parallel works by Engstrom[238-241] and Bard[242]. The SECM as electrochemical tool engages two different research issues that are the use of microelectrodes in electrochemistry and the application of piezoelectric elements to position the tip, like in scanning tunnelling microscopy (STM). Microelectrodes applications cover a wide area in the electrochemical research; therefore SECM is also able to incorporate a large number of experiments and techniques. SECM came from the realisation that the steady state current at a microelectrode is affected by the presence of a substrate that perturbs the diffusion layer of the tip. SECM has been extensively used to monitor the concentration of various species such as H_2O_2[243, 244], Ag^+ and I^-[245] and H^+[246-249]. It has also been possible to measure indirectly the dissolution of MnS from stainless steel [250]. The redox mediator I^-/I_3^- was used by Paik *et al.*[250] to measure the product of the dissolution HS^- and $S_2O_3^{2-}$. Scanning electrochemical microscopy has been widely used for electrodeposition of metals[251-260], metal oxides[261, 262] and biological substances[263-265].

1.5.2. Principles of SECM

SECM belongs to the group of scanning probe microscopes, a group that also includes scanning tunnelling microscopy (STM) and atomic force microscopy (AFM). As for these techniques, the SECM has a tip (an ultramicroelectrode) that is held by a three dimensional micropositioner above the sample surface. The tip and the substrate are both immersed in an electrolyte solution with a redox mediator. The fundamental principle of the technique is to control the electrochemistry of the tip and measure the electrochemical response when the tip is brought to the surface of the substrate. Earlier, the tip was moved by inchworm drivers or inchworm drivers combined with piezoelectric pushers which allowed work with nm resolution. Nowadays it is more common to use stepper motors, often with a piezoelectric pusher on the z-axis, to move the three dimensional stages with high positioning accuracy.

The SECM technique provides two modes for the probe to characterize the electrochemical response of the sample surface.

In the potentiometric mode[63], the tip acts as a passive probe measuring either the distribution of potential at the interface or the local concentration of specific ions (e.g. dissolving metal ions during galvanic corrosion)[266]. Using the Nernst Eq.(8), the local concentration of the ion of interest (averaged over the sensing region) can be calculated from the electrochemical response of the tip. Scanning the surface, the tip produces an image that is only dependent on the concentration profiles of the species it encounters without producing or consuming any species. Since the sensor is passive, only the substrate generator-tip collection (the “generation/collection principle”, GC, is cited below) measurements are possible [63].

The amperometric mode is the most popular mode of SECM because the tip acts as an active probe producing the diffusion layer which interacts with the sample surface. Therefore, experiments can be performed in a variety of ways. When a microelectrode at a sufficient positive potential is immersed in a solution containing species that can be oxidized, if the reaction is kinetically controlled by the diffusion of reduced species from the bulk to the electrode surface, the diffusion layer of the reduced species grows around the tip. After a short time ($\triangle t \approx \frac{a^2}{D}$ where a is the radius of the tip and D is the diffusion coefficient of the reduced species) the shape of the diffusion layer becomes stable and the steady state current $i_{T,\infty}$ is obtained (27):

$$i_{T,\infty} = 4\,n\,FDc^{\infty}a \tag{27}$$

where c^{∞} is the concentration in the bulk for the reduced species.

There are several modes of operation using the tip as an active probe. When the tip is moved near a surface, different reactions can occur due to the nature of the surface. If the diffusion layer at the tip is perturbed by the presence of a substrate, this is the basis of the feedback mode[63]. When the tip is brought near an electrically insulating surface, the substrate blocks the diffusion of reduced species to the tip and the current i_T decreases compared with that recorded in the bulk $i_{T,\infty}$. The closer the tip gets to the substrate, the smaller i_T becomes and this decrease in current with the distance is the *negative feedback* also called hindered diffusion. The *positive feedback* occurs when the tip is brought near a conductive substrate, while there is still the blockage of the diffusion of the reduced species to the tip by the substrate; there is also the reduction of the species oxidized by the tip at the surface-substrate. These new reduced species diffuse to the tip causing an increase in the flux, so the tip current is bigger than that in the bulk. The negative and positive feedback steady-state currents are shown in **Figure 1.8**.

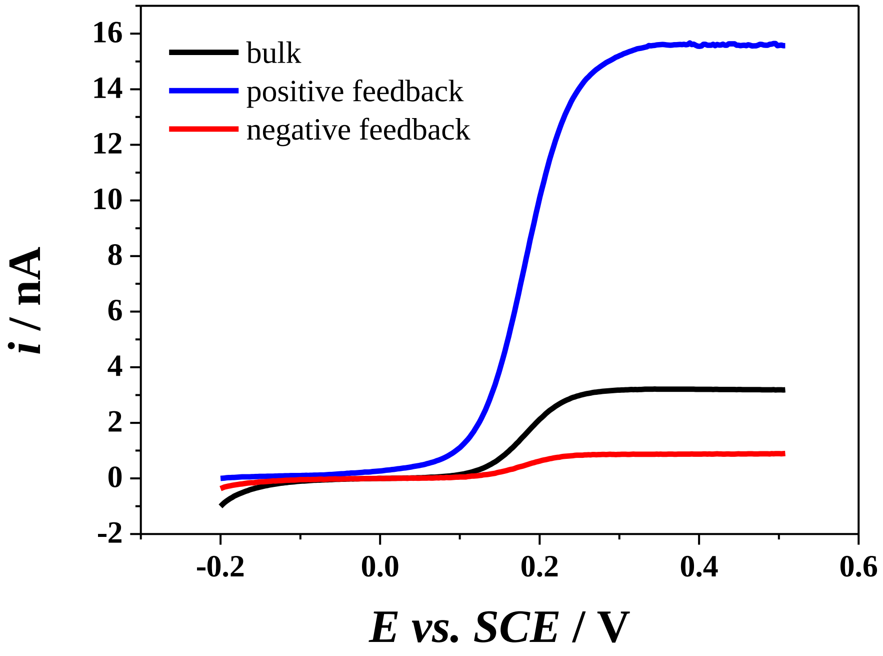

Figure 1.8 Steady state voltammograms recorded with a nominal Pt 25 µm ⌀ as WE at ν = 2 mVs^{-1} in a stagnant solution of 1 mM FcMeOH + 0. 1 M KCl in the potential window [-0.2 V; +0.65 V]. **Black:** Steady state current in the bulk, **blue:** close to a conductive substrate and **red:** close to an insulator.

In the GC mode, the microelectrode tip or the substrate surface consumes the species generated by the other. For this reason, there are two different GC configurations: (i) the tip generation/substrate collection (TG/SC) and (ii) the substrate generation/tip collection (SG/TC). In the first case, the tip is held at a potential where the reaction occurs and the substrate is held at a different potential at which the product of the tip reacts and is detected. Normally for stable species the collection efficiency is 100% because in most cases the substrate is larger than the tip. In the SG/TC mode, the tip detects the reaction that occurs on the substrate surface[63]. With this approach, many interesting studies about the adsorption and desorption kinetics of protons on ionic single crystal surfaces were carried out by Macpherson and Unwin[267-269], who demonstrated the possibility of inducing and monitoring dissolution processes from a single crystal surface *via* potential step chronoamperometry.

The SECM can also be used to modify the substrate surface in a direct way or in the microreagent mode [63]. In the latter case, the tip generates ions that diffuse towards the surface changing the local environment of the substrate. In the direct mode the tip is used as a small secondary electrode and the deposition or the etching of the substrate is confined in a small region determined by the tip. The main advantages of active probes over passive probes are that they can be sensitive to different redox species present in the solution and the fact that it is possible to access the tip-substrate distance.

The most popular solid electrodes for SECM are microdisc tips with diameter of 0.6-25 µm, that are achieved by sealing a microwire into a glass capillary and polishing the end until a mirror finish. The RG (ratio between the radius of the glass and the radius of the electrode) of the electrode is typically below 10.

1.5.3. Potentiometric probes in SECM

The potentiometric mode of SECM requires an independent determination of the absolute distance between the microelectrode and the sample surface. This is because the probe is usually very fragile and it is important to restrict its travel to avoid touching the sample. Furthermore, the potentiometric response of the tip does not hold the tip-substrate distance dependence found in the amperometric mode. Quantitative information regarding the concentration profiles can only be extracted with the knowledge of the tip-substrate distance. The tip position is precisely known only relative to a reference location in the solution. In the amperometric mode the probe acts like an electrochemical radar that produces/consumes redox species and the resulting concentration gradient in the tip-substrate gap yields a unique tip current-distance dependence. In the potentiometric mode the tip is passive and does not interfere with the concentration profiles except by shielding the sample surface from the bulk solution. Therefore different procedures need to be proposed to assess the tip-substrate distance in these conditions. The simplest consists in approaching the tip under visual observation with a microscope until it is seen to barely touch the substrate surface. This tip is then assumed as the zero on the tip-substrate distant scale, but this method is not very accurate [270].

As previously mentioned, the metal oxide potentiometric devices have different advantages. They can sustain Faradic reactions and therefore operate in the conventional amperometric mode when provided with a redox mediator in the solution. An approach curve can be recorded in the conventional feedback mode to assess the tip-substrate distance. Subsequently, the tip can be electrochemically reconditioned to perform potentiometric measurements. Following this approach, it is possible to have an accurate and precise control of the tip position. Horrocks *et al.*[131] and Toth *et al.*[99] recorded the steady state current for ORR on antimony microdisc and showed that the current decreases when moving the electrode close to an inert substrate. The tip potential was held in the plateau region for the ORR and the approach curve was then recorded from the bulk to the substrate so as to avoid crashing the tip. After returning to the bulk, the tip potential was held well positive of the ORR in order to regenerate the antimony oxide and re-establish the pH function. After few seconds, the tip was switched to potentiometric mode to record pH profiles and maps over the substrate. This approach is only possible with solid-state ISEs and only with those rapidly electrochemically regenerated. Unless removed by purging, oxygen is always present in the solution and it alleviates the need for addition of a redox mediator that could interfere with the potentiometric signal. Moreover, the normalization of the approach curve with the limiting current in the bulk removes the need for the knowledge of the bulk concentration and diffusion coefficient of oxygen. Csoka and Mekhalif[271] prepared recently a double function electrode for imaging copper ion concentration profiles. It was fabricated from a 25 µm platinum disc electrode in a glass capillary where the Pt was dissolved to obtain a small cavity that was filled with a carbon paste modified with diethyl-thiuram-disulfide ionophore. In the potentiometric mode, the electrode acted as a copper ISE with 16 s of response time. In the amperometric mode using dissolved oxygen as redox mediator the tip current could be used to estimate the tip-substrate distance. This approach was used to follow copper dissolution and the dissolution rate could be estimated from tip potential versus tip-substrate distance curves [270].

1.5.4. Applications of potentiometric pH detection in SECM

The most common of all the applications is to monitor pH profiles near electrodes, corroding surfaces or membranes. Klusmann and Schultze[249] made a comparison between theoretical and experimental pH profiles near planar and microdisc electrodes for constant flux and constant concentration sources. They also investigated the spatial resolution for pH mapping. Horrocks *et al.*[131] reported the results of SECM experiments where potentiometric pH-selective tips were used to image local pH changes in several systems like platinum microelectrodes during water reduction. A detailed investigation of proton concentration profiles close to silver-iodide based ion-selective membranes was reported by the same authors[99]. pH measurements were carried out in the vicinity of a semi permeable membrane operating in a chlor-alkali cell[137]. The tip consisted in two channels one filled with antimony to form pH-sensing disc and the other was left open to act as a Luggin capillary and eliminate the effect of the iR drop. This study showed the extent of penetration and leakage of hydroxides through the membrane. Similarly, pH profiles were recorded near bilayer lipid membranes with antimony microelectrodes[136]. pH measurements were also performed in the vicinity of a cathode evolving hydrogen gas using an antimony microelectrode[133]. The effect of a buffering agent, glycine, was investigated. Tanabe *et al.*[272] used potentiometric and amperometric SECM techniques to investigate the ionic environment above pits on stainless steel surfaces. They reported the detection of Cl^- with Ag/AgCl tips and protons with a 7 µm diameter carbon fibre, but the principle of detection of proton with the carbon fibre is not clear. Park et al. fabricated double barrel tips and probed the OH^- build-up generated by cathodic reactions on Al_3Fe in contact with Al 6061 in a galvanic cell. Luo *et al.*[165] also reported the fabrication of potentiometric pH tips to investigate localised corrosion. Micro-pH-sensitive iridium oxide electrodes with diameter less than 10 µm were developed by El-Giar and Wipf[273]. The electrode was fabricated from a glass micropipette having a tip opening of a few micrometres. A sonicated suspension of iridium microparticles in methanol was introduced into the tip. After the settling down and evaporation of the methanol, the particles were sintered to form a solid iridium cone inside the tip. Potential cycling in sulphuric acid at 3 V s^{-1} was employed to form the pH sensing oxide film on the iridium disc. The application of these pH-sensitive microelectrodes was demonstrated by imaging the pH changes due to the ORR at the surface of a cast iron sample. Mirkin *et al.*[101] used Sb microelectrodes to perform amperometric and potentiometric experiments near living cells. The pH was probed potentiometrically while the topography and redox activity of the cells were probed amperometrically. The topography was determined with hydrophilic mediators as they cannot penetrate the cell membrane; in contrast, the redox activity was determined with hydrophobic mediators that can permeate across the cell membrane. The use of a single tip to probe intracellular redox activities and pH changes provides valuable information when investigating biochemical processes. However, the control of tip-substrate distance was found to be challenge since biological specimen are soft, not flat and can be easily damaged by the scanning probe.

1.6. Structure of the thesis

Chapter 2 identifies all the reagents, instrumentation and standard experimental procedures which were used throughout the project. Chapter 3 introduces palladium hydride electrodes and their potentiometric signal is studied in detail in different atmospheres, with a particular attention reserved for solutions in which a oxidizing agent is introduced. Chapter 4 details the work conducted with SECM in order to have an insight of the reactions happening on the sensor in presence of oxygen. Chapter 5 presents a real case in which the palladium hydride sensors were used to monitor the carbonation of lime within a porous mesh. Chapter 6 reviews the achievements produced during this research project and lists possible paths for future work. In Chapter 7, appendices, the thermodynamic treatment of the potential in the miscibility gap is carefully explained, the most used procedures in NOVA are listed and an attempt of the electrogeneration of the portlandite crystals is presented.

2. Experimental

2.1. Reagents

This chapter contains the details behind all the undertaken experiments. Unless otherwise stated, all the reagents were used as received without further purification. See Table 2.1 for details. The water used to prepare solutions and to clean the glassware was deionized from a Whatman Still and RO50 water purification system (resistivity 18.2 M Ω cm^{-2}).

Table 2.1 List of the reagents used in experiments. RE: reference electrode.

Name	**Chemical Formula**	**Manufacturer**	**Purity**	**Use**
Alumina powder	Al_2O_3	Buehler		Polishing
Ammonium Tetrachloropalladate (II)	$(NH_4)_2PdCl_4$	Aldrich	97%	Plating mixture
Argon	Ar	Boc gases	99.9%	Purge gas
Brij® 56	$C_{16}H_{33}(OCH_2CH_2)_nOH$	Aldrich	n/a	Plating mixture
Calciumchlorite	$CaCl_2$	Fisher	97%	Test solution
Calcium hydroxide	$Ca(OH)_2$	IBZ-Salzchemie GmbH & Co.KG	25 g/l	Sample
Carbon dioxide	CO_2	Boc gases	99.9%	Purge gas
Chloridric acid	HCl	BDH	37-38%	Test solution
Crystal violet	$C_{25}H_{30}N_3Cl$	Aldrich	ACS reagent	Test Solution
Ferrocenemethanol	FcMeOH	Aldrich	97%	Test Solution
Heptane	C_7H_{16}	Lancaster	99%	Plating mixture
Hexachloroplatinic acid	H_2PtCl_6 xH_2O	Aldrich	99.9%	Deposition solution
Mercurous chloride	Hg_2Cl_2	Alfa Aesar	95%	RE
Mercurous sulphate	Hg_2SO_4	BDH	99.5%	RE
Mercury	Hg	Alfa Aesar	99.9998%	RE
Oxygen	O_2	Boc gases	99.9%	Purge gas
Potassium chloride	KCl	Fisher	99.5%	Electrolyte
Potassium chloride	KCl	BDH	Analar	RE
Potassium sulphate	K_2SO_4	BDH	Analar	RE
Sodium hydroxide	NaOH	BDH	96%	Test Solution
Trisodium phosphate dodecahydrate	Na_3PO_4 $12H_2O$	Sigma Aldrich	>98%	Test Solution
Disodium hydrogen phosphate dodecahydrate	Na_2HPO_4 $12H_2O$	BDH	Analar	Test Solution
Sodium dihydrogen orthophosphate dihydrate	NaH_2PO_4 $2H_2O$	Fisher	99.2%	Test Solution
Sodium sulphate	Na_2SO_4	Sigma	99.0%	Test Solution
Sulphuric acid	H_2SO_4	BDH	95%	Test Solution

All glassware used was soaked overnight in a 5 % Decon 90 (BDH) and deionised water solution and washed thoroughly at least 3 times with deionised water and then dried in a drying oven at 40 °C before the use.

2.2. Preparation of the solutions for pH measurements

2.2.1. Phosphate buffers

Phosphate buffers (0.02 M, ionic strength (I_s) = 200 mM, 100 ml) over the entire pH scale were prepared, according to the Liverpool buffers table[274] using an acid component with deionised water (90 ml). Na_2SO_4 was added to ensure the ionic strength of the buffers was 200 mM. The solutions were then titrated using aliquots of NaOH (0.1 M) at room temperature to the required pH. For pH 14, 1 M NaOH was used as a buffer.

As the buffers were prepared at room temperature but used at 25 °C the pH of each buffer was re-recorded using a water-jacketed cell at 25 ± 0.5 °C using the glass electrode pH probe. As the glass electrode is deemed to be inaccurate at a pH greater than 12, buffers past this pH range were unable to be measured reliably under temperature-controlled conditions.

2.2.2. Neutralization of 1 M NaOH with H_2SO_4

A few experiments were carried out in a solution of 1 M NaOH (pH = 14) in which different aliquots of 5 M, 1 M and 0.1 M H_2SO_4 were added to decrease rapidly the pH to lower values. The resulting the pH was calculated theoretically for the equilibrium between the strong base and the strong acid used.

2.2.3. Titration in a solution containing 1 M NaOH and 50 mM Na_3PO_4

The potentiometric titration was done in a solution of 1 M NaOH in which the salt Na_3PO_4 was added.The pH values were calculated taking into account the dissociation of the phosphates:

$$PO_4^{3-} + H_2O \rightleftharpoons HPO_4^{2-} + OH^- \qquad K = 0.0467 \qquad (28)$$

2.3. Scanning electron microscope

The scanning electron microscope used was a Philips XL30 ESEM microscope. It was predominantly used in the “wet mode” so as to prevent charging up of the glass or other insulators surrounding the metallic electrode. To take the images of interest, the gaseous secondary electron detector (GSE) was used in order to have the morphological features of the electrode. The images were predominantly taken at two different angles such as the view perpendicular to the electrode and a side view approximately at 70°. In this way it was possible to check the quality of the electrode surface, its homogeneity, the smoothness of the tip's insulator and the radii of the insulator and of the electrode.

2.4. Electrochemical instrumentation

All the measurements took place with the cell enclosed in a grounded Faraday cage in order to minimize the electromagnetic interferences. Electrochemical experiments were carried out with the Galvanostat / Potentiostat Autolab PGSTAT101 with NOVA 1.6 and NOVA 1.9. Some were recorded with a homemade high impedance differential amplifier for open circuit potential measurements (OCP). For scanning electrochemical microscopy (SECM), the tip was positioned using a system supplied by Physik Instrumente (PI) GmbH & Co. and consisting of three high-accuracy translation stages (model M-605) mounted as X-Y-Z combination axes and controlled by three DC-Servo-Motor Controller (model C-863). The travel ranges were 25 mm with an integrated 0.3 µm resolution linear encoder. The motor controllers were connected through a daisy chain and with a USB port to a personal computer. The axes were controlled by the PI MikroMove software. A video microscope was used to observe the relative location of the tip with respect to the substrate. This device was not used to measure distances but to avoid tip-substrate crashes. Rotating disc electrode (RDE) experiments were carried out with an AFCPRB Rotator supplied by Pine Instrument Company.

2.5. Electrochemical cells

Several cells with different shapes and functionality were used during this study:

- 15 ml water-jacketed glass cells had five or three necks to insert the electrodes and purge the solution, shown in **Figure 2.1**. When the constant temperature of 25°C was kept, the necks of the jacket were connected to a Grant W14 thermostat. The tubing for the bath was surrounded with a grounded wire mesh to prevent the conduction of electrostatic noise. When necessary, the required gas for the experiment was bubbled for 15 minutes prior to measurements and was kept as a blanket by allowing the gas to flow over the top of the solution without causing any disturbance to the surface of the liquid during the recording;

Figure 2.1 Picture of a 15 ml water-jacketed glass cell with five necks.

- a normal platinum mesh supported on glass made up the cell for electrodeposition within the surfactant template. The grid was used as CE and it was usually spread with the template mixture. The RE and WE were then inserted in the viscous mixture. The cell is shown in **Figure 2.2** without the plating mixture;

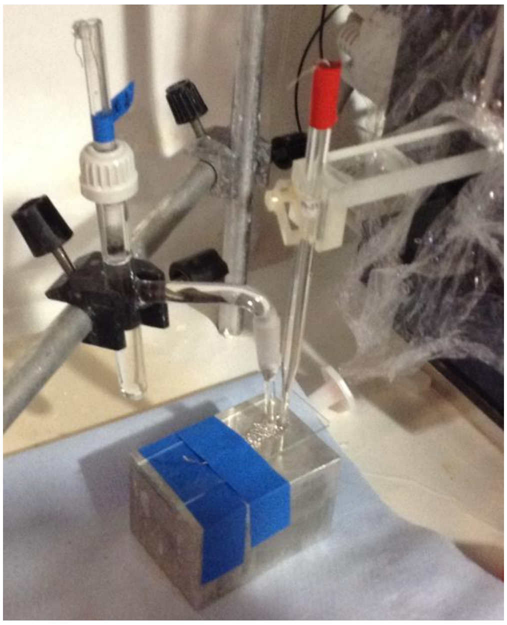

Figure 2.2 Picture of the cell for the electrodeposition of the Pd nanostructure with the RE (blue), CE (Pt gauze resting on the glass slide) and WE (red).

- the open Perspex® cell shown in **Figure 2.3**, was used for the carbonation experiments. The saturated calcium hydroxide solution was absorbed in small strips (3 mm wide × 1 cm long) of cellulose mesh (lens cleaning paper, pure cellulose supplied by Whatman) under thermostatic conditions (23°C) and with different Ar/CO_2 gas mixtures. The cellulose mesh was used for three reasons: to trap a thin film of solution and thus simulate carbonation in the confinement of a porous medium, to provide an ionic path between the electrodes and to analyse the solid phases formed during the carbonation. The reference electrode was clamped outside the cell and connected to the solution via a salt bridge (Agar saturated with K_2SO_4) attached to the body of the microelectrode and terminated by a capillary tip flushed with that of the microelectrode. This configuration was implemented to guarantee a constant distance between the pH sensing tip and the reference electrode and thus avoid Ohmic distortion while galvanostatically loading the microelectrodes with hydrogen. The cell contained up to 3 ml solution and had a removable lid (inset in **Figure 2.3**) designed to clamp the counter electrode at the bottom of the cell and prevent any movement during the tests. The two long side walls of the cell were made from glued microscope slides to facilitate inspection of the mesh and electrodes positions. The pH sensing electrode and attached salt bridge were introduced into the cell after closure of the lid, through a circular opening in the lid. At the bottom of the cell a plastic capillary was connected to a syringe to allow the removal of the solution. Gas mixtures were introduced in the cell via a glass pipette inserted through a second hole in the lid. The gas mixtures, oxygen free Ar and CO_2, were streamed into the cell through a thermostated humidifier (pure water) to ensure the cellulose mesh never dried out. Specific p_{CO2} were obtained by adjusting the valves and flow meters detailed in **Figure 2.3**. Each cylinder was connected to a flow meter that allowed a specific flow for each gas and, consequently, a specific volume or a partial pressure. The gas blend was homogenised in a mixing chamber and the stream was split between an exhaust line and a feed line regulated by a flow meter set at 0.25 L min^{-1}. The exhaust valve was adjusted to avoid gas overpressure within the system.

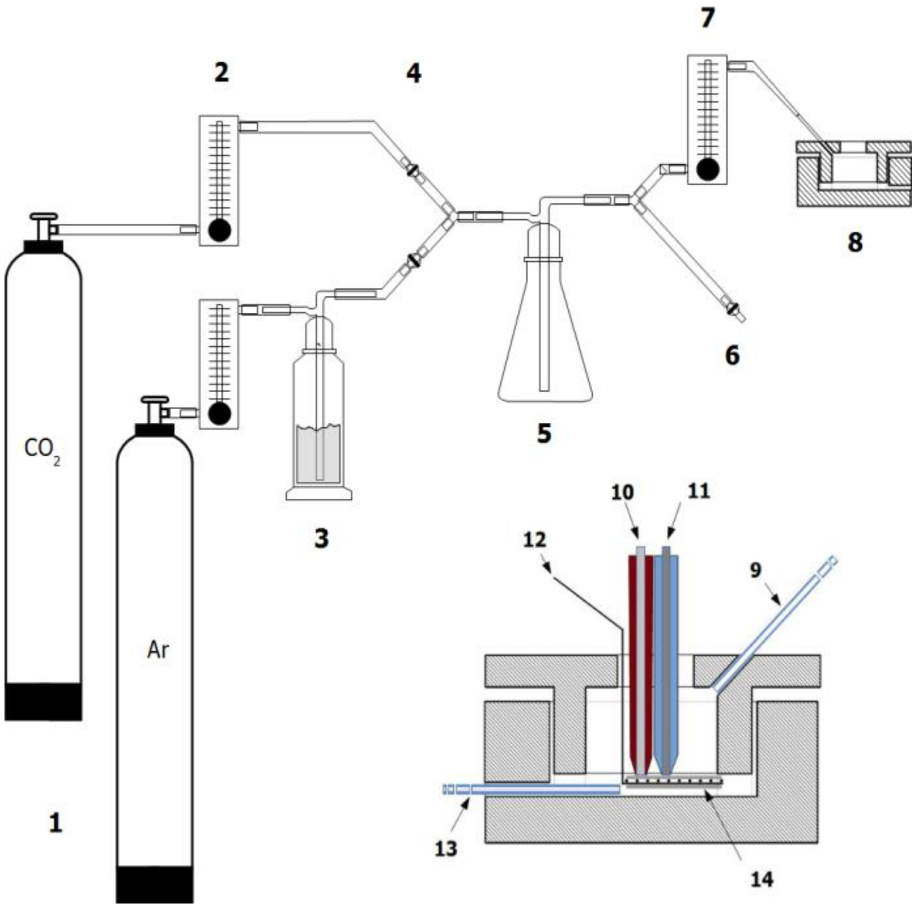

Figure 2.3 Design of the cell used in the experiment reported in chapter 5. The main U body of the cell was built in Perspex® sandwiched with microscope slides. Schematic of the experimental assembly: (1) gas cylinders, (2) flow meters, (3) humidifier, (4) valves, (5) mixing chamber, (6) exhaust line and valve, (7) flow meter and regulator (8) cell, (9) gas mixture injector, (10) reference electrode salt bridge, (11) pH sensing electrode, (12) counter electrode, (13) capillary to remove the solution, (14) cellulose mesh.

- the cells for SECM measurements had less traditional shapes because they need geometrical properties in order to fit in the most suitable way all the electrodes. The most used are:
    - a Perspex® cell (**Figure 2.4**) with two walls made of microscope glass slides and in which the bottom could be covered with a glass slide;

Figure 2.4 Picture of the Perpex® cell with a RE in order to illustrate the size of the cell body.

- a cell screwed on the EQCM holder for the electrodeposition of the desired metal on the quartz crystal electrode, **Figure 2.5**.

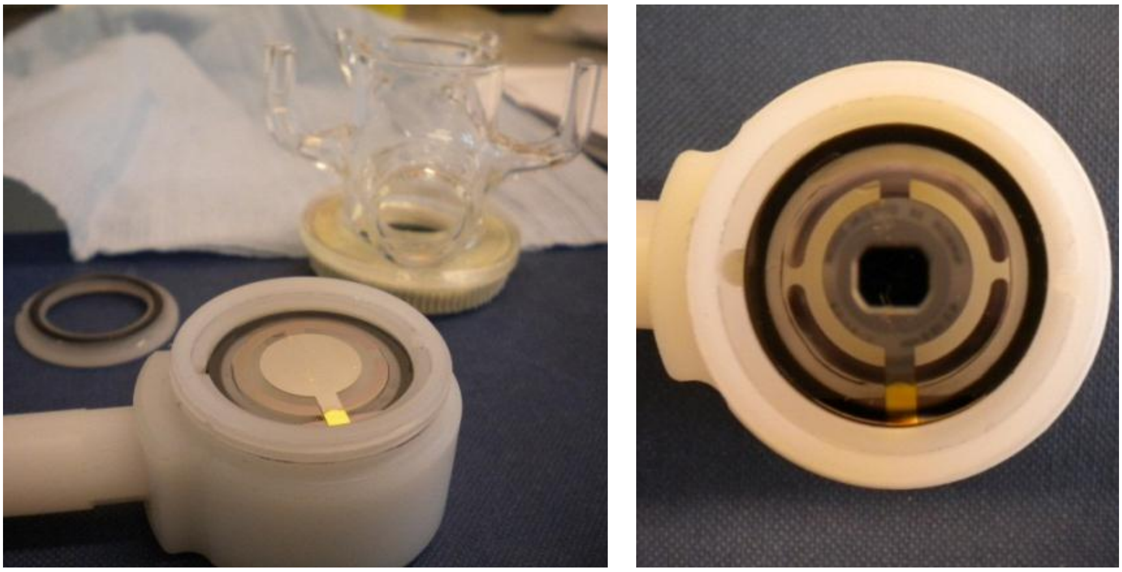

Figure 2.5 Cell used during the plating of the gold electrode with platinum. The substrate is fitted in the EQCM holder. The deposit of platinum on gold is smooth and shiny. A small part of gold is still visible because it is shielded by the crystal retainer during the deposition.

2.6. Electrodes

2.6.1. Reference electrodes

Two different electrodes were used in this work: saturated calomel electrodes (SCE) and saturated mercury/mercurous sulphate electrode (SMSE).

Homemade Hg/Hg_2SO_4, saturated K_2SO_4 electrodes (SMSE) were used in most experiments instead of SCE to prevent Cl^- ion contamination into the test solution. The electrodes were prepared according to the procedure proposed by Bartlett[275]. The electrodes were a combination of two glass pieces: one piece was a tube with one end closed and through which a platinum wire was sealed and a piece like a pipette with sintered glass at the very tip. Drops of liquid mercury were placed into the glass tube until the platinum wire was completely covered. A paste made of K_2SO_4/Hg_2SO_4 1:1 was then placed on the liquid mercury and everything was held by glass wool inserted into the tube. The tube was then inserted in the pipette filled with the saturated solution of K_2SO_4 solution. The homemade SMSEs were stored, soaked in saturated K_2SO_4 solution and rinsed before use.

Homemade Hg/Hg_2Cl_2, saturated KCl electrodes (SCE) were used as reference electrodes in experiment with solutions containing Cl^- ions. The preparation procedure was the same as for the SMSE, except that K_2SO_4 was replaced with Hg_2Cl_2 and K_2SO_4 by KCl. The homemade SCEs were stored soaked in saturated KCl solution and rinsed with purified water before use.

In the experiments with the micro-positioning system, the reference electrodes used were SMSE with an Agar salt gel bridge obtained with a saturated solution of K_2SO_4 + 1% of Agar. The salt agar mixture was soaked into a capillary in order to obtain a salt bridge that could be clamped with the working electrode with PTFE tape to minimize the iR drop during the SECM measurements.

All reference electrodes were tested regularly against a hydrogen electrode in order to have the correct potential difference with respect to SHE.

2.6.2. Counter electrodes

Two counter electrodes were used in this study: a platinum mesh with a dimension of 1 cm^2 and a large (4 cm^2) platinum gauze. The first was used in a three electrode configuration for voltammetry, chronoamperometry and chronopotentiometry, while the latter was used as the counter electrode and the support of the electroplating mixture in a three electrode configuration for the electrodeposition of mesoporous palladium, according to the procedure reported by Bartlett *et al.*[213]

2.6.3. Working electrodes

Microelectrodes where prepared according to the procedure described by Denuault [276]. Platinum microwires (5, 10, 25 and 50 µm diameters, 99.99% Goodfellow Metals) were inserted in borosilicate glass pipettes and the end of the pipettes was sealed using the flame of a Bunsen burner. Once sealed, the open end of the pipette was attached to a vacuum using a piece of tubing and the sealed end of the pipette was inserted into a heating coil and heated. This caused the glass to melt and collapse around the wire. The heating coil was gradually moved until 5 mm of microwire was left exposed to air at the top of the glass. After cooling and opening the vacuum line, finely cut indium was then inserted into the glass body until it covered the microwire. The glass tip was warmed gently until the indium melted. A copper wire (15 cm long x 500 µm diameter) was then inserted into the molten indium and twisted to ensure a good connection. On cooling, the indium was re-solidified and provided the connection between the microwire and the connecting wire. The pipette was then removed from the coil, allowed to cool down and the copper wire was fixed by the use of a quick set epoxy resin placed around the open part of the pipette so as to remove any strain on the connection.

Before their use, the microelectrodes were polished using decreasing roughness of emery paper (silicon carbide paper 320, 600 and 1200) and then on velvet polishing pads (Buehler) with alumina (5.0, 1.0, 0.3 and 0.05 µm) water slurries on a microcloth in order to have a mirror finish surface. Between the uses of the different polishing papers the electrode was rinsed with deionised water and cleaned in the ultrasonic bath with water to remove any residues of the polishing pad. Then the electrodes were transferred to 1 M H_2SO_4 solution in which cyclic voltammetry measurements were carried out until a stable voltammogram was obtained.

For SECM experiments, the microelectrodes need to be coned (polished as a truncated cone) in order to reduce the thickness of the insulating glass surrounding the microwire radius. Usually the tips have an RG (ratio between the insulator radius, r_g, and the microwire radius, a) of 10 or less. This is a very important factor in SECM experiments because the RG is a critical parameter which determines the amount of diffusion around the corner of the glass and therefore it needs to be well estimated in order to compare the experimental results with the simulated curves. A large RG also makes the experiments more difficult because any error in the alignment may result in a tip crash during the approach or the scanning. The RG of the electrode was estimated by taking a GSE image of the tip in the ESEM in order to have the ratio between the measured insulating glass and the metal radii. To obtain a truncated cone, the electrodes were ground by hands on a lapping machine using Al_2O_3 lapping films of 5, 1 and 0.3 µm. In between the different lapping films, the electrode was rinsed in acetone to remove any residues of the plastic binder of the lapping film. Another essential feature is that the microwire needs to be concentric with the entire tip in order to prevent asymmetric behaviours during the electrodeposition and the SECM experiments.

In order to test the diffusional proprieties of the microelectrodes, steady state cyclic voltammograms were recorded in a solution containing 2.5 mM FcMeOH and 0.25 M KCl at 2 mVs^{-1}. **Figure 2.6** shows typical CVs for different microelectrodes. **Figure 2.7** shows that the relationship between the limiting current and tip radius is linear as expected from the theory ($i_L = 4nFDc^{\infty}a$). The determination of the diffusion coefficient from the slope of the line and gives $D \approx 7.15\text{x}10^{-6}$ cm^2s^{-1}.

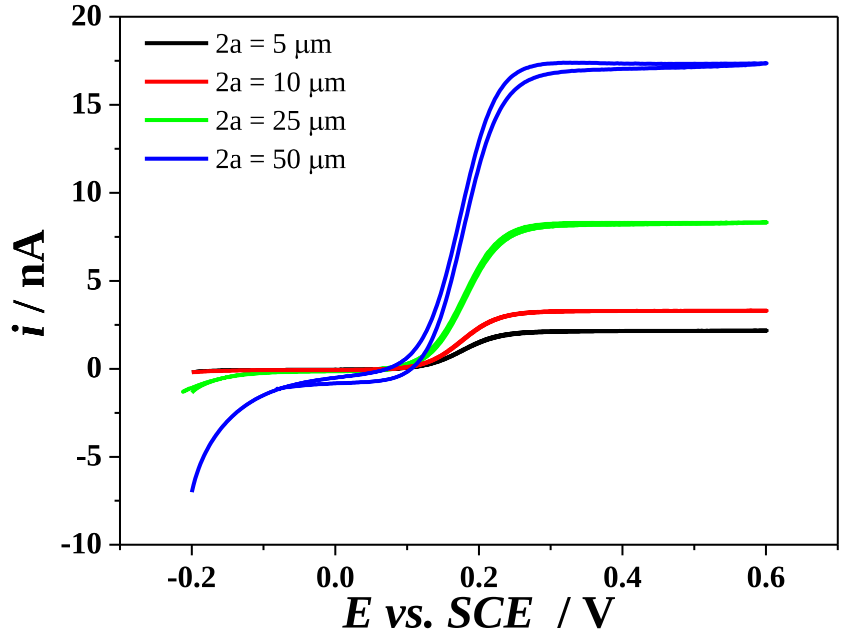

Figure 2.6 Steady state voltammograms recorded in aerated 2.5 mM FcMeOH + 0.25 M KCl solution for a series of platinum microdisc radii at 2 mV s^{-1}.

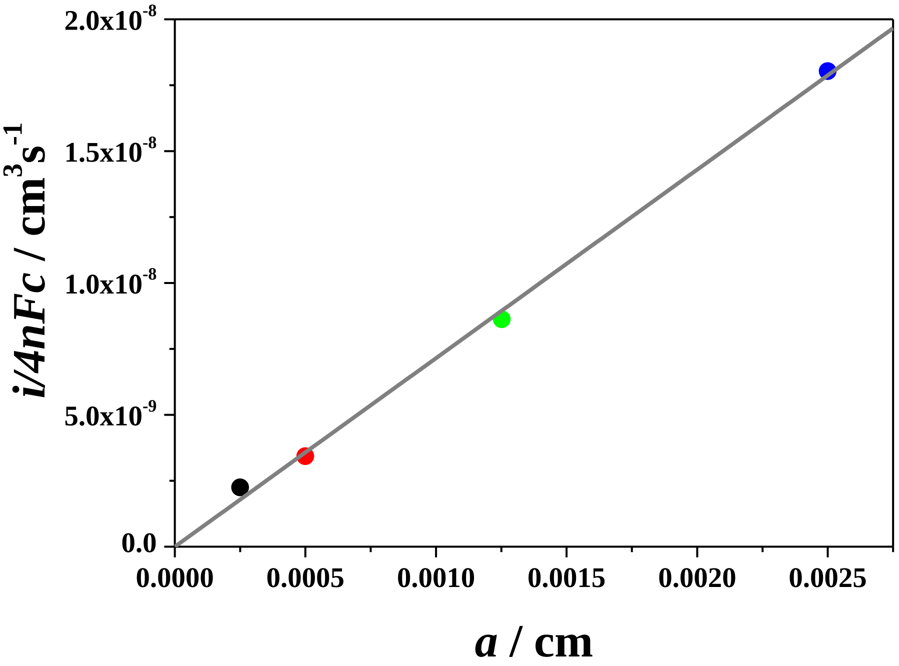

Figure 2.7 Plot of the limiting current *vs.* microdisc radius for the data reported in **Figure 2.6** the gradient of the plot is the diffusion coefficient of the species. The straight line is the line of the best fit.

2.7. Deposition and characterization of the palladium film

2.7.1. Preparation of the plating mixture

The plating mixture for the nanostructured palladium deposition was prepared as described previously by Bartlett *et al.* [213] and consisted of 12% wt. $(NH_4)_2PdCl_2$, 39% wt. H_2O, 47% wt. Brij® 56 and 2% wt. heptane. These conditions produce the hexagonal phase H_1 of the surfactant shown in the phase diagram in **Figure 2.8**. The water and palladium salt were combined in a glass container followed by the addition of the heptane and the surfactant Brij®. Upon stirring the mixture became very viscous and turned a red/ brown colour. The mixture was sealed in a glass container using Parafilm to prevent any changes in concentration during heating as this can change the phase obtained. The mixture was homogenised by gently heating for 30 minutes at 40 ºC, causing the mixture to become less viscous and then allowed to cool to room temperature. The mixture was then stirred before repeating the heating/cooling processes twice more.

To determine the phase structure of the lyotropic liquid crystals, the texture of the plating mixture was observed using a polarising optical microscope (Olympus BH2 equipped with a heating stage). A small amount of the plating mixture was sandwiched between a glass slide and a cover slip and placed between two crossed polarisers that were perpendicular to one another. This allowed for the optical texture of the plating mixture to be determined as the anisotropic effect of the hexagonal phase of the plating mixture changes the polarisation of the light. The mixture was then heated until a phase change was seen (~ 60 ºC) i.e. when no light was transmitted through the mixture. This is because the cubic and micellar phases are optically isotropic and cannot be viewed with the polarised light microscope[277]. Upon cooling to room temperature the sample appeared to have a feather like appearance, which is characteristic of the hexagonal phase (H_1), shown in **Figure 2.9**. The hexagonal phase is anisotropic, alters the polarisation of the light and can be seen under polarised light.

The hexagonal phase was further characterised using a drop of water on the slide as the hexagonal phase dissolves in water whereas the lamella phase is insoluble in water. The difference in the hexagonal and lamella phase could have also been distinguished by the difference in viscosity between the two phases, as the hexagonal phase is much more viscous than the lamella phase [278].

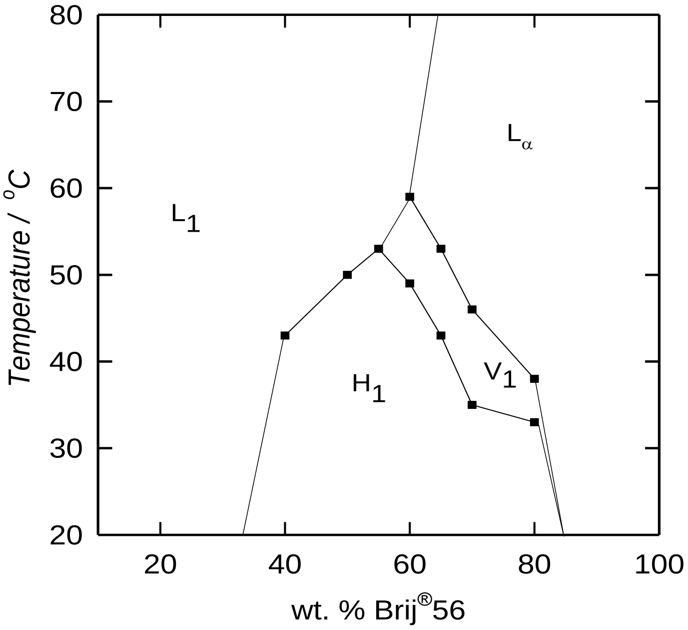

Figure 2.8 Phase diagram for mixtures of a 1.40 mol / l solution of $(NH_4)_2PdCl_4$ in water, Brij®56 and heptane. The ratio between $(NH_4)_2PdCl_4$ / water (0.4) and surfactant / heptane (22) was kept constant. The composition (by weight) of surfactant in the aqueous solution was increased from 20 to 80%. H_1 is the hexagonal phase, V_1 the cubic phase, L_α the lamellar phase and L_1 the micellar solution. Taken from[221]

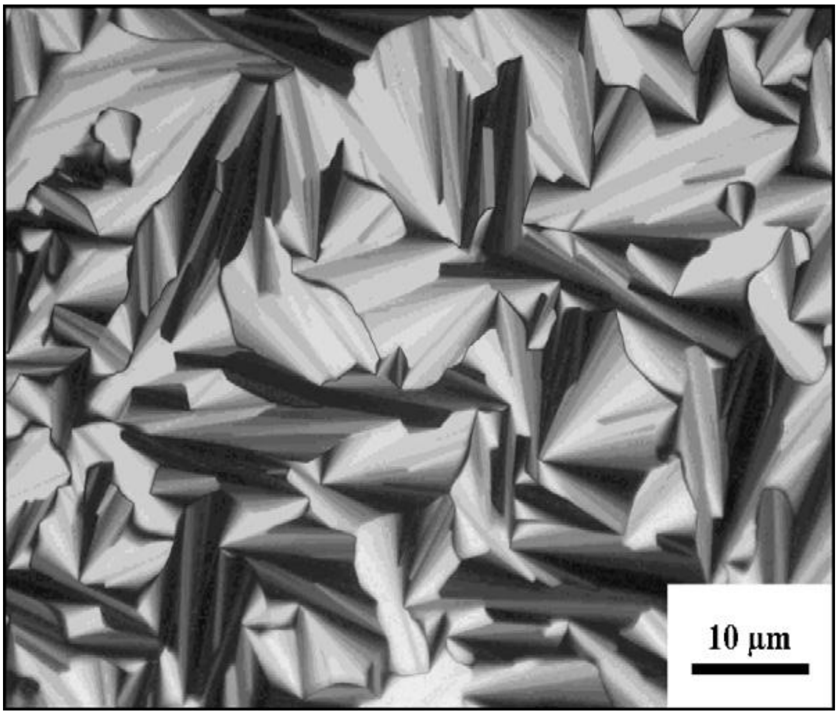

Figure 2.9 Polarized-light optical microscopy (POM) image of H_2PtCl_6: Brij56 liquid crystalline phase. Taken from Zhong *et al*.[279]

2.7.2. Electrochemical deposition of H_1-e Pd film on platinum microdiscs

The deposition of the nanostructured film of palladium onto platinum microdiscs (generally roughness factor, R_f, ~ 2 [280]) from the template mixture[213] was carried out by sweeping the potential, *cyclic voltammetry*, and by potential step, *chronoamperometry*. The palladium salt was mixed with the non-ionic surfactant (Brij® 56), water and heptane in order to obtain the template mixture for the deposition of the mesoporous Pd films. No supporting electrolyte was added to the solution as this could influence the existence of the liquid crystalline phases and disrupt the pores arrangement. A platinum mesh and homemade saturated calomel electrode (260 mV *vs.* SHE) was used as counter and reference electrodes respectively. The working and reference electrodes were inserted closely together in the template mixture pasted onto the counter electrode.

Figure 2.10 shows the current and the charge recorded during the deposition of the palladium by cyclic voltammetry in the first three scans. The potential was swept at 2 mV s^{-1} between 0.05 and 0.4 V starting with the cathodic sweep. The increase in the cathodic charge is due to the reduction of the Pd(II) to Pd(0) to form the film. The reduction starts to be observed at 0.2 V during the first scan, but with the increase of the amount of Pd deposited (following scans), the reduction potential progressively shifts to more anodic potentials. The amount of palladium electrodeposited from each cycle can be estimated by the respective deposition charge. The absence of any anodic charge during the sweeps indicates that the deposited Pd is not oxidised and re-reduced; this is due to the potential range chosen during the experiment. The total amount of Pd deposited during the cycles shown, assuming 95% deposition efficiency[222], corresponds to a charge, q_{dep}, of 50.51 µC.

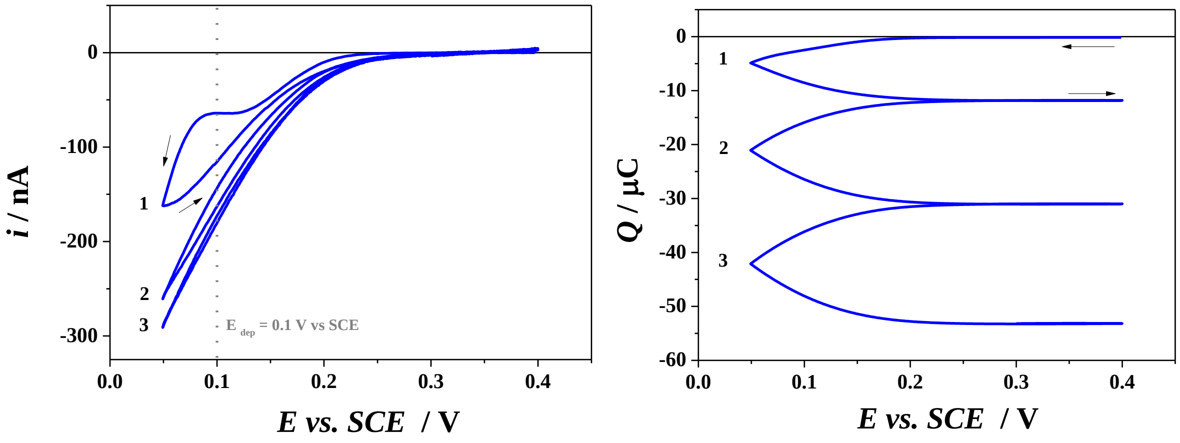

Figure 2.10 Electrodeposition of H_1-e Pd on a platinum microdisc ($2a$ = 50 µm) by cyclic voltammetry. The potential was scanned at $\nu = 2$ mV s^{-1} in the potential range E = [0.05; 0.40] V *vs.* SCE in a plating mixture of 12 wt.% $(NH_4)PdCl_4$, 47 wt.% Brij® 56, 39 wt.% water and 2 wt.% heptane at room temperature[213]. (left) First three cycles recorded, (right) charge recorded for each cycle. q_{dep} = -53.17 µC.

Figure 2.11 shows the current and the charge recorded during the deposition of the palladium by chronoamperometry. The potential was stepped from the OCP to a value in in the double layer region, DL, (E_{DL} = 0.4 V) where no reaction occurs at an appreciable rate, to the value (E_{dep} = 0.1 V) where the steady state current of the reduction had been observed during the first cycle in **Figure 2.10** until the desired charged had been passed. The reduction current rises to nearly -60 nA immediately after the potential step as a result of the double layer charging. The current decreases then to reach -35 nA after 42 s and then it increases again to reach -65 nA at the end of the experiment. The measurement was stopped when the desired amount of charge density had been reached (Q_{dep} = 2 C cm^{-2}).

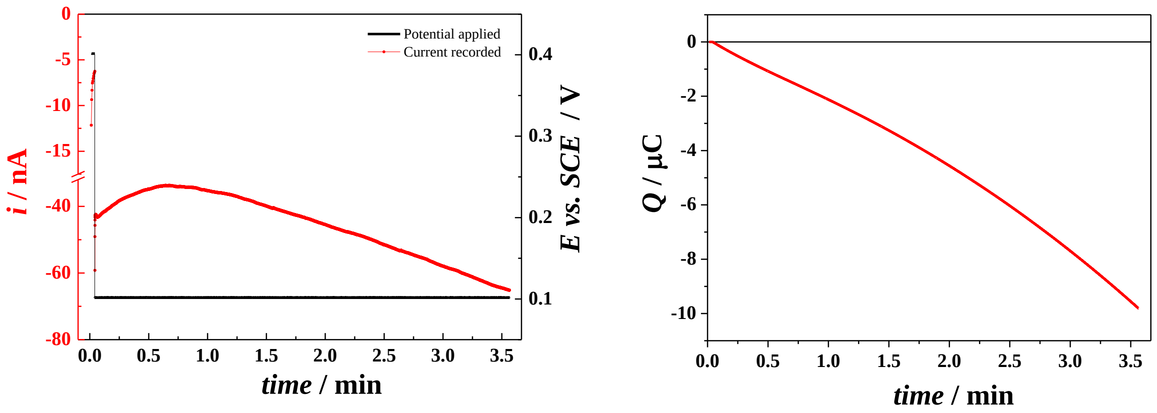

Figure 2.11 Electrodeposition of H_1-e Pd on a platinum microdisc ($2a$ = 25 µm) by chronoamperometry. The potential was stepped from the OCP to the double layer region for 5 s (E_{DL} = 0.4 V) and then at E_{dep} = 0.1 V until the desired charge has been passed. The plating mixture was the same plating mixture solution used for the experiment shown in Figure **2.10**[213]. (left) Potential step applied and current transient recorded during the electrodeposition, (right) charge recorded after stepping to the plating potential. Q_{dep} = -9.81 µC.

When the films are deposited from the lyotropic liquid crystalline phase, the pores in the palladium are initially filled by the surfactant. Prolonged washing in water (circa 24 hours) is compulsory to remove the surfactant from the pores. Nerveless, the surface of the pores is never completely clean so the catalyst needs to be activated by sweeping the potential in the electrolyte potential region until stable voltammograms are obtained (usually at ν = 100, 50 and 10 mV s^{-1}). The catalyst was activated in a solution of 1 M H_2SO_4 in which a platinum mesh was used as counter electrode and a homemade SMSE as reference (703 mV *vs.* SHE). Cyclic voltammetry in acid solutions was systematically used to characterise the electrochemistry of the H_1-e Pd films[213].

Figure 2.12.left shows a set of voltammograms recorded for a freshly prepared H_1-e Pd film which was soaked in water for 4 days and then transferred to 1 M H_2SO_4 solution. The potential was swept starting from the double layer region (E = - 0.3 V) with the cathodic sweep in order to see the formation of adsorbed and absorbed hydrogen. On the anodic scan, first the oxidation of the hydrogen occurs and at more anodic potentials it is possible to observe the formation of the surface oxides. On the return (E = 0.05 V) the surface oxides are removed giving rise to a well-defined stripping peak in the voltammetry. It is possible to observe that the Faradic peaks increase in size with respect to each successive cycle. This event occurs as the surfactant, originally in the pores, diffuses out and is replaced by the acid solution. As this happens, the surface area in contact with the solution increases and the electroactive surface area increases as well. As

the amount of Pd deposited increases, the activation takes more time/cycles because the film grows in thickness and the pores become longer. Marwan [221] observed with EQCM measurements on the H_1-e Pd film that dissolution of palladium starts with the formation of the surface oxides at around 0.1 V *vs.* SMSE on the anodic cycle and continues until 0.05 V *vs.* SMSE on the cathodic cycle when the oxides is stripped from the electrode surface. In order to avoid any ageing of the nanostructured by this dissolution, repeatedly cycling of the electrodes into the oxide formation region was avoided.

Figure 2.12.right shows a voltammogram recorded at 10 mVs^{-1} after the activation of the H_1-e Pd was completed. It presents the characteristic features of the nanostructure in the hydrogen and oxide regions [206, 213]. According to Bartlett [213] and Birry [211], the labelled peaks in the hydrogen region correspond to (a) HS adsorption and (f) desorption of hydrogen, the start of hydrogen (b) absorption and (e) desorption in the α PdH, the start of the hydrogen (c) absorption and (d) desorption for the β PdH. In the oxygen region the peaks can be attributed to (I) the metal oxides formation and (II) the reduction of the oxides.

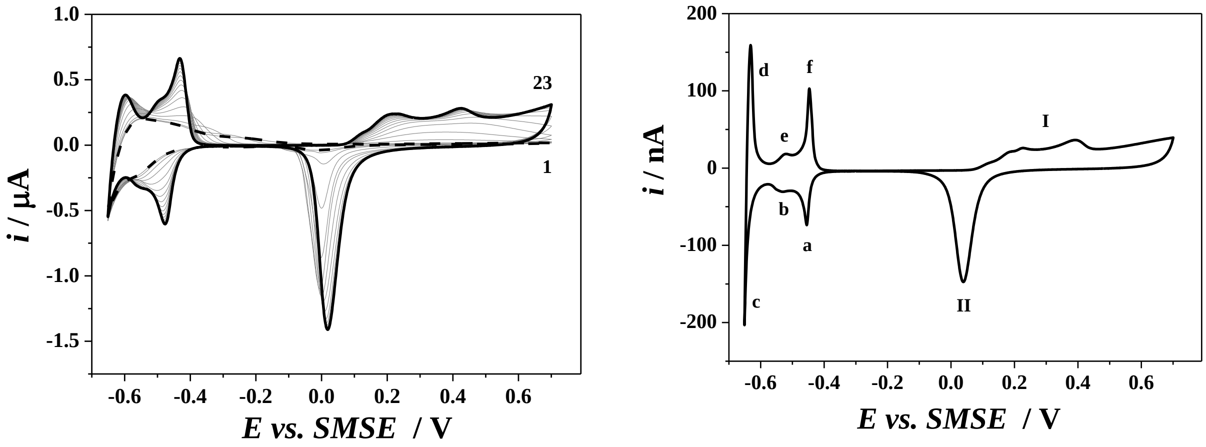

Figure 2.12 Cyclic voltammograms of an H_1-e Pd film (J_{dep} = 10 C cm^{-2}) deposited on a platinum disc electrode (2*a* = 10 µm) recorded in 1 M H_2SO_4 at (left) ν = 100 mV s^{-1} and (right) ν = 10 mV s^{-1}. (left) The increase in the current recorded in subsequent cycles during the activation of the catalyst is associated with the gradual removal of the surfactant from the pores. The numbers identify the scans. (right) The labelled peaks in the hydrogen region correspond to (a) HS adsorption and (f) desorption of hydrogen, the start of hydrogen (b) absorption and (e) desorption in the α PdH, the start of the hydrogen (c) absorption and (d) desorption for the β PdH. In the oxygen region the peaks can be attributed to (I) the metal oxides formation and (II) the reduction of the oxides. [211, 280]

The charge associated with the removal of the oxide layer was used to measure the electroactive area of the palladium film. The stripping charge of the oxide was estimated by integrating the peak II, dividing the value with the scan rate in order to obtain a charge and dividing the last value for the charge of one monolayer of oxide (424 µC [281]). In order to know the roughness factor of the electrode, the electroactive area was divided by the geometrical area of the electrode. The latter was measured either by steady state voltammetry in FcMeOH or in degassed $(NH_3)_6RuCl_3$ or by taking an image of the film with the ESEM.

The electrodeposition of nanostructured palladium was mostly carried out by chronoamperometry, nevertheless the same results can be achieved by the galvanostatically by fixing a current for a defined period of time in order to pass the desired charge for the electrodeposition. Results in **Figure 2.13** show there is no difference in one or the other approach regarding the activity of the catalyst. In the potentiostatic mode, the potential was held (at 0.1 V) until the desired charge of 10 µC has been passed (red graph) and in the galvanostatic mode (blue graph) the current was fixed for a defined amount of time (50 nA for 200 s); in both cases identical characterization voltammograms were obtained. The potentiostatic electrodeposition is usually preferred to the galvanostatic one because the latter may produce non uniform films[282].

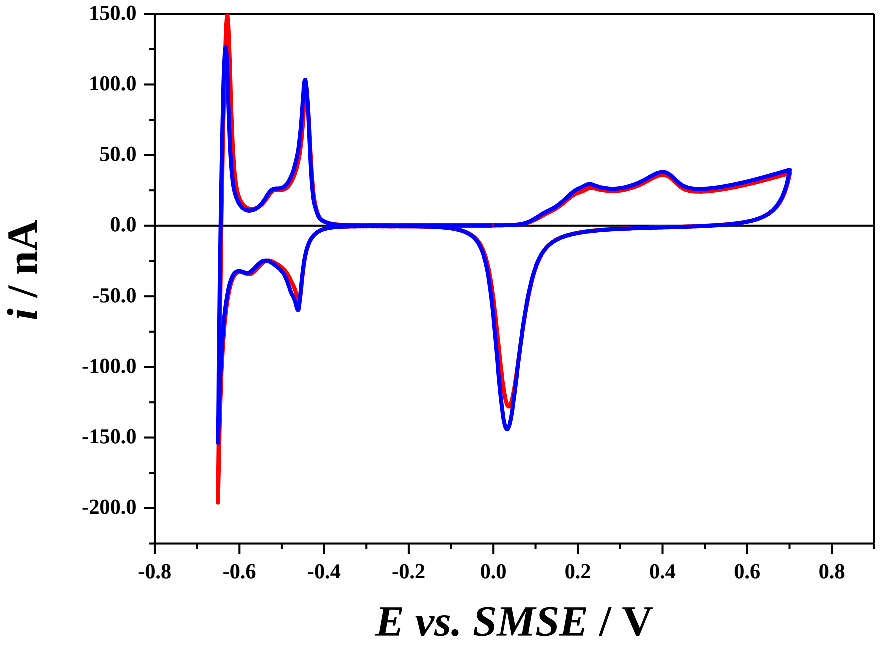

Figure 2.13 Cyclic voltammograms at ν=10 mV s^{-1} of H$_1$-e Pd films in 1 M H_2SO_4 in the potential window [-0.65; +0.70] V. Q_{dep} = 2 C cm^{-2}; q_{dep}= -10 µC. **Red**: potentiostatic mode, **blue**: galvanostatic mode.

The electrodes prepared as reported in this chapter were used intensively for the experiments reported in the chapters 3, 4 and 5. All the electrodes were prepared with the same chronoamperometric procedure with a deposition charge density of 1, 2, 4 or 10 C cm^{-2} depending the desired lifetime.

3. PdH microelectrodes as pH probes: the alkaline region and the role of oxygen.

3.1. Introduction to the PdH microelectrodes

Palladium hydride electrodes have long been used as reference electrodes[193, 194, 283] by using the constant potential of the α+β phase obtained in fixed pH conditions. The advantage of using the palladium hydride instead of the platinum hydrogen electrode is that there is no need to bubble gaseous hydrogen in the solution because the palladium hydride itself carries the hydrogen supply.

The palladium hydrogen electrodes have also been used widely as pH sensors[199, 204, 206, 284, 285] because the potential measured is dependent on the hydrogen ion activity in the solution. The advantages to employ palladium hydride electrodes as pH sensors are many: the potentiometric response is rapid, stable and reproducible. Imokawa *et al*.[206] reported an almost theoretical potentiometric response for those sensors with a *potential-pH* calibration curve, reproduced in **Figure 3.1**, with an almost Nernstian slope of -59.2 mV / pH at 25°C from pH 2 to pH 12.

It needs to be stressed that all Imokawa's measurements were carried out with nanostructured palladium hydride electrodes, with the palladium being electrodeposited on a platinum microelectrode. The linearity of the calibration curve over such a wide pH range is a rare characteristic for micro pH sensors. Furthermore, due to their nature, they can be used under extreme conditions of very high temperature or pressure[194], or in fluoride media[202].

Imokawa *et al*. joined together the use of the nanostructured palladium films with the pH sensing ability of palladium hydride. The use of the nanostructure ensured to maintain the geometry of the electrode at micrometre size; therefore the peculiarities of disc microelectrodes were maintained.

In this chapter, the fabrication of the hydride pH sensor will be presented with a particular enphasis on the calibration of this novel pH meter. The behaviour of the sensor will then be studied in presence of oxygenated and deoxygenated solution better to understand its limitations.

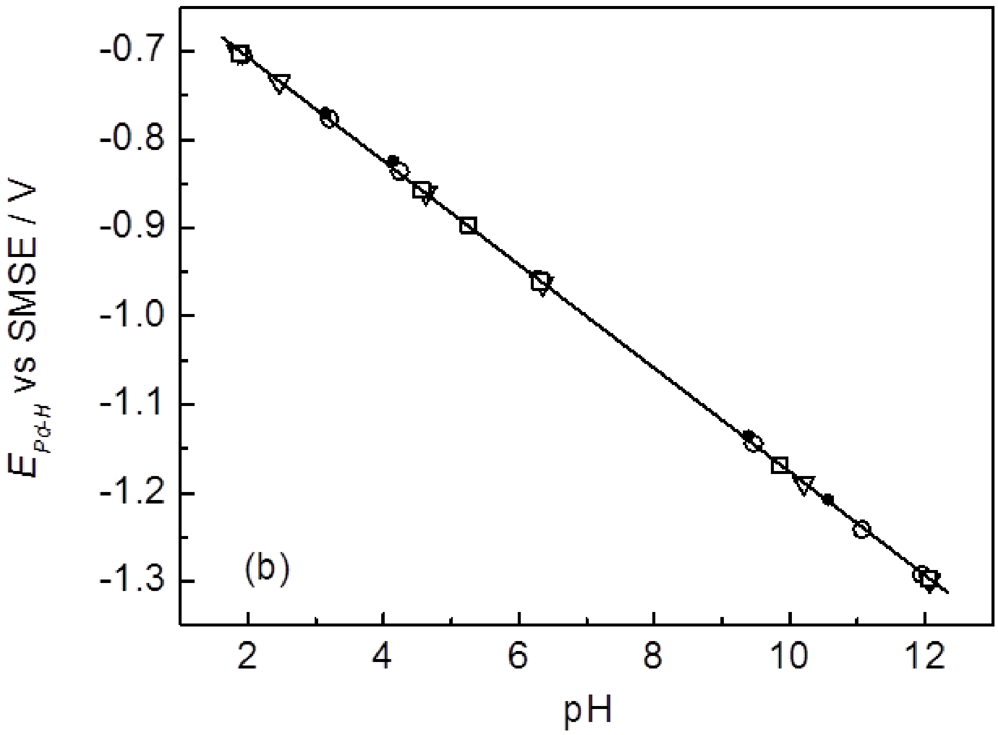

Figure 3.1 Calibration curve *E* $_{PdH}$ *vs. pH* taken from Imokawa *et al.*[206]. The data were obtained from the titration of a deaerated solution of 0.5 M Na_2SO_4 with H_2SO_4 and NaOH. The data at pH 7 were obtained by phosphate buffer.

3.2. How to obtain a PdH-pH probe?

Historically, palladium hydride electrodes were prepared by loading a palladium wire with hydrogen directly in the gas phase. This does not require a particular preparation of the palladium, it just needs to be clean enough and free from surface contaminants; usually this was achieved by dipping it in nitric acid. This ensures that a rapid equilibrium is established between the gaseous hydrogen and the hydrogen dissolved in the palladium.

In this section, two different approaches to load the catalyst with hydrogen are presented. The metal can be totally saturated with hydrogen in a short period (due to the nanostructure) by applying a cathodic polarization either at constant potential or current.

3.2.1. Potentiostatic loading

It needs to be stressed that in the potentiostatic loading, the potential is the driving force which controls the insertion of the hydrogen in the metal lattice and that the rate of absorption adapts itself according to the experimental conditions.

Potentiostatically driven hydrogen insertion is the most reported path to load different metals. Lukaszewski, Hubkowska, Grden and Czerwinski have published an extensive literature about this using Pd limited volume electrodes [180, 218, 228, 286-291]. LVEs offer the possibility to analyse different aspects of the hydride formation property such as the amount of absorbed hydrogen (*H/Pd*) as a function of the potential (E_L) applied to load the palladium. Normally, to estimate the amount of hydrogen absorbed as a function of E_L, the experimental procedure consists in the application of one potentiostatic jump between a potential where neither adsorption nor absorption exists (E_{DL}) and a potential located in the hydrogen absorption region (E_L). The chronoamperometric absorption of hydrogen can be coupled with voltammetric oxidative desorption in order to introduce the hydrogen at various potentials (E_L) and extract it at different sweep rates. The dependence of the measured amount of sorbed hydrogen as a function of E_L or scan rate, ν, can thus be estimated.

Potentiostatic loadings ensure that the hydrogen is loaded to a maximum *H/Pd* ratio before HER occurs on the surface. **Figure 3.2** shows chronoamperograms for H_1-e Pd electrodes with different amounts of catalyst recorded during the potential step between E_{DL} and E_L in a deaerated solution of 0.5 M Na_2SO_4 with 0.05 M H_2SO_4. E_{DL} and E_L were chosen after a voltammogram in the entire hydrogen region had been recorded. According to **Figure 1.7**, E_{DL} has been chosen in the region (I) and E_L in the region (IV). The cathodic current of the loading transients has a clear behaviour that is independent of the amount of palladium electrodeposited. As the potential switches from E_{DL} to E_L, a large current signal that rapidly decays to a first plateau (III) is recorded (**Figure 3.2**). It has been attributed to the start of hydrogen HS (I) and to the start of absorption in the α PdH (II), while (III) is due to the phase transition to reach a pure β PdH phase (IV), and the hydrogen evolution reaction (V) [285, 292].

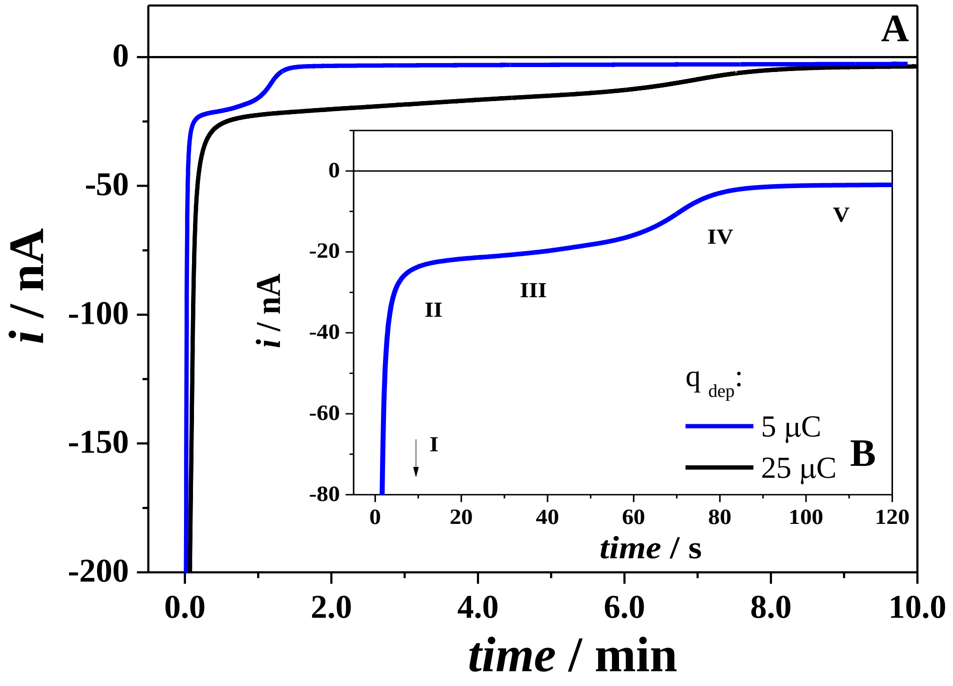

Figure 3.2 Potentiostatic loading. Chronoamperograms to load hydrogen into H_1-e Pd films with different amounts of catalyst. The experiment was carried out in a deaerated 0.5 M Na_2SO_4 + 0.05 M H_2SO_4 solution. The potential was stepped for 60 s in the double layer region (E_{DL} = -0.165 V *vs.* SMSE) and then to a potential in which the β PdH phase could be formed (E_L = -0.75 V *vs.* SMSE) until the second plateau was reached. **(A)** Comparison of the time needed to load different amounts of catalyst (**black**, q_{dep} = 25 μC and, **blue**, q_{dep} = 5 μC) and **(B)** definition of the five regions during the loading of hydrogen. The labels correspond to the start of hydrogen HS (I), the absorption in the α PdH (II) and the phase transition region (III) to reach a pure β PdH (IV) phase, and the hydrogen evolution (V) [285].

Clearly, the potential chosen for the loading influences the kind of processes taking place at the electrode surface, so the shape of chronoamperograms recorded differs for different E_L [211, 292]. If the potential chosen is too cathodic, the HER produces bubbles that can be trapped in the pores[191]. Another problem is that the choice of E_L depends on the pH of the solution: the more alkaline the solution, the more negative E_L has to be. This clearly is a problem when the sensor has to operate in unknown pH solutions.

3.2.2. Galvanostatic loading

In the galvanostatic loading, the hydrogen injection reactions are driven by applying a constant current at the electrode surface. The main advantage of this method over the potentiostatic loading is that it is possible to obtain a higher level of control in the generation of the hydride phases and in the mixed region between them. This approach is much more convenient than the potentiostatic loading because there is no need to know in advance the pH of the test solution. It is possible to load the electrode simply by going from zero current (OCP) to a negative current.

The galvanostatic intercalation of hydrogen in the metal lattice is less common than the potentiostatic one. In the galvanostatic transient technique a controlled and constant current - is imposed to the system and the potential adjusts itself to select different reactions capable of delivering the required rate.. The amount of hydrogen loaded, q_L, is simply estimated by the insertion current, i_L, and the time needed to reach a complete β PdH phase. Normally, to provide a complete saturation of hydrogen in the palladium, the experimental procedure consists in the application one galvanostatic jump between the zero current and a current located in the hydrogen absorption region (i_L).

An example of typical chronopotentiograms recorded during the loading of hydrogen in the nanostructured palladium films is shown in **Figure 3.3**. In the main picture a comparison of the potential transients under different galvanostatic conditions for the loading is presented. The cathodic potential of the loading transients has a clear behaviour that is independent of the current, i_L, applied. Only the transition time, Δt in region (III), depends on the current chosen as the time is inversely proportional with respect to the current needed for the hydrogen loading. As the current switches from 0 to i_L, the electrode potential rapidly moves to more cathodic values until a stable plateau (V) is recorded. The features in the chronopotentiogram have been attributed to the start of hydrogen HS (I) and to the absorption in the α PdH phase (II), while (III) is the constant potential due to the phase transition region to reach a pure β PdH (IV) phase, and the hydrogen evolution reaction (V) [285, 292]. By multiplying the loading time with the loading current, the potential drift can also be plotted against the loading charge used to insert the hydrogen **Figure 3.3.B**.

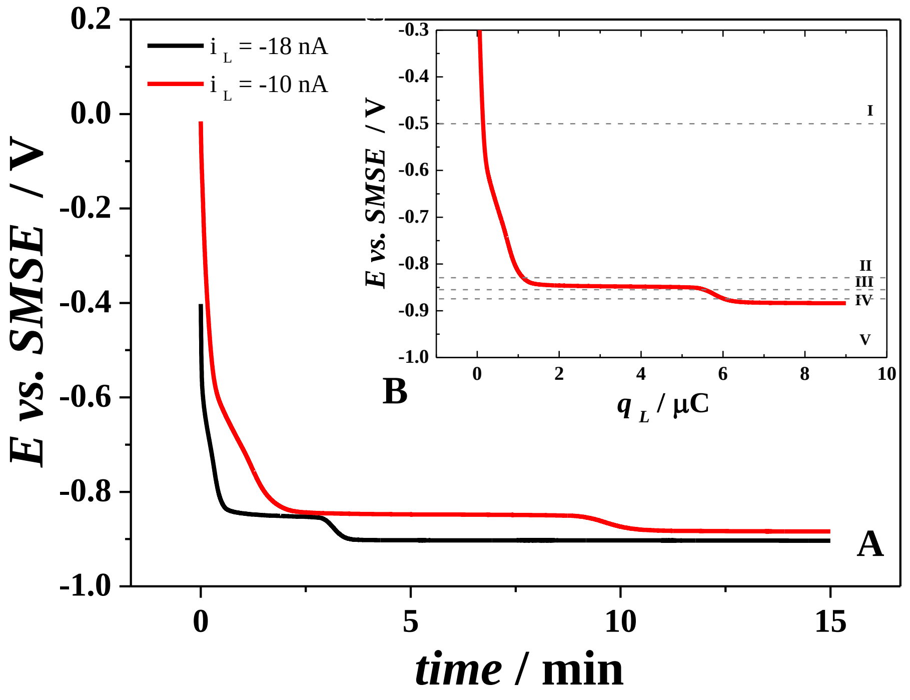

Figure 3.3. Galvanostatic loading. Typical chronopotentiograms recorded during the loading of hydrogen into a H_1-e Pd film ($2a$ = 25 μm, Q_{dep} = 10 C cm^{-2}) in a solution of 0.5 M Na_2SO_4 at pH ~ 4. **(A)** Comparison of different loading currents (**black**, i_L = -18 nA and, **red**, i_L = -10 nA) and **(B)** chronopotentiogram for i_L = -10 nA plotted against the hydrogen loading charge, q_L. There are five clear regions which correspond to (I) the double layer zone and the start of hydrogen HS, (II) the absorption in the α PdH, (III) the phase transition region to reach (IV) a pure β PdH phase, and the (V) hydrogen evolution [292]

The steady current applied at the electrode forces the reduction of the protons in the solution to occur at a constant rate via the Volmer reaction (19). The potential of the electrode moves then to more cathodic values with time as the hydrogen is absorbed increasing the *H/Pd* ratio in the α PdH phase. The first plateau is reached as soon as the β phase begins to coexist with the α phase and it ends with the completion of the β PdH phase. According to Williams [292], the last reduction potential plateau is due to the Heyrovsky (20) or the Tafel (21) reactions associated with the HER. One should note that the phase transition plateau (III) is at the same potential when the insertion of hydrogen is done by applying different currents. The equilibrium potential between the two hydride phases is in fact dependent only on the activity of protons in the solution. Besides, the α → β transition plateau (III) is at 150 mV more lower potential than that for the extraction of hydrogen, β → α, at OCP conditions. This phenomenon is usually known as hysteresis[293]. Also in the case of galvanostatic loading, as previously mentioned, a good practice is not to maintain the polarization after the completion of the β PdH phase because of the production of hydrogen bubbles. The Ohmic polarization due to changes in concentration of the electrolyte along the main axis within the pores has never been considered on H_1-e Pd.

3.3. How does the PdH-pH probe work?

The beauty of palladium hydride electrodes is that they behave as pH sensors. At standard temperature, the palladium-hydrogen phase diagram consists, in the hydrogen poor α PdH phase ($H/Pd < 0.02$), the intermediate region where the α and β coexist ($0.02<H/Pd<0.6$) and the hydrogen containing rich β PdH phase ($H/Pd > 0.6$). When the hydrogen is increased to the limit of the miscibility gap, the system has only one degree of freedom by virtue of the Gibb's phase rule, which fixes the hydrogen content and therefore the hydrogen activity of the α phase. In the two phase region, the equilibrium imposes that the activity of hydrogen in the α phase must be equal to the activity of hydrogen in the β phase. This constant hydrogen activity in the metal provides a wide ranging and stable activity against which the hydrogen ion activity in solution can be reliably measured. The pH response can be derived from the Nernst equation (29):

$$E_{PdH} = E^0_{PdH} - \frac{RT}{nF}\, pH \tag{29}$$

where E_{PdH} is the potential of the electrode, E^0_{PdH} is the standard potential, R is the gas constant, T is the temperature and F is the Faraday constant [193].

Typical potential transients during the spontaneous discharge of the sensor at OCP are reported in **Figure 3.4**. The measurements were performed at different pH, and this is reflected by the differences in the nominal value of the potential plateau at the phase transitions. **Figure 3.4.left** shows a typical potentiometric response, *red*, and its first order derivate, *blue*. The two curves were compared to estimate the two characteristic times t_1 and t_2, whose difference determines the life time of the pH sensor. Imokawa *et al.* [206] reported that the lifetime is roughly proportional to the geometrical features of the film. In **Figure 3.4.right** the features are labelled. The rising potential before reaching the plateau correspond to the β phase [$t < t_1$] so the time t_1 can be related to the $H^{\beta\rightarrow\alpha}$/Pd ratio quoted in the literature [180, 191, 206, 211, 213, 217, 219, 226, 227, 294]. The stable potential [$t_1 < t < t_2$] denotes the period of time in which the progressive transition from β to α phase is taking place. During this time the two phases are in equilibrium and the value of this potential is related to the pH of the solution. After the plateau [t > t_2] the potential rises again. This event is due to the progressive loss of hydrogen when the hydride is entirely in the α phase. In addition, **Figure 3.4.right** shows a comparison of the potential transients recorded after the palladium had been loaded by chronoamperometry (blue) and chronopotentiometry (red), in both the cases, the potentials agree within the experimental error. In this study the equilibrium potential is estimated considering the potentials at the life time limits, $E(t_i)$, and taking the average. The error for the potential transient is estimated as the half difference of the two potentials at the life time limits ($err = \frac{|E_{t1} - E_{t2}|}{2}$).

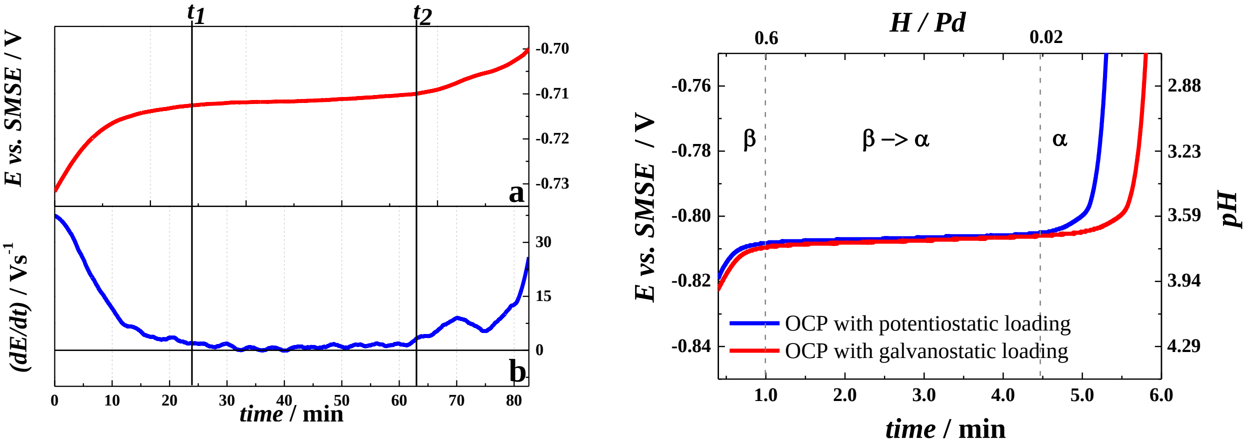

Figure 3.4 (left) (a) Potential transient recorded at OCP with an H_1-e Pd film (Brij® 56) deposited (Q_{dep} = 1 Ccm^{-2}) on a 25 µm diameter Pt electrode. The experiment was carried out in a deaerated 0.5 M Na_2SO_4 + 0.05 M H_2SO_4 solution immediately after hydrogen was loaded at E_L = -0.75 V at pH = 2. **(b)** First order derivative of the potential transient to measure the pH sensor lifetime defined by the vertical lines t_1 and t_2, t_{life} = 39 mins. **(right)** Comparison of potential transients recorded with a H_1-e Pd film (2a = 25 µm, Q_{dep} = 10 C cm^{-2}) in 0.5 M Na_2SO_4 at pH ~ 3.7 in an open cell after the catalyst has been loaded potentiostatically, **blue**, and galvanostatically, **red**. The identification of the phases and the *H/Pd* ratio are in accordance with models [227] and isotherms in acidic solutions [180, 191, 206, 211, 213, 217, 219, 294].

The H/Pd values in **Figure 3.4.right** were assumed taking in consideration the beginning and the end of the transition region, but they can be estimated by the atomic ratio as calculated as follow:

$$\frac{H}{Pd} = \frac{m_H}{m_{Pd}} = \frac{q_H}{q_{Pd}}\frac{n_{Pd}}{n_H} = 2\,\frac{q_H}{q_{Pd}} \qquad (30)$$

were *m* are the number of moles, *q* is the charge, *n* is the number of electrons. In particular, q_H is the charge produced by the extraction of the inserted hydrogen by LSV between the OCP of the system and -0.1 V *vs.* SMSE (at pH = 7) and q_{Pd} is the charge of the electrodeposited palladium.

3.4. The Nernstian behaviour of the phase transition in alkaline pH

From the practical point of view, the excellent reproducibility of the plateau potentials between electrodes with different size and thicknesses[206] allows to estimate the correct value of proton activity in solution (and interfaces) of an unknown pH upon comparison with the calibration curve. From previous preliminary studies [285], the nanostructured hydride sensors have shown an almost Nernstian linear behaviour also for solution at pH > 12, where usually the glass pH electrode fails.

In this project, the potentiometric pH response of H_1-e Pd hydride microelectrodes was studied in extreme alkaline conditions with the purpose to use the sensors in $Ca(OH)_2$ solutions. Different approaches were followed. The potential transients were recorded (i) in homemade buffers, (ii) during the neutralization of 1 M NaOH and (iii) during the titration of a solution containing 1 M NaOH and 50 mM Na_3PO_4.

For each plateau recorded during the experiments (i-iii), E_{PdH} was estimated and plotted as a function of pH, as shown in **Figure 3.5**. The plot was built using a combination of data by measurements carried out in buffers (i) neutralizations and titrations (ii and iii). Eight different H_1-e Pd sensors were used for these experiments. The linear trend of the data is in agreement with the previous study done for pH < 12. The calibration curve E_{PdH} *vs.* SMSE as a function of pH can be fitted with the following equation:

$$E_{PdH} = (-567 \pm 5)\ mV + (-58.7\ \pm 0.5) mV\ pH \tag{31}$$

The parameters estimated after these measurements are close to the theoretical values in the Nernst equation referred to the palladium hydride system. **Table** 3.1 compares the parameters obtained, their maximum and minimum values with respect to the theoretical parameters. To our knowledge, this is the first observation of a microelectrode reliably measuring pH to such alkaline conditions.

Table 3.1 Comparison between the theoretical and the estimated parameters in the Pd hydride calibration curve .

	Parameters	$E_{Theoretical}$ vs. *SMSE* / mV	$E_{Experimental}$ vs. *SMSE* / mV
Intercept	E^{o}_{PdH}	-589	-567 ± 5
Slope	$\frac{2.303\,RT}{F}$	-59.2	-58.7 ± 0.5

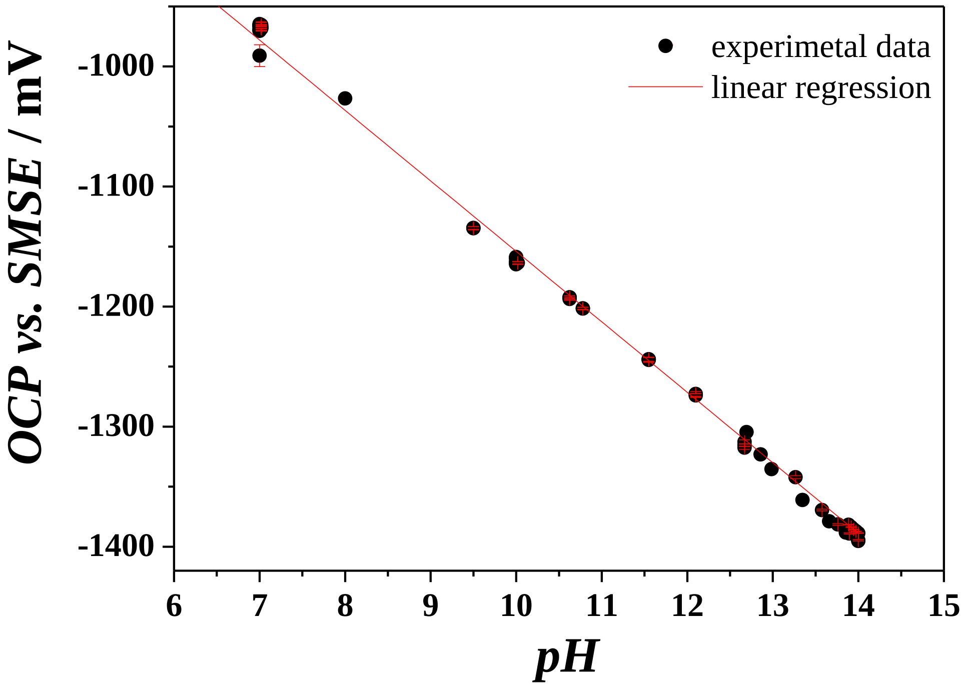

Figure 3.5 Calibration curve E_{PdH} *vs. pH vs.* SMSE at 25°C obtained from potential transient measurements in homemade phosphate buffers (measured pH), forward neutralization in 1 M NaOH and forward titration in 1 M NaOH with 50 mM Na_3PO_4 (calculated pH). The **red line** draws the equation (39) of the linear regression of these data points. The error is estimated as $\frac{|E_{t1}-E_{t2}|}{2}$ only for the data acquired in buffers.

3.5.The identification of the processes upon cyclic voltammograms

Previously, in paragraph 2.7.2, the voltammetry of H_1-e Pd has been considered in 1 M H_2SO_4. In this section the main features of voltammograms in solution containing dissolved salt at more alkaline pH are observed and analysed in order to (i) assign processes to different potentials, (ii) support the understanding of the peaks in cyclic voltammetry and linear sweep voltammetry and (iii) support the understanding of the potential plateaus in chronopotentiometry.

The experimental data presented in this section were recorded in a solution of 0.5 M Na_2SO_4 adjusted to pH 4 by addition of 5×10^{-5} M H_2SO_4. The experiments were carried out in divided cells with the WE and CE (platinum ring or grid) in one compartment containing the analyte solution, and a homemade reference electrode SMSE (703 mV *vs.* SHE) in the second compartment. The two cells were divided by a homemade agar salt bridge obtained with a saturated solution of K_2SO_4 + 1% of Agar. This was adding 3 mV to the potential of the SMSE *vs.* SHE. All the experiments were done at room temperature without any thermostatic control.

In order to understand the processes taking place, preliminary tests were carried out at high and slow scan rates and in presence/absence of crystal violet; voltammograms were also recorded at different cathodic limits in the absence of air to avoid any signal from the ORR. The peaks are labelled as they appear in the voltammogram, clockwise, starting from peak 1 at -0.58 V. The different peaks that have been identified on the basis of **Figure 3.6** and **Figure 3.7 A** and **B** are listed with their characteristic features in **Table 3.2**.

Table 3.2 Analysis of the peaks labelled in **Figure 3.6** and **Figure 3.7**.

Peak	Process	Observations	Conclusion
1	cathodic	• the peak potential remains constant by varying the negative limit, • it disappears in presence of crystal violet.	surface process
2	cathodic	• it appears for E < -0.9 V, • the peak potential remains constant by varying the negative limit, • it does not disappear in presence of crystal violet.	bulk process
3	cathodic	• it appears for E < -1.2 V, • the peak potential varies with the scan rate, • the crystal violet shifts the peak potential to more anodic values	bulk process

4	anodic	- it does not disappear in presence of crystal violet - it appears when the lower potential limit is -1.2<E<-0.9 - the peak potential remains constant by varying the negative limit, - the area under the peak is decreasing when the potential limit gets more anodic	bulk process
5	anodic	- the peak looks asymmetric, due to the presence of the peak 4, - it appears when the lower potential limit is E<-1.2, - the peak potential is shifted to more cathodic values in presence of crystal violet, - the area under the peak remains the same in presence of different amounts of crystal violet.	Bulk process
6	anodic	- it disappears in presence of crystal violet, - the peak potential remains constant by varying the cathodic limit except when bulk processes do not happen. In this case the peak potential gets more anodic.	surface process
7	anodic	- the peak potential remains constant by varying the negative limit, - it disappears in presence of crystal violet.	surface process

Furthermore, the peak separation between 5 and 3 is decreasing with increasing concentration of crystal violet and therefore the process looks more reversible. According with the observations listed in **Table 3.2**, the processes can be identified ad linked between them as: (1) adsorption/(6) and (7) desorption, (2) absorption/(4) corresponding extraction, (3) absorption/(5) corresponding extraction. From this interpretation, the extraction 4 happens at more cathodic potentials than the 5. This might be due to a more reversible process that leads to a smaller peak separation. Less clear is the role of two desorption peaks when only one adsorption process has been observed.

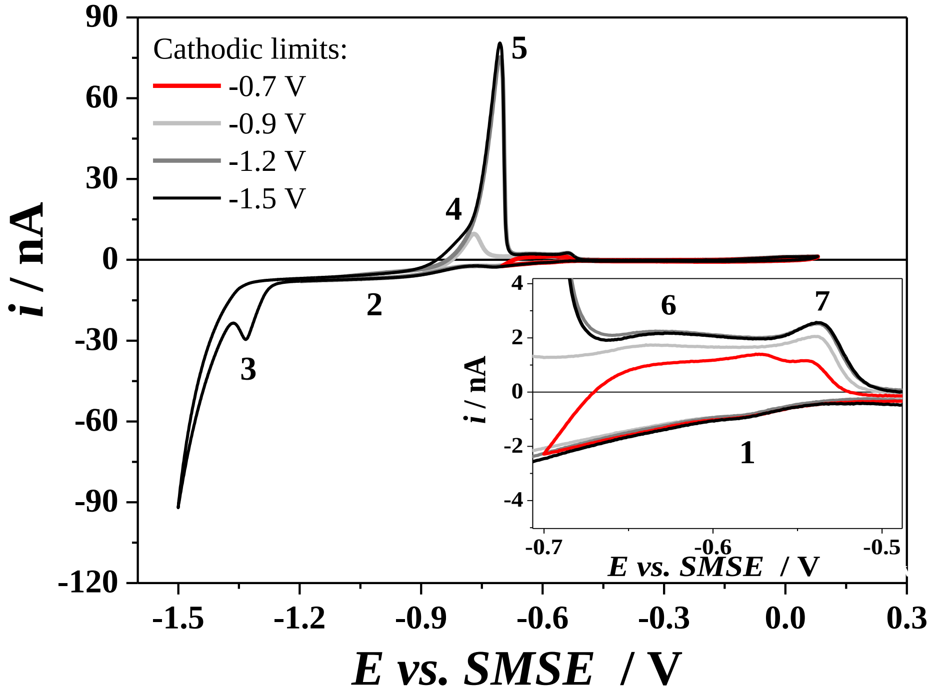

Figure 3.6 Cyclic voltammograms for an H_1-e Pd film (Q_{dep} = 10 C cm^{-2}, *RG* = 4.26) deposited on a platinum disc electrode (2*a* = 10 μm) recorded in a deaerated 5×10^{-5} M H_2SO_4 + 0.5 M Na_2SO_4 solution at a scan rate of ν = 2 mV s^{-1}. The cathodic potential was changed to identify the processes occurring in the hydrogen region. In the inset, the region with the peaks 1, 6 and 7 is enlarged.

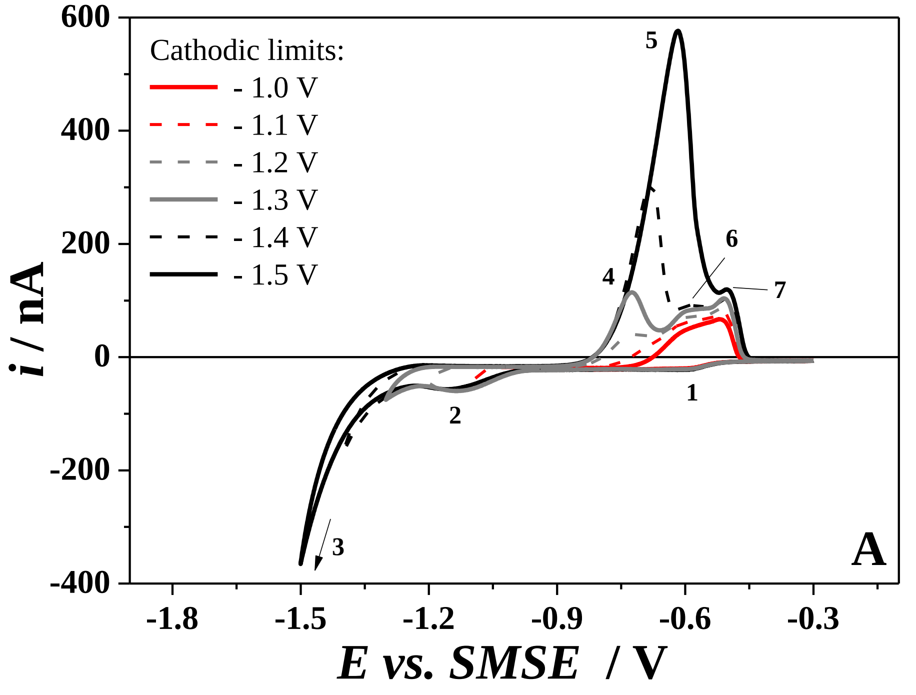

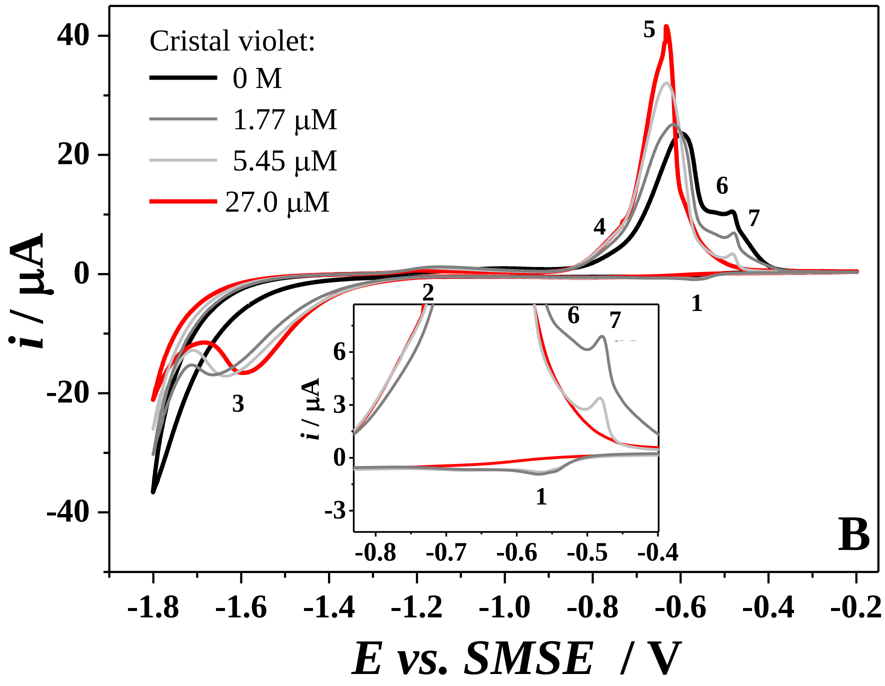

Figure 3.7 Cyclic voltammograms for an H_1-e Pd film (Q_{dep} = 10 C cm^{-2}) deposited on a platinum disc electrode (A : 2*a* = 10 µm, *RG* = 3.83 and B: 2*a* = 250 µm) recorded in a deaerated solution of 5×10^{-5} M H_2SO_4 + 0.5 M Na_2SO_4 at a scan rate of ν = 50 mV s^{-1}. The voltammograms were recorded in order to discriminate the hydrogen processes occurring at the surface and in the bulk by **(A)** the change of the cathodic potential and **(B)** the addition of increasing amounts of crystal violet in the solution. During every addition the solution was bubbled with argon to guarantee its homogenization and to remove possible air which could have diffused during the stabilisation of the voltammograms.

In accordance with these considerations, it is possible to attribute the peaks in the hydrogen region to the hydrogen adsorption (a) and desorption (f and g), the start of hydrogen absorption in the α (b) and β (c) PdH phases, the hydrogen evolution reaction (d) and the extraction of hydrogen from the hydride (e). These are clearly identifies in **Figure 3.8**.

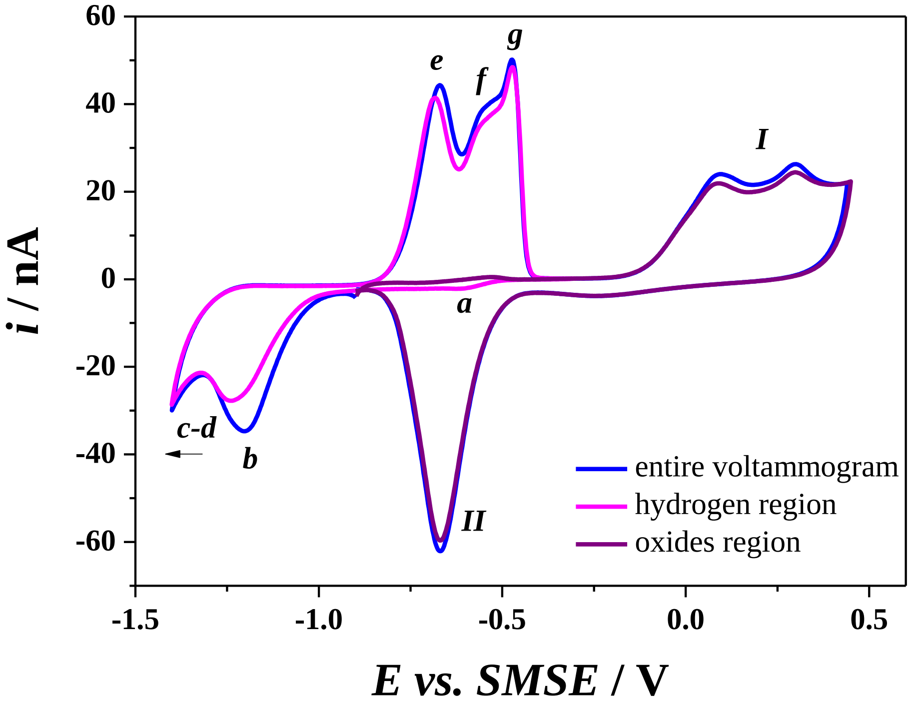

Figure 3.8 Cyclic voltammogram for an H_1-e Pd film (Q_{dep} = 2 C cm^{-2}, *RG* = 3.25) deposited on a platinum disc electrode (2*a* = 25 μm) recorded in argon purged 5×10^{-5} M H_2SO_4 + 0.5 M Na_2SO_4 solution at 50 mV s^{-1}**.** The peaks in the hydrogen region correspond to (a, f-g) the hydrogen adsorption/desorption, (b) the start of absorption in the α PdH and (c) β PdH, (d) the hydrogen evolution reaction and (e) hydrogen extraction from the hydride. In the oxides region, the labels corresponds to (I) the formation of the palladium oxides and (II) their reduction.

3.6.The effect of oxygen in the pH sensing

The introduction of oxygen into the solution causes a negative shift in the current of the voltammograms below -0.3 V, and a clear limiting current was observed, see **Figure 3.9**. The limiting current obtained for an oxygen saturated solution, -68.91 nA, approximately 4.5 times larger than that obtained for an air saturated solution, -15.07 nA, in good agreement with the oxygen level in air.

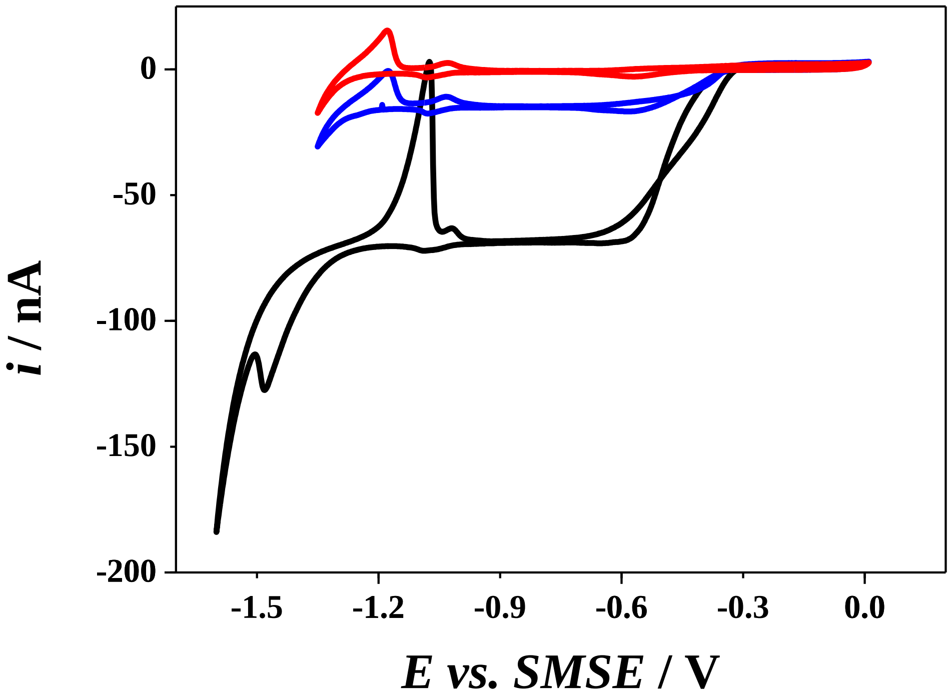

Figure 3.9 Voltammograms recorded with a 25 µm H_1-e Pd electrode (Q_{dep} = 2 C cm^{-2}) at 1 mV s^{-1} and 25±0.5 °C in a 20 mM phosphate buffer, pH 12.6, I_s= 200 mM in different gaseous environments; argon (**red**), air (**blue**) and oxygen (**black**).

The limiting current was plotted *vs*. the pH (not shown) to determine whether any dependence existed between the two and to see whether the ratio of limiting currents between air and oxygen saturation remained constant across the pH scale. In air saturated solution, the limiting current is approximately -16 nA and the limiting current in oxygen saturated solution is -60 nA. This results in the limiting current of the ORR in presence of oxygen being approximately four times that recorded in air. The plot also demonstrates there is not definite trend and the limiting current did not seem to depend on pH.

3.6.1. Effect of oxygen during the galvanostatic loading

Galvanostatic loading was carried out in absence and presence of oxygen. It was noticed that the time taken to load hydrogen into the palladium to achieve the complete β phase was much longer in the presence of oxygen than in argon, see **Figure 3.10**. As the same current used to load in the different gaseous environments it was believed that the loading time was longer in presence of oxygen due to a proportion of the current being used to carry out the ORR. This results in the current needing to be passed for a longer period of time to ensure the same level of loading as in the presence of air and argon is achieved. As the ORR occurs to a lesser extent in the presence of air, and should not be carried out at all in the presence of argon, the loading time was observed to be shorter in presence of air and the shortest in argon.

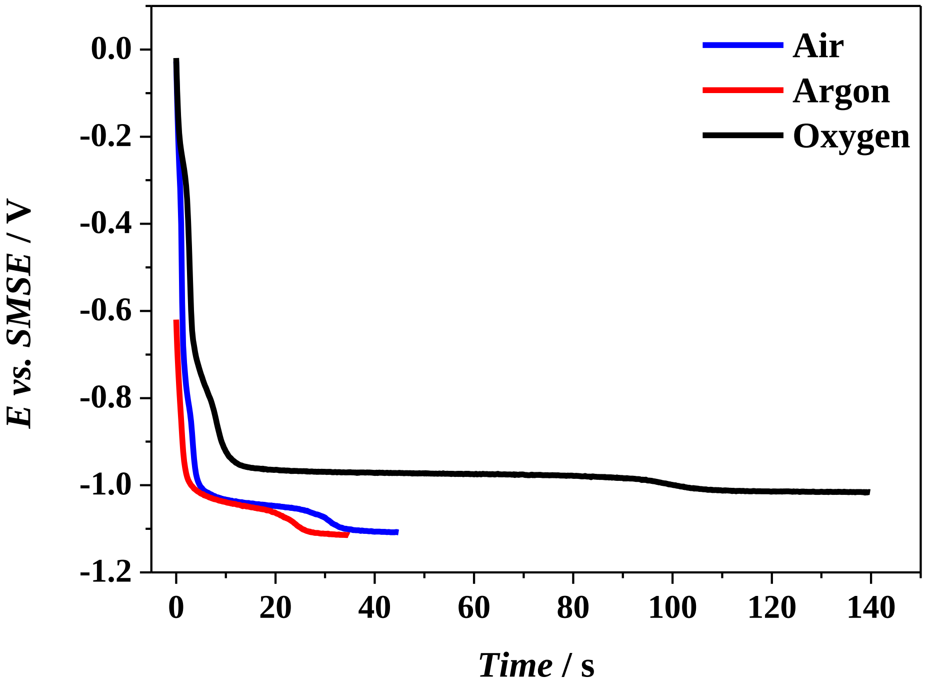

Figure 3.10 Galvanostatic hydrogen loading of H_{1-e} Pd 25 µm electrode at -80 nA *vs.* SMSE with a Pt grid as the CE in PB 200 mM, I_s=200 mM, pH = 3.0 at 25 ± 0.5 °C. Loading in presence of oxygen (**black**), air (**blue**) and argon (**red**).

3.6.2. Effect of oxygen on OCP measurements

Chronopotentiometric measurements, **Figure 3.11**, demonstrate that the lifetime of the sensor in the presence of oxygen was much shorter than in presence of air or argon. If we assume that the rate of extraction was driven solely by the ORR, then according to the limiting current of the ORR recorded on the voltammograms, we would expect to see the lifetime of the sensor in air to be approximately four times longer than that in oxygen.

From the OCP transient, **Figure 3.11**, it can be seen that the lifetime of the sensor in air is much greater than four times that in oxygen thus it can be said that the lifetime is governed by more than the rate of the ORR. It is thought that the extraction of the hydrogen from the nanostructured pores, which controls the lifetime, is dependent on two reactions: the electrochemical reduction of oxygen, balanced by the hydrogen extraction via electron transfer through the surface of the metal, and the direct chemical reaction of oxygen and hydrogen on the surface of the electrode. The very short lifetime observed with oxygen suggests that the chemical reaction occurs at a much faster rate with oxygen saturation than with air saturation.

It is also interesting to consider why the hydrogen loaded in presence of argon extracts at all as the proposed methods of extraction should not occur in an inert atmosphere. It is possible that the extraction is caused by a small amount of oxygen present in the solution, which is allowing for these reactions to occur. As the oxygen is in very low concentration the lifetime of the sensor is much greater than the lifetime in air or oxygen as these reactions are unable to proceed at a significant rate.

It is also likely that as there is equilibrium between the hydrogen in the lattice and the H_2 in the solution, when the molecular hydrogen diffuses away from the interface, then the hydrogen is extracted from the metal. This process will be occurring in all three gaseous environments, as it does not depend on the presence of oxygen.

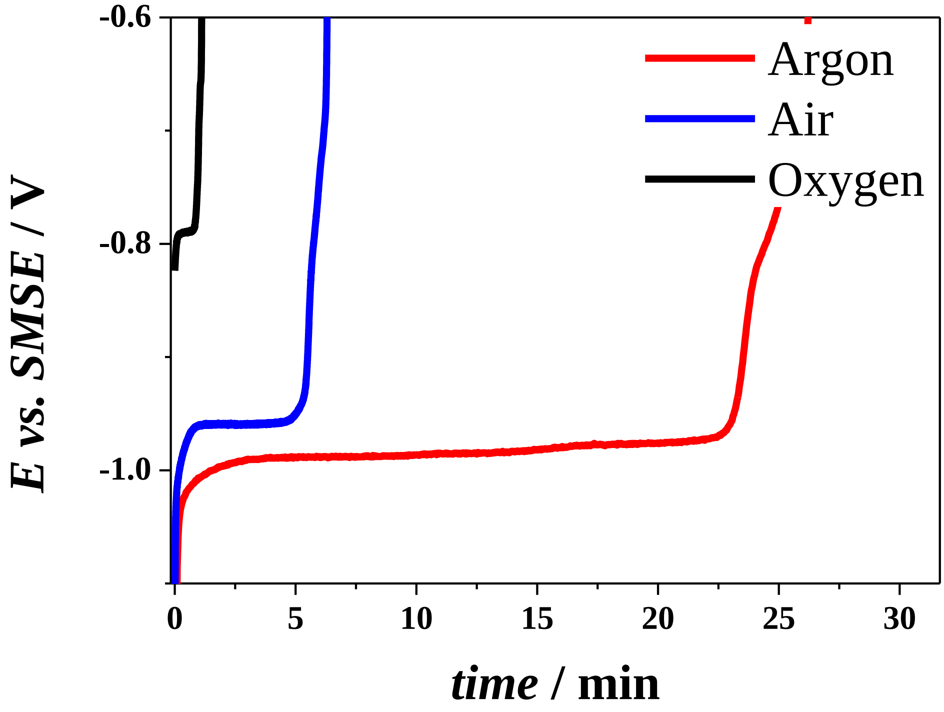

Figure 3.11 Chronopotentiograms recorded at open circuit and 25 ± 0.5 °C with a 25 µm diameter H_{1-e} Pd electrode (Q_{dep} = 2 C cm^{-2}) in PB 200 mM, I_s = 200 mM, pH = 7.0 at 25 ± 0.5 °C in presence of argon (**red**), air (**blue**) and oxygen (**black**).

For each pH, the potential of the α-β transition plateau from the chronopotentiograms was recorded in presence of argon, air and oxygen. The open circuit measurements were repeated six times in air and oxygen and three times in argon due to time constraints. Having determined the potentials at t_1 and t_2 an average potential for the plateau region was determined, $\bar{E}$. The average of the results obtained from the repeated experiments was then determined to provide an average $\bar{E}$ for each pH; the values obtained for $\bar{E}$ in the different gaseous environments were plotted against the pH of the solution to produce the corresponding calibration curves, see **Figure 3.12**.

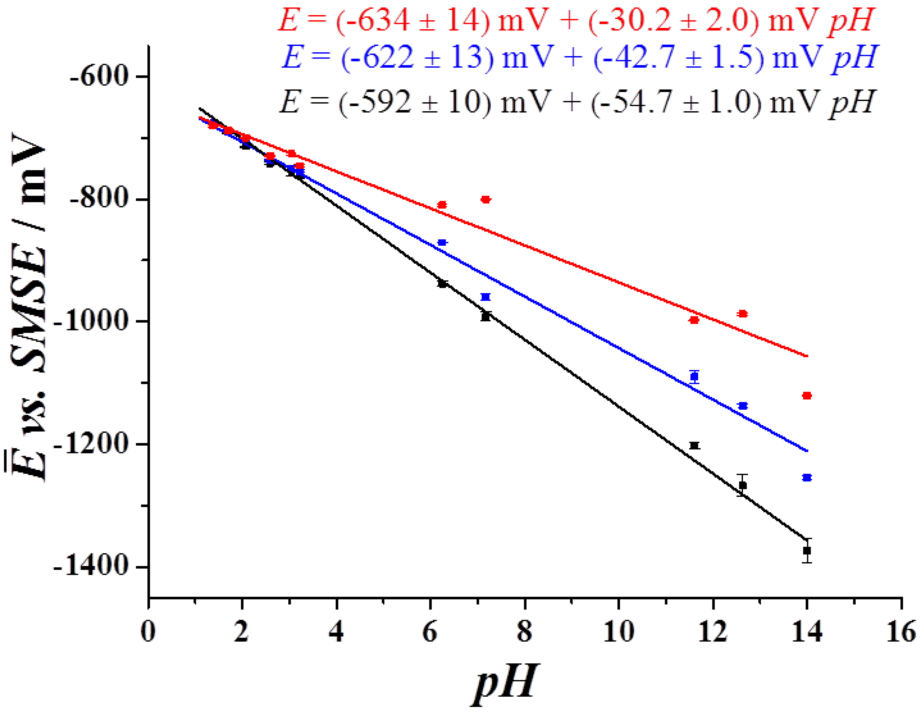

Figure 3.12 Calibration curve E_{PdH} *vs.* *pH* *vs.* SMSE at 25°C obtained from open circuit potential transients in homemade phosphate buffers at 25 ± 0.5 °C. Argon (**black**), air (**blue**) and oxygen (**red**) with the associated trend lines and errors.

The calibration plots, **Figure 3.12**, show that the linear relationship between the potential and the pH is maintained even in presence of air and oxygen in the solution, but the reproducibility (larger error bars) of the results is getting worse the more oxygen is in the solution. Furthermore, the slopes in presence of air and oxygen show a sub Nernstian response, this will be investigated in chapter 4.

In the acidic region of the plot, below pH 6.2, the data is thought to be less reliable as there were fluctuations in the temperature due to problems with the thermostatic bath. As the Nernst equation is temperature dependent these fluctuations caused the potentials measured to be less reliable. The recordings for this acidic range were not repeated as the focus of this research was the neutral and alkaline region of the pH scale in order to use the sensor in presence of saturated solution of $Ca(OH)_2$.

The experiments carried out in argon, **Figure 3.12**, demonstrate the excellent reproducibility of the H_{1-e}Pd electrodes and, as in previous studies[206, 285], the almost linear Nernstian response of the pH-electrode.

In presence of air and oxygen the intercept of the trend line is shifted to a more negative potential than that seen for argon. Furthermore for pH > 1.5 the presence of oxygen creates a positive shift, but for pH < 1.5 the presence of O_2 leads to a negative shift.

It has been found that the electrode behaves very differently in presence of oxygen. The data collected demonstrates that the presence of oxygen significantly changes the behaviour of the sensor and that the behaviour of the palladium hydride system in oxygen is far from being understood. The complexity of the system and the poor reliability of the data collected in oxygen at this stage provide little practical use.

For each point on the calibration plot the error associated with the potential was calculated using two different methods: first, the error was calculated by finding the standard deviation of the average potential for the plateau for each repeat of the experiment, second, the error was calculated using the difference in potential between t_1 and t_2 (ΔE) determined for each repeat, the average ΔE value was found and divided by two. The standard deviation method provided the error associated with the different repeats. In many cases the error was found to be an order of magnitude smaller than that one measured as $\frac{|E_{t1}-E_{t2}|}{2}$. The error calculated using ΔE provided a more realistic overview of the error associated with the measurements as it calculated the error associated with the plateau. The errors obtained using this method are shown in the calibration plot.

It can be seen that some of the errors associated with measurements taken in argon are quite large. It was thought that this is due to the increased lifetime seen in presence of argon, as over this extended lifetime oxygen may slowly enter the system. Furthermore, the error bars are not very large compared with the reproducibility of the data, whatever the gas. The error estimation is therefore not able to account for the unreliable behaviour of the palladium hydride in presence of dissolved oxygen.

3.7. The driving factor

From the data presented above, it looks clear that oxygen is playing an important role and its interaction with the palladium hydride needs to be considered, analysed and quantified.

A series of stripping experiments were carried out in order to quantify the process of hydrogen extraction in presence of dissolved oxygen. The procedure consisted in (i) galvanostatically loading the nanostructured palladium to fully charge the metal with hydrogen, (ii) leaving the electrode at open circuit potential for a set time to allow the “natural discharge” of hydrogen from the PdH, (iii) switching to the potentiostatic mode and recording a linear sweep voltammogram to completely extract the hydrogen from the Pd lattice and (iv) integrating the area under the stripping peak to quantify the amount of hydrogen left in the hydride. **Figure 3.13** shows the recorded stripping peaks for different waiting times. The durations for which the sensor was left to discharge naturally are written on the figure. It is possible to see that the area under the peak decreases with increasing discharge duration and it is possible to observe from **Figure 3.14** that the corresponding charge decreases linearly with the discharge duration. The slope of this linear relationship is a current, approximately -14 nA, which is analogous to the extraction current of the hydrogen from the metal lattice.

As previously mentioned, oxygen looks to be a substantial component that is driving the reaction because in presence of oxygen (as air or pure oxygen) the lifetime of the sensor is decreasing and the loading time is increasing massively. In order to quantify the rate of oxygen reduced at the tip at the same time in which the extraction was occurring, a LSV of the ORR was acquired, **Figure 3.15**.

The ORR limiting current observed has almost the same value (between 13 and 14 nA) as the slope of **Figure 3.14**. As previously mentioned, this slope is thought to be the extraction current of the hydrogen from the palladium hydride lattice. It can therefore be concluded that the hydrogen extraction current is driven by the diffusion controlled reduction of oxygen on the nanostructured Pd surface.

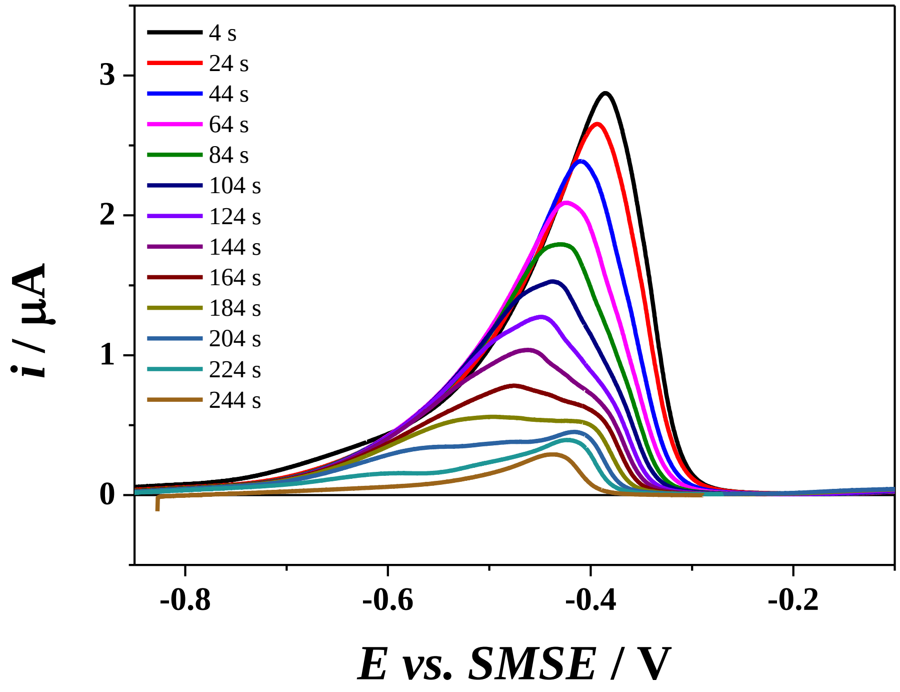

Figure 3.13 Linear seweeps voltammograms for the extraction of hydrogen from the PdH recorded after galvanostatically loading hydrogen and leaving the electrode at open circuit for the times indicated in the legend. The experiments were carried out in aerated 20 mM PB I_s = 200 mM pH = 7 at room temperature and with a H_1-e Pd electrode (2a = 25 µm and Q_{dep} = 4 C cm^{-2}).

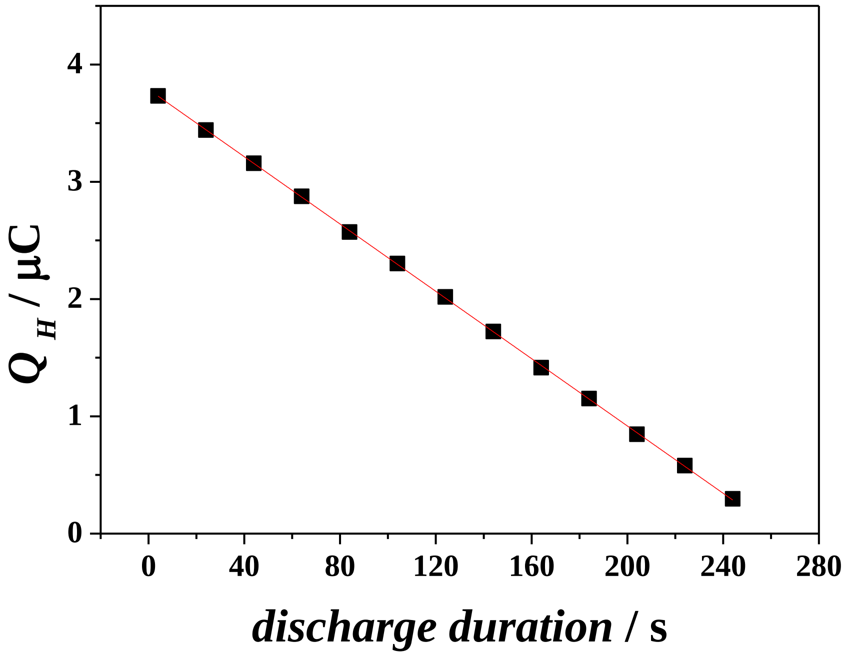

Figure 3.14 Plot of the hydrogen extraction charges recorded after allowing the PdH to discharge at open circuit for different discharge durations along the β to α transition plateau. The extraction charges were calculated from the stripping voltammograms shown in **Figure 3.13**.

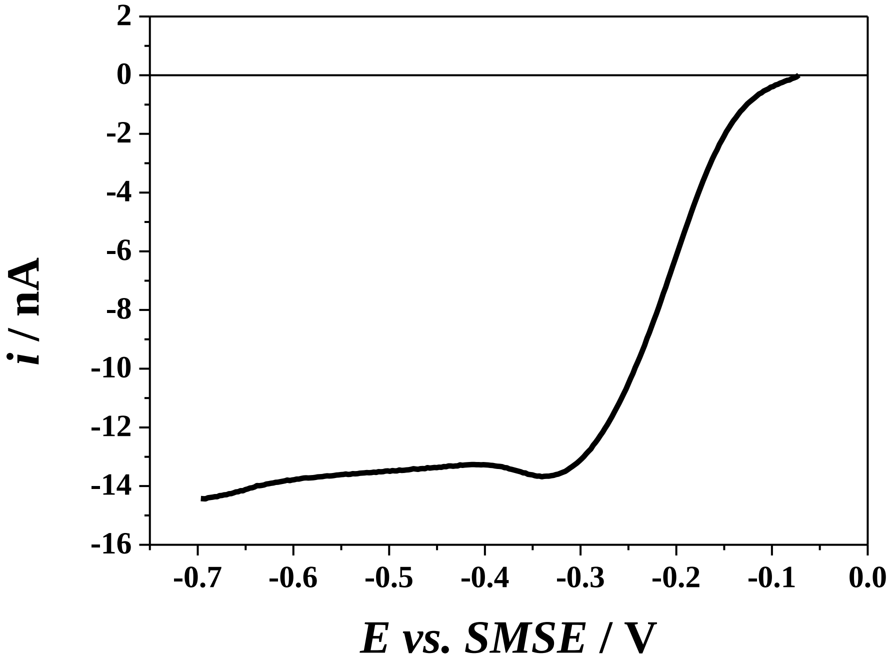

Figure 3.15 Linear sweep voltammogram recorded with a H_1-e Pd electrode (2a = 25 µm and Q_{dep} = 4 C cm^{-2}) in aerated 20 mM PB I_s = 200 mM pH = 7 solution at 1 mV s^{-1}. The LSV was started at OCP.

The same procedure was used to estimate the extraction current in absence of any oxidant (i.e. with the solution previously degassed for 20 minutes with argon and left covered with an argon blanket to prevent any uptake of oxygen). As for **Figure 3.13**, the charge under the stripping peaks recorded for different waiting times was found to decrease with increasing discharge durations. As in **Figure 3.14**, the plot of the hydrogen stripping charge *vs.* discharge time, shows a linear trend (Figure **3.16**) but the slope, or hydrogen extraction current, is only -319 pA. It is therefore concluded that in absence of any oxidant, the rate of hydrogen extraction is extremely slow and this dictates the longer lifetime of the palladium-hydrogen electrode.

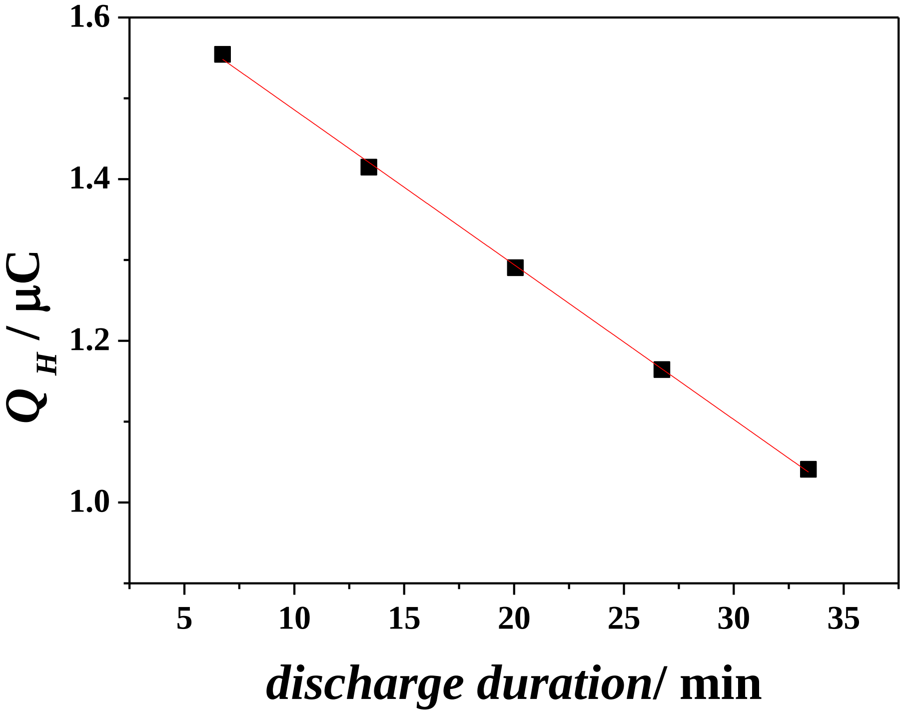

Figure 3.16 Plot of the hydrogen extraction charges recorded after allowing the PdH to discharge at open circuit for different discharge durations along the β to α transition plateau. The extraction charges were calculated from the stripping voltammograms recorded with a H_1-e Pd electrode (2*a* = 25 µm and Q_{dep} = 2 C cm^{-2}) in argon purged 20 mM PB I_s = 200 mM pH = 7 at room temperature.

3.8. Summary

In the present study, accurate cyclic voltammetric experiments at different cathodic limits and in presence of surface poison allowed the study of processes taking place on the palladium in its hydrogen region. Furthermore, the cathodic electrolysis is employed for loading H_1-e Pd films with hydrogen in order to prepare mesoporous palladium hydride micro pH sensors. It has been shown that the palladium hydride electrode can be prepared by galvanostatic or potentiostatic loading with hydrogen. The response proportional to the pH can be found during the discharge of the sensor when the electrode is in the transition between the β and α phases: that potential is stable and it is proportional to the log of the proton activity at the electrode-solution interface, therefore the potential is proportional to the pH. In order to have an accurate measurement of the pH, the potentiometric response of the electrode was studied in different buffers in order to obtain the calibration curve of OCP *vs*. pH shown in **Figure 3.5**. The curve show a linear response in the entire pH range with only one slope unlike other pH sensors and this linearity is in agreement with the theory. Remarkably, the linearity extends to pH 14 and we believe this is the first evidence of a pH microelectrode operating at such high pH. When oxygen is introduced into the system, the Nernstian response is no longer valid and the reproducibility worsens. The presence of oxygen also increases the loading time and decreases massively the lifetime of the sensor. In addition, the OCP is more positive, therefore a calibration curve was recorded also with two different oxygen concentrations, **Figure 3.12**. From **Figure 3.15** the limiting current for the ORR is very close to the extraction rate obtained from stripping voltammetry, **Figure 3.14**. It can be concluded that the ORR current drives the extraction of hydrogen from the hydride. In absence of oxidants, instead, the hydrogen extraction rate is two orders of magnitude smaller, inducing a much longer transition between the β and α phases of the PdH.

In the following chapter, the behaviour of H_1-e Pd microelectrodes will be discussed in the context of SECM experiments.

4. PdH SECM tips: from potentiometric to amperometric sensing.

4.1. Introduction to SECM experiments

The majority of scanning electrochemical microscopic (SECM) experiments is performed in the amperometric mode, but microelectrodes have also long been used as potentiometric sensors.

Potentiometric probes are the oldest form of electrochemical sensors. They can be used to study many chemical species that cannot be detected by amperometric techniques. In particular, hydrogen, alkali, alkaline earth metal ion concentrations of importance in biological system can be sensed with potentiometric ISE but not with amperometric techniques because they are not electroactive in aqueous media[270]. Other advantages of these ion selective tips are that they have a high selectivity towards the analyte and that potentiometric sensors are passive probes. In contrast to the amperometric probes, potentiometric devices do no alter the composition of the analyte in the sample. Since the electrode is not involving a Faradaic process, it does not alter the redox state of the species of interest, it does not does not consume/produce new species such as protons or hydroxyls, and it does not trigger mass transport in the analyte. This is particularly important for biological applications where the sample volume is very small.

As shown in chapter 5, the palladium hydride electrode is extremely sensitive to dissolved oxygen for both the lifetime of the sensor and the OCP recorded. In this chapter, the SECM is used to study the potential of the PdH tip during the natural extraction of hydrogen in aerated conditions at different tip-substrate distances in order to shield the flux of oxygen toward the tip and understand the relation that links the OCP and the ORR.

4.2. Amperometric approach curve with the ORR

The potentiometric use of SECM requires an independent determination of the absolute distance between the UME and the substrate. Usually potentiometric probes are made with micro-or nano- glass pipettes filled with ion carriers or the electrodes are made with fragile glass membrane electrodes, so it is important to limit their movements to avoid touching of the sample.

During the experiment, the location of the tip in the solution is known only relative to a reference position of the micro-positioning system. In the amperometric mode the tip produces or consumes redox species and the resulting concentration gradients in the space between the substrate and the tip have unique tip-current distance dependence. But in the potentiometric mode the tip is passive should not interfere with the concentration profiles except by screening the substrate surface from the bulk solution. Several procedures can be used to assess the tip-substrate distance and the simplest is to approach the tip under microscope observation until it is seen to almost touch the sample surface. This position is then defined as the zero on the apparent tip-substrate distance scale. This method can be used when an accurate estimation of the tip-substrate distance is not required. In the case of solid state electrode it is possible to switch from the amperometric mode of the SECM to the potentiometric mode. Metal oxides and metal hydrides potentiometric devices are advantageous because they can sustain Faradaic reactions and therefore operate in the conventional amperometric mode if a redox mediator is present in the solution. This is the way the PdH electrode was used: an approach curve was recorded in the conventional hindered diffusion amperometric mode of the SECM in order to assess the precise tip-substrate distance. Later, when the absolute tip substrate distance was known, the tip was electrochemically reconditioned to perform potentiometric measurements. Following this approach, the steady-state current for ORR was recorded on a nanostructured palladium microdisc while approaching a glass substrate. It is shown in **Figure 4.1** that the current decreases when moving the electrode close to an inert substrate. This is in agreement with the principle of hindered diffusion and the current-distance curve was exploited to determine the absolute tip-substrate distance by the use of the theoretical curve computed for a disc-shaped tip [295].

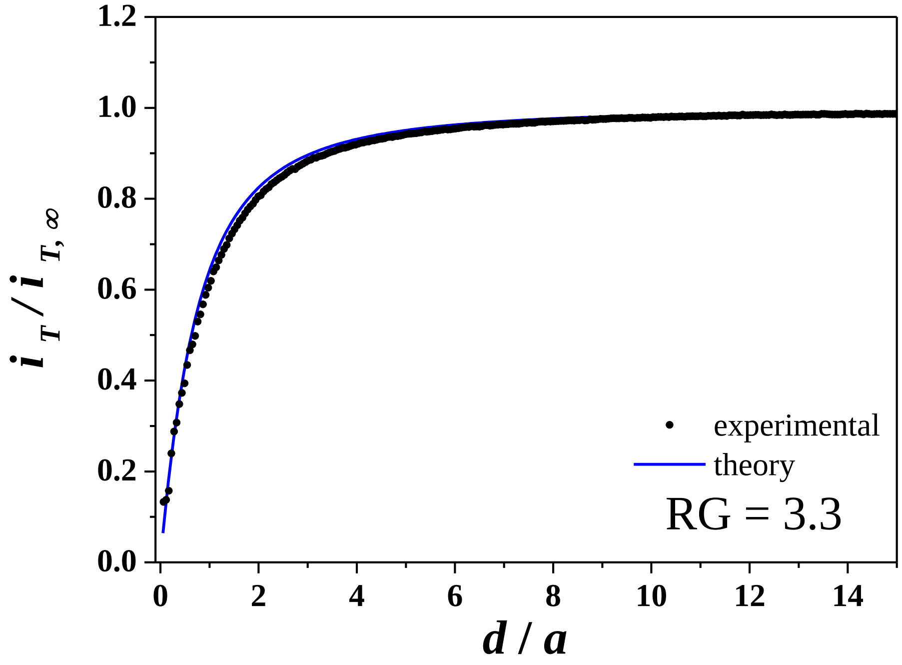

Figure 4.1 Amperometric approach curve recorded with a nanostructured Pd tip at 1 µm s^{-1} in aerated pH 7 phosphate buffer solution (I_s = 200 mM); *RG* = 3.3. *a* = 18.7 µm. The amperometric response was taken at -0.6 V *vs.* SMSE to ensure that the ORR was diffusion controlled over a glass substrate.

4.3. Potentiometric and amperometric observations as a function of *d/a*

When the desired tip-substrate distance was achieved, the tip was switched to the potentiometric mode and used to record different chronopotentiograms, cyclic voltammograms, linear sweep voltammograms for Tafel and linear polarisation experiments.

4.3.1. Potentiometric behaviour

Figure 4.2 shows a set of chronopotentiograms recorded at different tip-substrate distances above the inert substrate in the aerated phosphate buffer. They all show features characteristic of the loss of hydrogen from the palladium lattice. At short time the potential rises sharply as the β phase loses hydrogen and then reaches a plateau ($OCP_{\beta\rightarrow\alpha}$) when the α phase begins to nucleate within the β phase. As described in the previous chapter, this is the transition region where the phase rule dictates that the electrode potential only depends on the activity of protons in solution but not on the H/Pd atomic ratio. Only in this region, the electrode can be used as a pH sensor. At the end of the plateau the potential rises as the entire PdH is now in the α phase. At longer times, a second shoulder is observed that is thought to reflect the hydrogen desorption from the palladium surface. All these observation are consistent with the previous chapter. Surprisingly, all the chronopotentiograms depend on the tip substrate distance. As the tip approaches the inert substrate, the most important observation is that there is a significant increase in the lifetime of the phase transition. A second important observation is that the plateau potential, $OCP_{\beta \rightarrow \alpha}$, becomes more negative as the tip approaches the substrate. This cannot be due to a change in the pH of the solution because it is buffered, nor it can be due to the tip sensing an Ohmic drop, as there is no current flowing within the cell. Such a potential shift would be a major problem if the tip were about to be used to monitor pH.

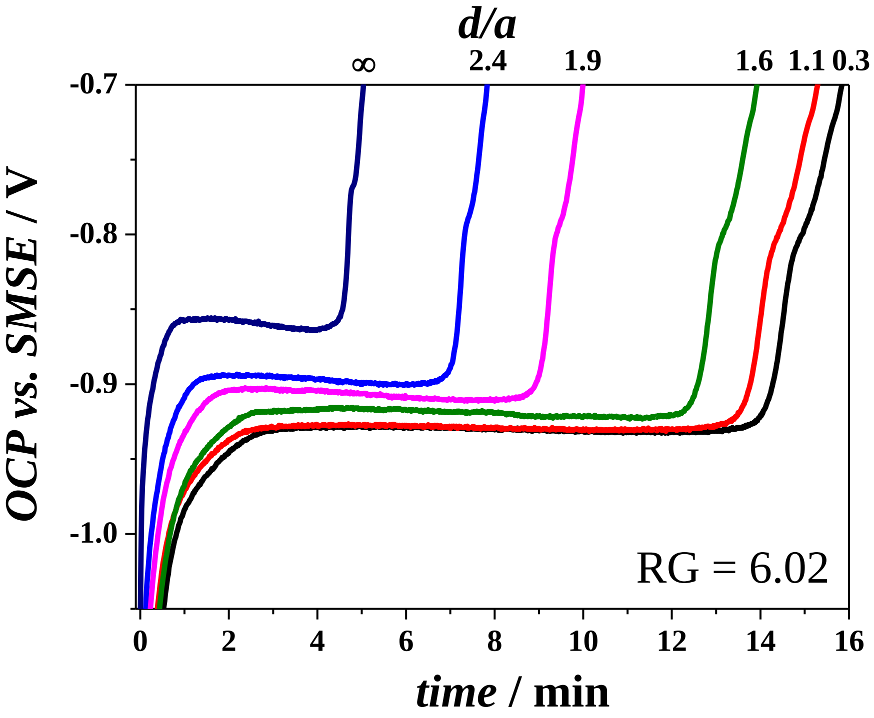

Figure 4.2 Chronopotentiograms recorded at several tip-substrate distances, *d*, in an aerated pH 7 buffer solution (I_s = 200 mM). *a* = 18.7 µm, *RG* = 6.

4.3.2. Cyclic voltammetry

At the same positions where chronopotentiograms were recorded, the potential was cycled in almost the entire potential range of the electrolyte until stable voltammograms were recorded at a scan rate of 50 mV s^{-1}. The potential was not swept too cathodically otherwise the current due to the oxidation of the hydrogen extracted from the bulk would have led to less clear features of the hydrogen adsorption peaks. These voltammograms are shown in **Figure 4.3**. **Figure 4.4** shows more clearly and with more details the changes in the voltammograms recorded in the hydrogen region when the tip was getting closer to the substrate. From both these graphs is it possible to observe that all the features described in **Figure 3.8** are unchanged. It can be seen that the peak potential of the oxides reduction peak is getting slightly more cathodic and smaller the closer the electrode is to the substrate. It can be noticed a strong dependence of the anodic peak *e* in the hydrogen region with the distance while the anodic peaks *f* and *g* do not look to be much affected by the different tip-substrate distances. It looks therefore that the hydride extraction peak is larger in the bulk than near the substrate. This may happen because the protons are hindered and the rate of hydrogen insertion decreases next to the substrate compared to the bulk. The hydrogen adsorption does not appear to be affected by the tip-substrate distance probably because the hydrogen absorption requires only one monolayer of hydrogen. Furthermore at the beginning of the anodic scan, between -1.2 V and -1.1 V in **Figure 4.4**, a broad peak has its relative maximum changing to more anodic voltages as the tip gets closer to the substrate. As the tip-substrate distance decreases, the voltammograms shift up because the limiting current for the ORR decreases due to hindrance.

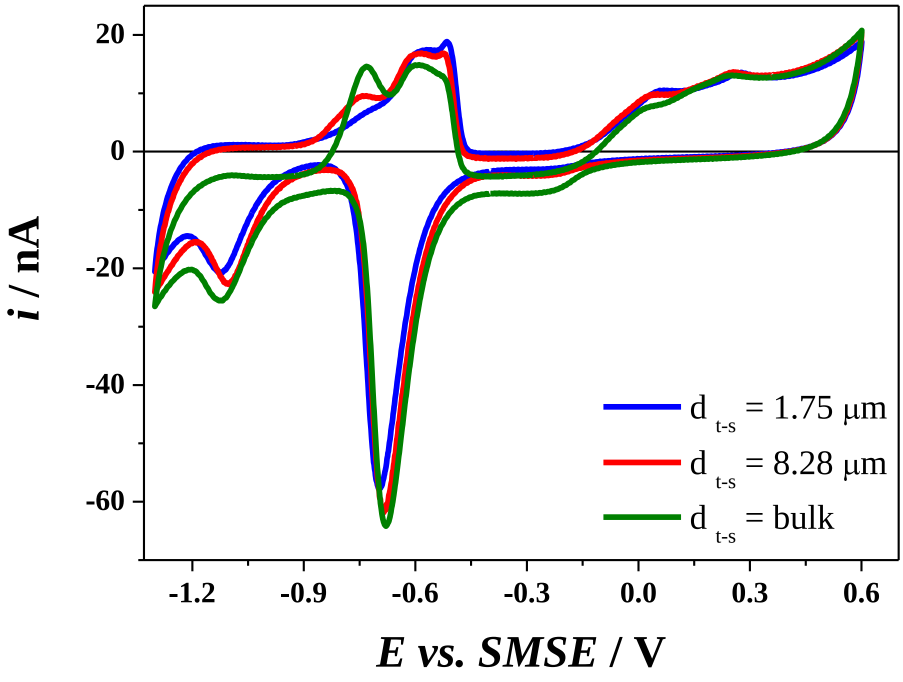

Figure 4.3 Cyclic voltammograms for the H_1-e Pd tip (*RG* = 10, *a* = 5 μm, Q_{dep} = 10 C cm^{-2}) recorded at *v* = 50 mV s^{-1} for different distances with respect to the substrate. The solution used was an aerated 5×10^{-5} M H_2SO_4 + 0.5 M Na_2SO_4 in an open cell.

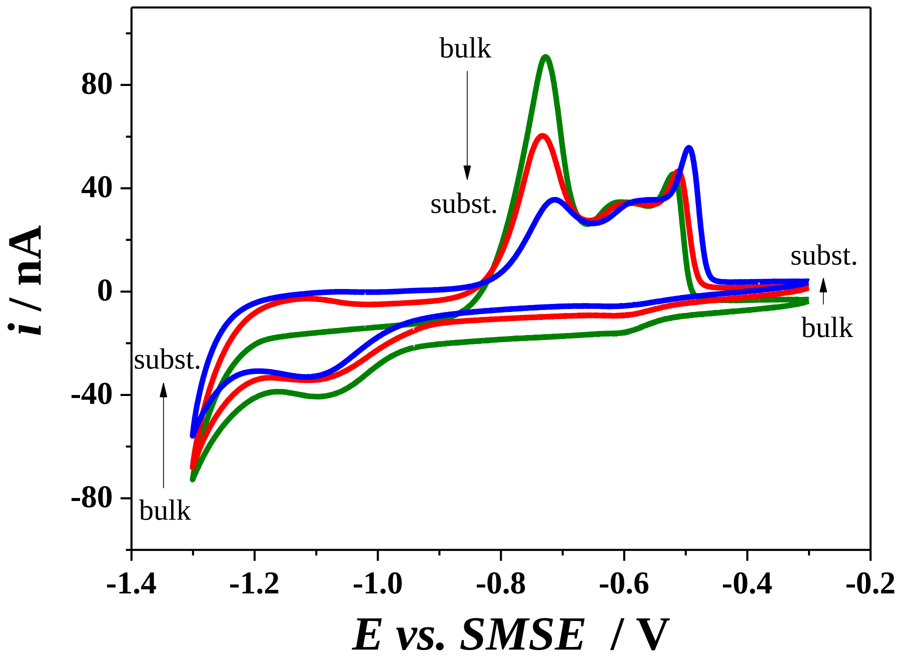

Figure 4.4 Cyclic voltammograms for the H_1-e Pd film (*RG* = 5.35, *a* = 12.5 µm, Q_{dep} = 10 C cm^{-2}) recorded at different distances with respect to the substrate. The solution used was an aerated 5×10^{-5} M H_2SO_4 + 0.5 M Na_2SO_4 in an open cell. The voltammograms were recorded in the hydrogen region at v = 20 mV s^{-1}. The harrows indicate the sequence in which the voltammograms where recorded when decreasing the tip-substrate distance.

4.3.3. Tafel and Linear Polarization Resistance (LPR) experiments

The behaviour of the PdH electrode was studied in aerated buffered conditions by recording $OCP_{\beta\rightarrow\alpha}$ and LSV experiments at different tip-substrate distances, therefore at different rates of ORR. These linear sweep voltammograms were recorded at 1 mV s^{-1} ± 100 mV around the $OCP_{\beta\rightarrow\alpha}$ and they are shown in **Figure 4.5** presented as Tafel plots in the top part of the figure. The equilibrium potentials found with the potential sweeps are in agreement with the $OCP_{\beta\rightarrow\alpha}$ values measured by chronopotentiometry at the same tip positions, as shown in the bottom part of **Figure 4.5**. The corresponding exchange currents, from now on called hydrogen extraction currents, were estimated from the intercept between the cathodic Tafel branch and the vertical line corresponding to the equilibrium potential. Finding a clear linear region over one decade of current proved difficult; for this reason, the extraction currents, $i_{T,ex}$, were also estimated from the polarization resistance $\left(i_{T,ex} = \frac{RT}{nFR_P}\right)$ determined from the gradient of the LSV taken within ±10 mV of the equilibrium potential for several tip-substrate distances, **Figure 4.6**.

The extraction currents found from R_P are in good agreement with those derived from Tafel plots and follow the same tip-substrate distance dependence, **Figure 4.7**. The latter also shows that the extraction currents are comparable in magnitude with the limiting currents for the ORR at all tip-substrate distances. These results therefore strongly suggest that the kinetics of the hydride oxidation is controlled by the diffusion of oxygen to the PdH tip.

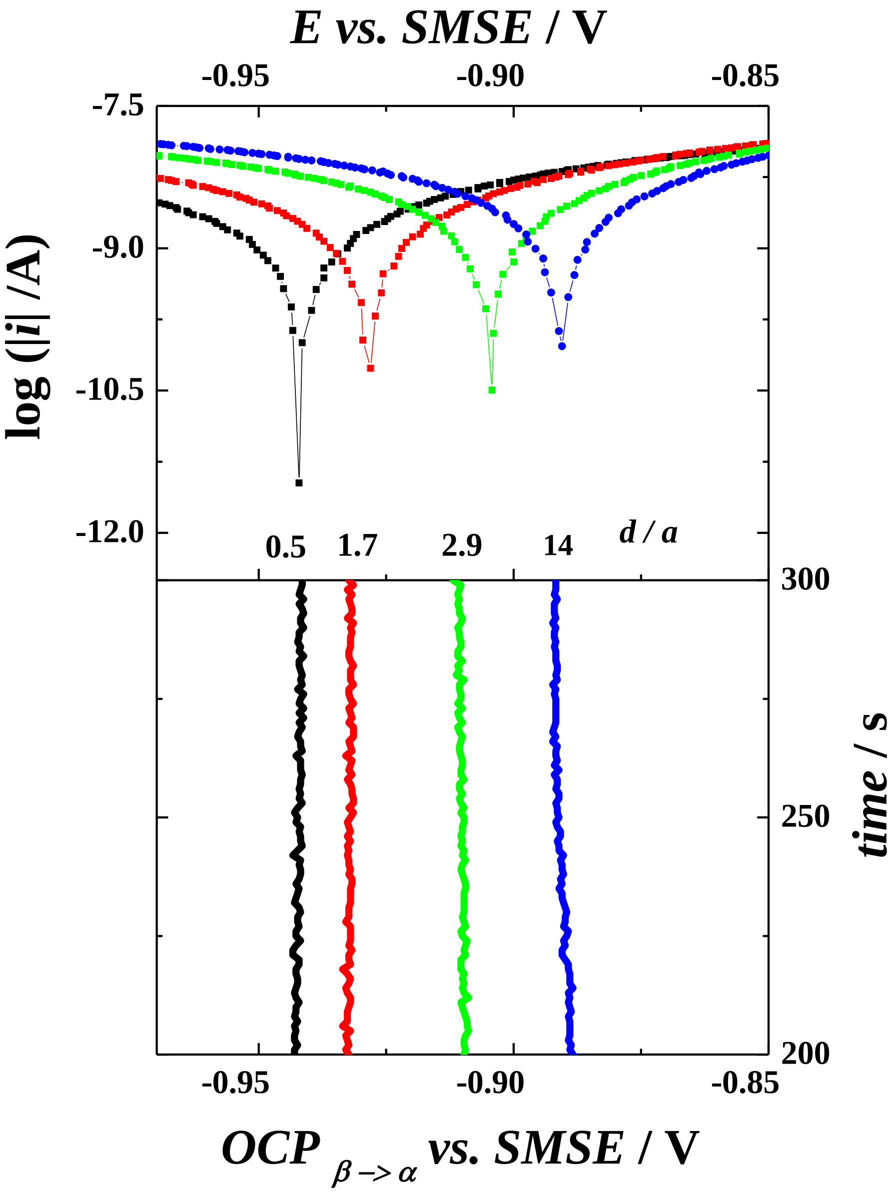

Figure 4.5 Comparison between Tafel experiments (top) and chronopotentiograms at $OCP_{\beta\rightarrow\alpha}$ (bottom) recorded at the tip-substrate distance indicated by *d/a*. LSV were taken at 1 mV s^{-1} around $OCP_{\beta\rightarrow\alpha}$.in aerated pH 7 buffer solution (I_s = 200 mM) with a H_1-e Pd tip (a = 17.15 µm, RG = 5, Q_{dep} = 10 C cm^{-2}).

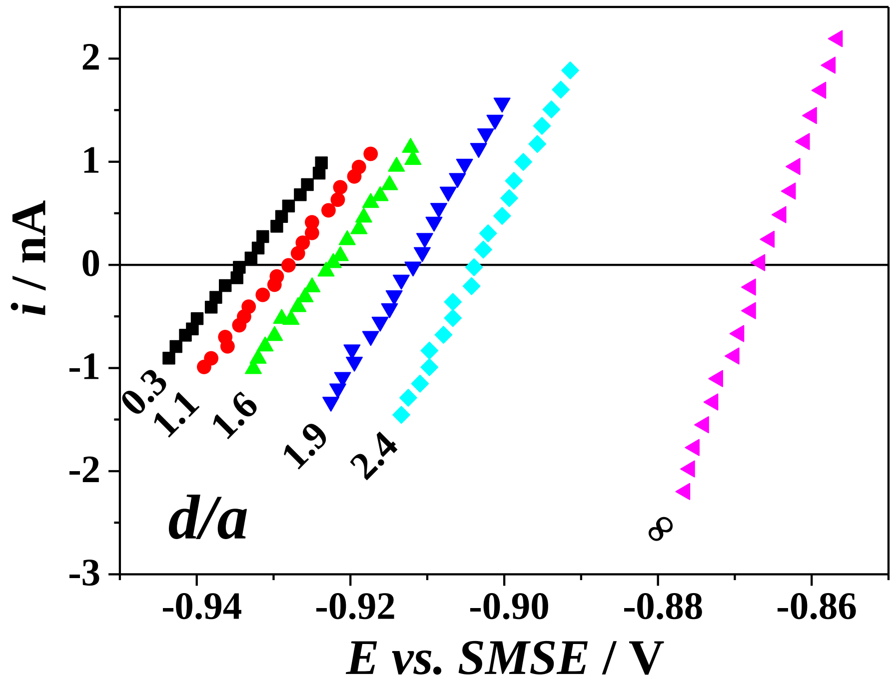

Figure 4.6 Linear sweep voltammograms (LSV) recorded at 1 mV s^{-1} around $OCP_{\beta\rightarrow\alpha}$ to determine the linear polarization resistance at the tip-substrate distances indicated by *d/a*. LSV were taken at 1 mV s^{-1} in aerated pH 7 buffer solution (I_s = 200 mM) with a H$_1$-e Pd tip (a = 18.7 µm, RG = 6, Q_{dep} = 10 C cm^{-2})

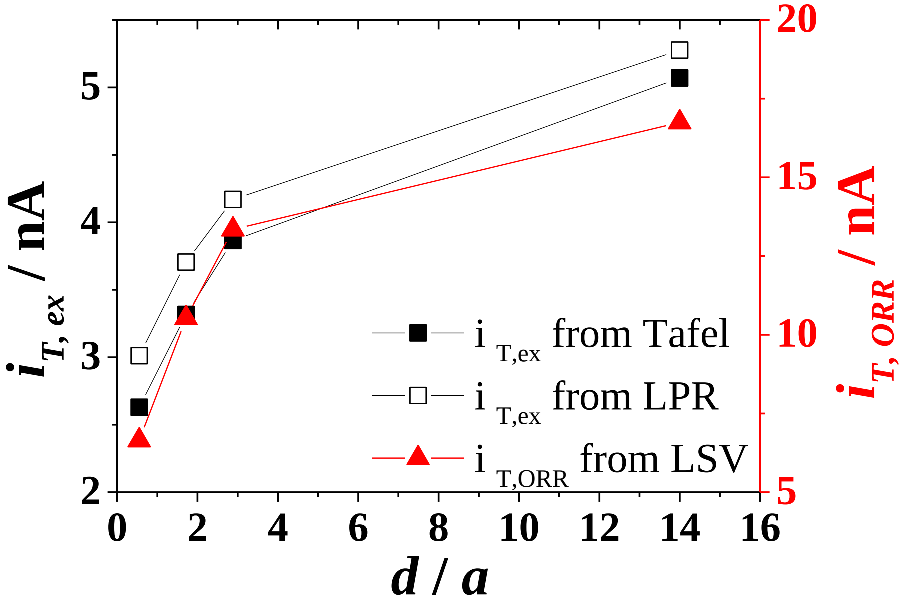

Figure 4.7 Comparison between the hydrogen extraction currents (left Y-axis) and the limiting currents for oxygen reduction (right Y-axis) recorded at different tip-substrate distances. The extraction currents were estimated from the Tafel plots presented in **Figure 4.5** and from the linear polarization resistance (not shown).

4.4. Potentiometric approach curve

A potentiometric approach curve recorded to assess the dependence of $OCP_{\beta \rightarrow \alpha}$ on the tip-substrate distance is shown in **Figure 4.8**. The duration of the approach curve was kept shorter than the duration of the β to α transition to prevent any variation of the tip potential with the hydride composition. The curve confirms that the potential becomes more negative as the tip-substrate distance decreases. Surprisingly, the dependence of the potential on the tip-substrate distance matches the amperometric approach curve recorded with the same tip for the reduction of dissolved oxygen. The latter is in perfect agreement with the theoretical curve for hindered diffusion [295] shown in **Figure 4.1**, thereby confirming that the nanostructured film is sufficiently thin to behave as a disc. **Figure 4.8** clearly suggests that the potentiometric response was driven by a process analogous to hindered diffusion at all tip-substrate distances. The only redox active species present in the solution being oxygen, the tip potential must be related to the rate of the oxygen reduction reaction. Palladium is known to be a good catalyst for promoting the ORR [296-298], and the nanostructured palladium is expected to be even better as found for nanostructured Pt tips prepared by the same method [299]. As a result, the wave for ORR occurs at very positive potentials (circa -0.1 V *vs*. SMSE from the reverse sweep and -0.35 V *vs.* SMSE from the forward sweep) according to **Figure 4.9** and the $OCP_{\beta \rightarrow \alpha}$ is more negative than the potential for the ORR wave. This potential difference is sufficiently large that the nanostructured PdH tip promotes the ORR at a diffusion controlled rate at all pH. In presence of oxygen, two Faradaic processes are therefore balanced at $OCP_{\beta \rightarrow \alpha}$: the electrochemical oxidation of the hydride and the electrochemical reduction of the oxygen. Any increase in the oxygen flux toward the electrode is matched by an increase in the PdH oxidation rate and therefore by a larger hydrogen extraction rate.

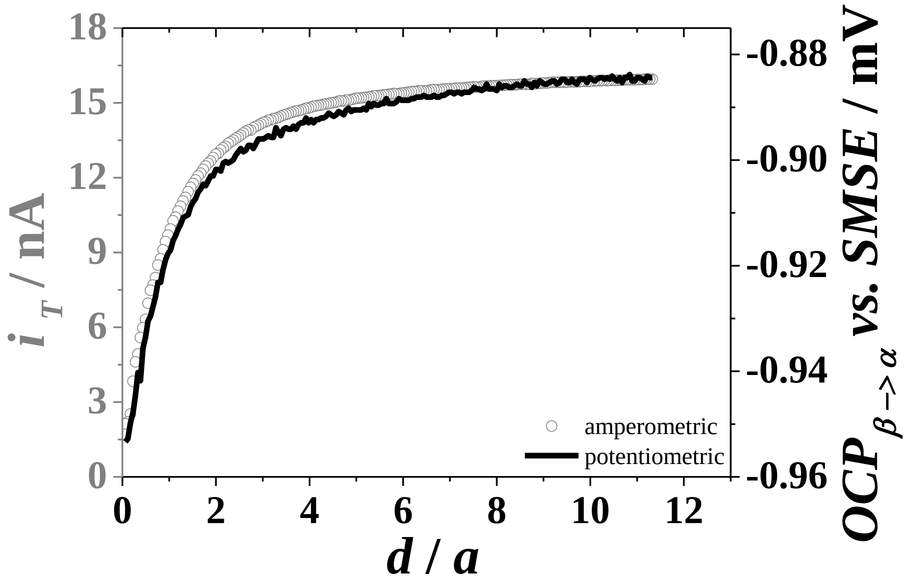

Figure 4.8 Comparison with potentiometric (right Y-axis) and amperometric (left Y-axis) approach curves recorded with a nanostructured Pd tip at 1 µm s^{-1} in an aerated pH 7 phosphate buffer solution (I_S = 200 mM); *RG* = 3.3, *a* = 18.7 µm. The amperometric response was taken at -0.6 V *vs.* SMSE to ensure that ORR was diffusion controlled. The potentiometric response is the open circuit potential taken in the β to α transition of the palladium hydride.

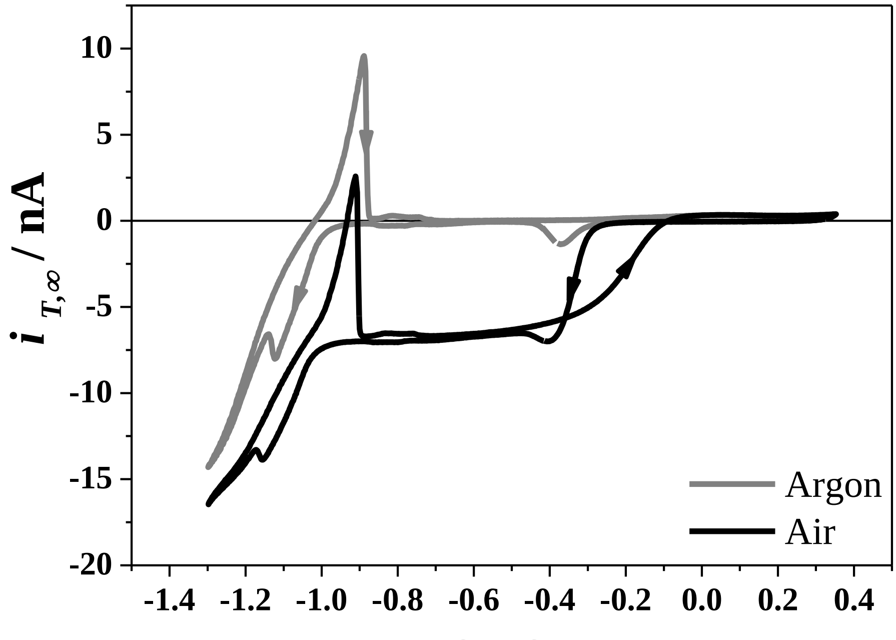

Figure 4.9 Cyclic voltammograms recorded with and without dissolved oxygen with a nanostructured palladium tip (*a* = 7.9 µm; *RG* = ∞) at 1 mV s^{-1} in a pH 7.5 phosphate buffer solution, I_S = 200 mM.

4.5. The mixed potential model

It is possible to argue that the potential observed in presence of oxygen reflects a pH change due to the ORR, but if this was the case, the potential shift should be negative because the ORR is making the solution near the electrode more alkaline; experimentally the shift is always found to be positive. Instead the potentiometric and amperometric results suggest that the potential of the PdH tip obtained in presence of dissolved oxygen is not the thermodynamic potential predicted from the phase rule, but it is a mixed potential defined where the rate of anodic and cathodic processes are equal. This is akin to the mixed potential concept used in corrosion [300] and catalysis [301, 302]. The main anodic reaction is the extraction of hydrogen from the hydride, while the main cathodic reaction is the reduction of oxygen on the nanostructured Pd surface. The oxidation of the PdH can thus be thought of as a corrosion problem: the larger the flux of oxygen, the higher the anodic current must be to match the cathodic current. As a result, the tip potential shifts to more positive values as schematically shown in **Figure 4.10** for three tip-substrate distances. When $d = 0$ the diffusion of oxygen is fully hindered and $E_{T,d=0}$ equals $OCP_{\beta\rightarrow\alpha}$ in absence of any oxygen ($OCP_{\beta\rightarrow\alpha,\text{ no O2}}$). At a distance $d_1 > 0$, hindrance has decreased and a small flux of oxygen forces the tip to take the mixed potential $E_{T,d_1} > E_{T,d=0}$. At the distance $d_2 > d_1$, hindrance is much less pronounced and a large flux of oxygen forces the tip to take the mixed potential E_{T,d_2} such that $E_{T,d=0} < E_{T,d_1} < E_{T,d_2}$. The schematics also suggest that for any tip-substrate distance d, the mixed potential $E_{T,d}$ can be simply estimated as a linear function of the diffusion-controlled current for ORR at d, $i_{T,d,ORR}$, via the polarization resistance recorded in absence of oxygen, $R_{p,no\ O2}$, the latter being the inverse of the current-potential curve of the PdH tip recorded in the absence of oxygen.

$$E_{T,d} = OCP_{\beta\rightarrow\alpha,no\ O_2} + \left|i_{T,ORR}\right| \times R_{p,no\ O_2} \qquad (32)$$

This expression was tested for a nanostructured PdH microdisc with a small tip ($a = 7.9$ µm, $RG = \infty$) to enhance the flux of oxygen to the electrode and produce a larger potential shift. In this experiment, performed in a pH 7.5 phosphate buffer, all the parameter in the right hand side of equation (32) were measured in the bulk so that the rate of ORR was at its maximum. Using the measured data for $OCP_{\beta\rightarrow\alpha,\text{no O}_2}$ (-1000 ± 3) mV and $R_{p,\text{ no O}_2}$ (21.6 MΩ), both recorded in argon-purged solution and shown respectively in **Figure 4.11** and **Figure 4.12** with the blue plots, and of $i_{T,d,ORR}$ (-7.14 nA) recorded in aerated condition, **Figure 4.13**, the calculated tip potential (-840 mV) was in good agreement with the tip potential measured in the aerated pH 7.5 buffered solution (-844 ± 3) mV, shown as the red chronopotentiogram in **Figure 4.11**.

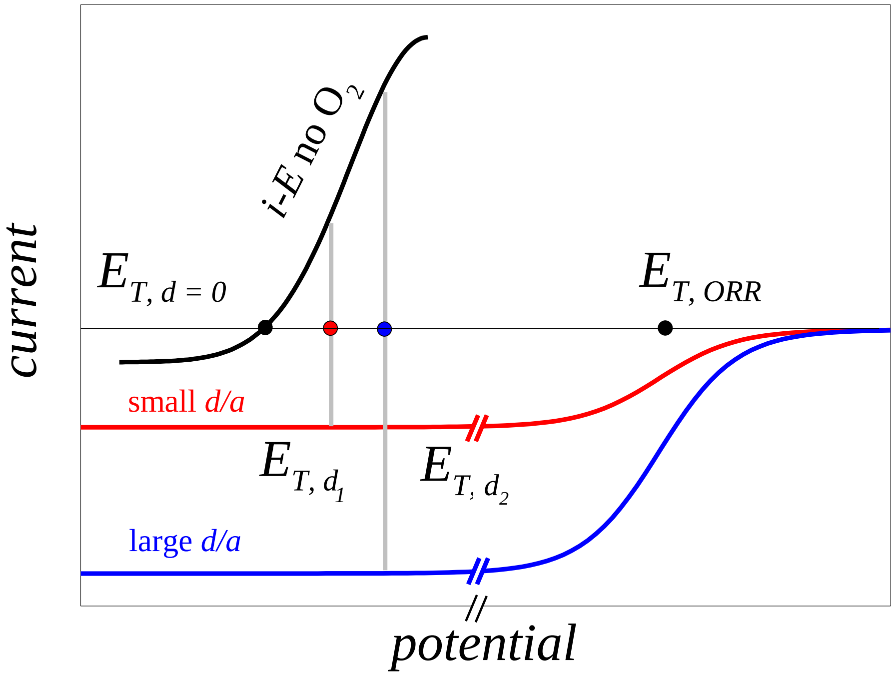

Figure 4.10 Schematic representation of the interplay between the current potential curves for the anodic (H extraction from Pd, **black**) and cathodic (ORR on the palladium surface, **blue** and **red**) processes leading to a mixed potential different from the thermodynamic value of potential found in the absence of dissolved oxygen. To illustrate the dependence of the tip potential on the flux of oxygen, the sketch is drawn for three tip-substrate distances, $d = 0 < d_1 < d_2$. $E_{T, ORR}$ is the half-wave potential for the ORR on the tip.

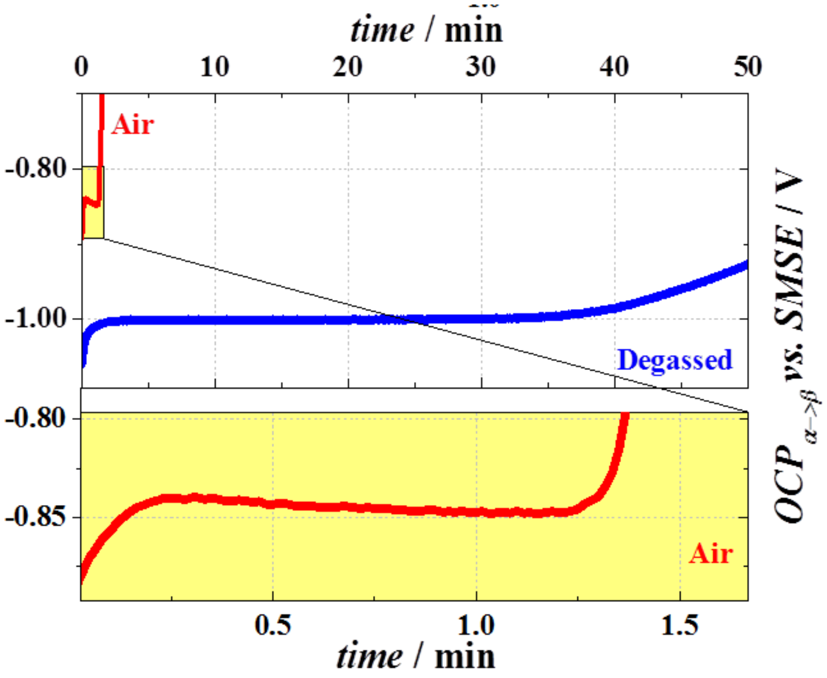

Figure 4.11 Chronopotentiograms recorded with (**blue**) and without dissolved oxygen (**red**, also reproduced below with a different time scale) with a nanostructured palladium tip (*a* = 7.9 µm; *RG* = ∞) at in a pH 7.5 phosphate buffer solution I_S = 200 mM.

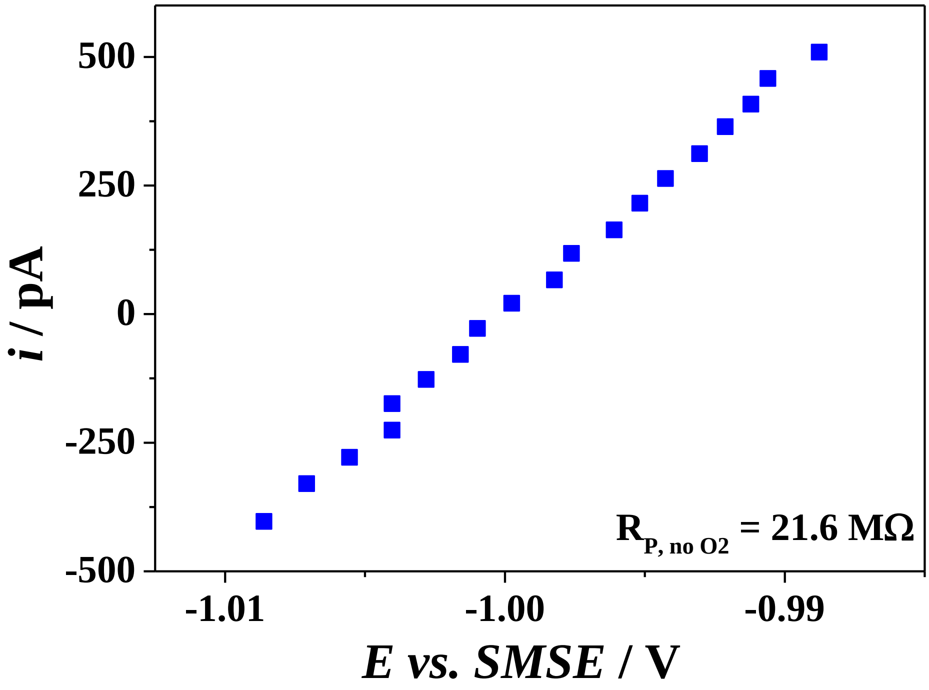

Figure 4.12 LSV recorded at 1 mV s^{-1} around $OCP_{\beta\rightarrow\alpha}$ to determine the linear polarization resistance in argon-purged solution. The experimental conditions are the same as the one used in the experiments in **Figure 4.11**.

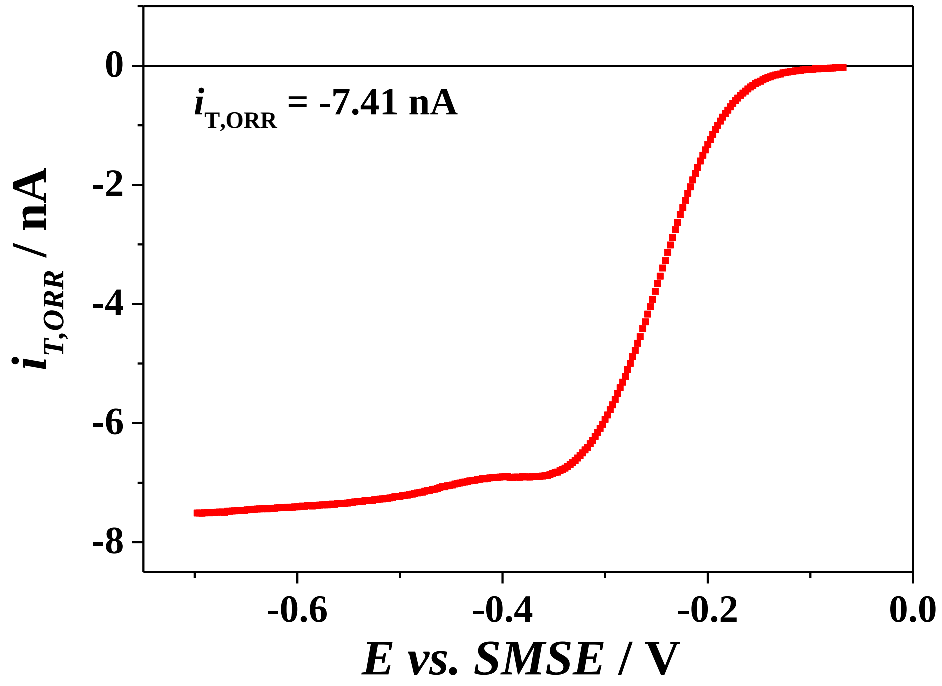

Figure 4.13 Voltammogram for the ORR recorded in the bulk in presence of air with the same experimental conditions used for the experiments in **Figure 4.11** and **Figure 4.12**.

4.5.1. The linear dependence between $OCP_{\beta\rightarrow\alpha}$ and $i_{T,ORR}$

By using the tip employed in **Figure 4.8**, equation (32) was then tested against all tip-substrate distances by plotting the potentiometric approach curve ($OCP_{\beta\rightarrow\alpha}$ *vs.* d) against the amperometric approach curve ($i_{T,ORR}$ *vs.* d), both taken from **Figure 4.8**. **Figure 4.14** shows a clear one to one correlation between the two approach curves. Furthermore, the intercept (-967 mV) which corresponds to a tip current equal to zero, as would be found with complete hindrance, is in perfect agreement with the thermodynamic potential measured in the absence of oxygen ($OCP_{\beta\rightarrow\alpha,\mathrm{no}\ O_2}$ = -973 mV) in the pH 7 buffered solution; their difference is within the experimental error of 6 mV. The slope (4.48 MΩ) is one order of magnitude larger than $R_{p,\,no\ O_2}$ obtained for this tip (26.8 MΩ).

Despite a good agreement found in the bulk, equation (32) should only be valid for low oxygen concentrations where the potential shift remains sufficiently small that the PdH current-potential relationship is linear. For high oxygen fluxes, i.e. small tips in the bulk with large oxygen concentrations, the potential shift becomes so large that the PdH current-potential relationship becomes curved and the mixed potential is no longer a simple linear function of the limiting current for the ORR. This can be easily seen on the current potential curve recorded in the absence of oxygen with the small tip, **Figure 4.9**. With small PdH nanostructured tips the high oxygen flux discharges hydrogen rapidly and the lifetime of the β to α transition plateau becomes unworkably short. In oxygen saturated solutions, it is difficult to observe a stable plateau with the 25 µm diameter tips prepared as described above. With larger tips it is possible to deposit thicker nanostructured film, thereby increasing the hydrogen reservoir, and operate in oxygen saturated solutions.

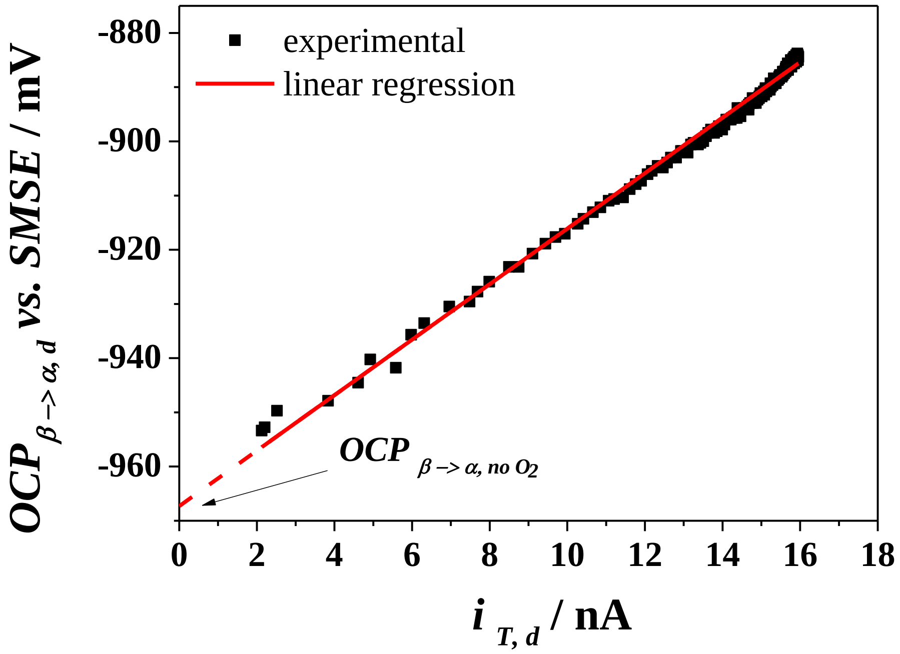

Figure 4.14 Plot of the tip potential recorded at different tip-substrate distances against the diffusion-controlled current for ORR recorded at the same tip-substrate distances. All the experimental details as for **Figure 4.8**.

4.5.2. Rotating Disc Electrode confirmation

In order to verify that the potentiometric response observed with the SECM tip was generic, similar experiments were conducted with a nanostructured Pd film deposited on a rotating disc electrode and loaded with hydrogen to H/Pd = 0.6. The potential of the electrode, recorded for several rotation rates in aerated pH 7 phosphate buffer solution, was found to increase linearly with the square root of the rotation rate and the intercept was found to be within 3 mV of the potential measured in argon-purged solution. The RDE data therefore confirm the observations made with the SECM tip.

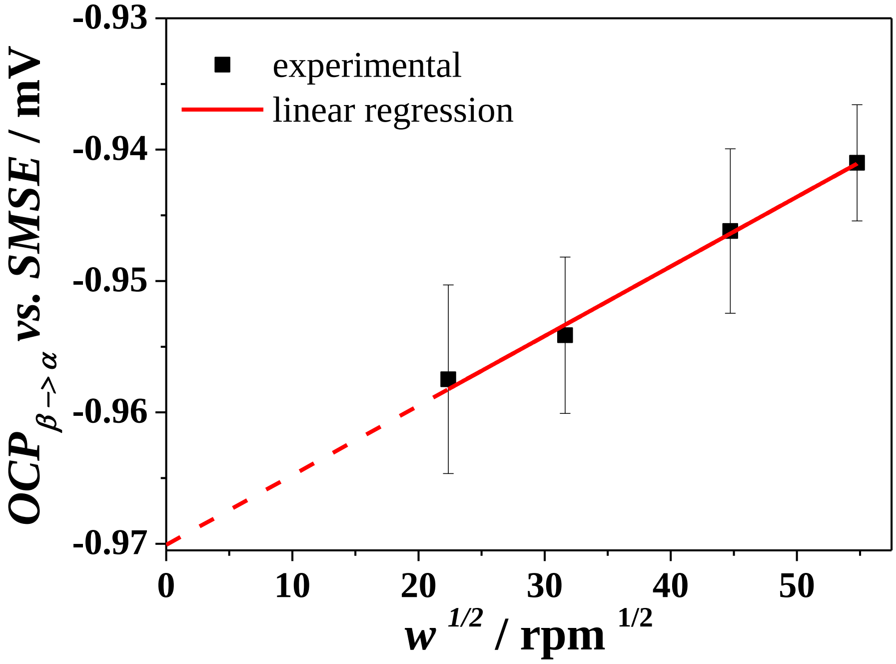

Figure 4.15 Plot of the dependence of $OCP_{\beta\rightarrow\alpha}$ on rotation, w, for a nanostructured Pd RDE in aerated pH 7 phosphate buffer solution, I_s = 200 mM. The Pd film was electrodeposited (Q_{dep} = 4 C cm^{-2}) on a 5 mm diameter platinum rotating disc.

4.6. Theoretical approach and validity

While equation (32) is qualitatively convenient to explain the correlation between potentiometric and amperometric approach curves, its quantitative use is limited to conditions such that the potential shift is no greater than ca. 50 mV. Let us assume that the hydrogen insertion/extraction reactions at the Pd surface follow the Butler-Volmer kinetics. At the mixed potential the rate of hydrogen extraction is equal and opposite to the rate of oxygen reduction on the surface represented by the equality:

$$i_c = i_a^0 \exp\left(\frac{F\,n_a}{RT}(1-\alpha_a)(E_m - E_a^0)\right) \tag{33}$$

where i_c, i_a^0, n_a, α_a, E_m, E_a^0 are respectively the cathodic current, exchange current for the anodic process, number of electrons involved in the anodic process, anodic transfer coefficient, mixed potential and standard potential for the anodic reaction. Provided $\frac{F\,n_a}{RT}(1-\alpha_a)(E_m - E_a^0) < 1$, the exponential can be linearized and expression (33) becomes:

$$i_c = i_a^0 \left(1 + \frac{F\,n_a}{RT}(1-\alpha_a)(E_m - E_a^0)\right) \tag{34}$$

Further rearrangements yield:

$$E_m = E_a^0 + \frac{RT}{Fn_a(1-\alpha_a)}\left(\frac{i_c}{i_a^0} - 1\right) \tag{35}$$

$$E_m = E_a^0 - \frac{RT}{Fn_a(1-\alpha_a)} + \frac{RT\,i_c}{Fn_a(1-\alpha_a)i_a^0} \tag{36}$$

$$E_m = E_a^0 - \frac{RT}{Fn_a(1-\alpha_a)} + \frac{R_{p,a}}{(1-\alpha_a)} \times i_c \tag{37}$$

where $R_{p,a}$ is the anodic polarization resistance. Expression (37) predicts a linear dependence of the mixed potential on the limiting current for the ORR but this approximation in only valid when $\frac{F\,n_a}{RT}(1-\alpha_a)(E_m - E_a^0) < 1$ and so when the potential shift is:

$$E_m - E_a^0 < \frac{RT}{Fn_a(1-\alpha_a)} \tag{38}$$

and so when $E_m - E_a^0 < 0.051\ V$ at 25°C with $n_a = 1$ and $\alpha_a = 0.5$.

4.7. Summary

This study demonstrated how the potentiometric mode of SECM can be used to sensitively probe and alter the mixed potential due to two independent redox processes provided that the transport of one of the species involved is controlled by diffusion. This was illustrated with the discharge of hydrogen from nanostructured Pd hydride films deposited on the SECM tip. In deaerated solutions, the OCP of the PdH in equilibrium between its β and α phases does not depend by the tip substrate distance while in aerated conditions it is found to be controlled on hindered diffusion of oxygen. Chronopotentiometric and amperometric measurements at several tip-substrate distances reveal how the flux of oxygen toward the Pd hydride film determines its potential. LSV shows that the polarization resistance increases when the tip approaches an inert substrate. The SECM methodology also demonstrates how dissolved oxygen affects the rate of hydrogen extraction from the Pd lattice. Over a wide potential window, the highly reactive nanostructure promotes the reduction of oxygen which rapidly discharges hydrogen from the PdH. The flux of oxygen toward the tip can be adjusted via hindered diffusion. Approaching the substrate decreases the flux of oxygen, lengthens the hydrogen discharge and shifts the OCP negatively. The results are consistent with a mixed potential due to the rate oxygen reduction balancing that of hydride oxidation. The methodology is generic and can be applied to other mixed potential processes in corrosion and catalysis.

5. *In situ* monitoring carbonation in a porous medium

5.1. The application of the PdH-pH electrode.

Numerous chemical reactions involve pH changes but despite its importance pH still remains a difficult parameter to determine in many cases. On the one hand extreme pHs cannot be measured with most pH sensitive devices, including the conventional glass electrode. On the other hand pH is hard to measure in confined places with interfacial processes typically found in geochemistry, electrochemistry or biochemistry proving to be particularly challenging. Of all the pH sensors currently available the glass electrode is by far the most convenient for measurements in bulk solutions but it is unsuited for operations in localised environments. It is also unsuited to very basic media as the alkaline error (a phenomenon also known to increase with temperature[303]) affects the response for pH > 9; even with alkali glass membranes[283] its range does not extend beyond pH 12. Among all the approaches cited in section 1.3, the palladium hydride (PdH) electrode stands out as the only one capable of producing a single Nernstian response over the whole pH range[304]. It can be turned into a microdisc electrode to perform localised measurements but its potentiometric response is not stable with time as the hydrogen diffuses in to the bulk of the Pd wire. To circumvent this problem Imokawa *et al.*[206] electrodeposited thin nanostructured Pd films onto Pt microdiscs and showed that, once loaded with H, the PdH film exhibited a single Nernstian response from pH 2 to 12. We confirmed in chapter 3 that this response can be extended up to pH 14 with high stability and excellent reproducibility (**Figure 3.5**). Imokawa *et al.*[206] also reported that the lifetime of the nanostructured PdH microdiscs was seriously shortened by the presence of dissolved oxygen. In chapter 3 and 4, we showed that the presence of oxygen also affects the potentiometric response where, instead of delivering a potential proportional to pH, the electrodes produce a mixed potential related to pH and to the flux of oxygen towards the electrode as it reduces on the nanostructured Pd film (**Figure 4.10**). We also were able to quantify the offset due to the presence of oxygen by the use of equation (32) and the calibration curve in air and oxygen saturated solution shown in **Figure 3.12**. The offset is significant only for very small electrodes since they promote higher ORR fluxes; furthermore it increases when the pH is larger than 1.5 as shown in the calibration curve in **Figure 3.12**.

In this chapter we describe how nanostructured Pd hydride microelectrodes were successfully exploited to monitor pH variations from a reaction confined in a porous substrate with solutions ranging from very alkaline to mildly acidic. In chapter 3, through calibrations, we first demonstrated that the potentiometric pH characteristic of the microelectrodes follows a single Nernstian response even in strong alkaline conditions and in chapter 4 we quantified the effect of oxygen on the calibration curve. In this chapter we employ the electrodes to record pH transients during the carbonation of lime within a humid fibrous mesh. To control the carbonation we performed the experiments with different partial pressures of CO_2 and in each case validated the experimental results with theoretical calculations from PHREEQC[305] and with SEM and XRD analysis of the $CaCO_3$ particles deposited on the mesh fibres.

5.2. A typical experimental procedure

Experiments with the carbonation of lime were carried out with saturated solutions of $Ca(OH)_2$ absorbed in small strips (3 mm wide × 1 cm long) of cellulose mesh (lens cleaning paper, pure cellulose supplied by Whatman) inside a homemade poly(methyl methacrylate) (PMMA) cell (**Figure 2.5**) under thermostatic conditions (23°C) and with different Ar/CO_2 gas mixtures.

The cellulose mesh was used for three reasons: to trap a thin film of solution and thus simulate carbonation in the confinement of a porous medium, to provide an ionic path between the electrodes and to capture the solid phases formed during the carbonation for subsequent analysis. A typical experiment was conducted as follows: 1) the cellulose mesh was wrapped around the counter electrode. 2) The electrodes were positioned in the cell and clamped with the lid. 3) A stream of wet Ar was sent into the cell. 4) The cell was filled with about 3 ml of saturated $Ca(OH)_2$ solution using a syringe fitted with a disposable filter (0.1 µm Puradisc 25 TF from Whatman) to avoid introducing solid phases. 5) Cyclic voltammograms were recorded to check the cleanliness of the Pd nanostructure. 6) A chronopotentiogram was recorded while loading the palladium film galvanostatically with hydrogen to a H/Pd ratio circa 0.6 corresponding to the beginning of the β phase of the hydride. 7) The microelectrode was set to open circuit and its potential was recorded to measure the pH in the bulk of the solution. 8) While continuously recording its potential the microelectrode was moved downwards until its tip touched the cellulose mesh. 9) After checking for signal stability, the solution was removed from the cell using the syringe and capillary at the bottom of the cell thereby leaving some solution absorbed in the cellulose mesh. 10) The baseline pH for the thin film of solution was recorded. 11) The gas mixture was modified to allow a chosen partial pressure of humid CO_2 in the cell. 12) The electrode potential was recorded continuously while carbonation occurred until a stable plateau was reached. The solid phases precipitated within the mesh samples were subsequently observed with a field emission scanning electron microscope and analysed with an X-ray diffractometer.

5.3. Modelling of the results with PHREEQC

Results of experimental measurements were compared with results of PHREEQC calculations. PHREEQC is a computer program for simulating chemical reactions and transport processes in natural or polluted water, in laboratory experiments, or in industrial processes. The program is based on equilibrium chemistry of aqueous solutions interacting with minerals, gases, solid solutions, exchangers, and sorption surfaces (which accounts for the original acronym: pH-REdox-EQuilibrium) but over the years it has evolved to include the capability to model kinetic reactions and one-dimensional transport.[305] This software has already been used in several scientific fields such as geochemistry, hydrology and environmental pollution and was also used to study the phase and morphology evolution of calcium carbonate precipitated by carbonation of hydrated lime[306].

Simulations used in these tests were carried out using a solution and two equilibrium phases as initial conditions, according to a method already used by other researchers[307, 308]. The solution was made of 1 kg of pure water (set by default to pH = 7 and pe = 4, i.e. to a redox potential of 0.237 V *vs.* SHE) as solvent with the addition of calcium to simulate saturated solutions. In all simulations the pH was left as a variable to allow charge balance. The calculations were carried out at 20, 23 and 25°C.

Gaseous carbon dioxide and one of the anhydrous polymorph of calcium carbonate where considered as equilibrium phases. According to the instruction provided with the software, for the gaseous phase the log of p_{CO2} (in bar) was considered instead of the saturation index required for the solid phases. The number of moles of carbon dioxide were set to high values to model the equilibrium with an infinite reservoir of $CO_{2(g)}$. The solid phase considered to form during the reaction (monohydrocalcite, vaterite, aragonite or calcite), was modelled using a saturation index of 0 and an infinite reservoir (although similar results were obtained without considering the number of moles of solid phase introduced). The database used for the simulations was a modified version of the database developed by the Lawrence Livermore National Laboratory (LLNL) of Berkeley (California, USA). Modification consisted in the addition of data for vaterite (not included in this database) with data taken from the SIT database, developed by the French National Radioactive Waste Management Agency.

According to PHREEQC calculations (**Table 5.1**), the initial pH of $Ca(OH)_2$ saturated solutions at 20, 23 and 25°C are, respectively, 12.56, 12.45 and 12.37. The final pH, instead, varies from a minimum of 6.08 for a solution in equilibrium with calcite at 25°C and p_{CO2} = 0.75 atm, to a maximum of 7.21 for a solution in equilibrium with monohydrocalcite at 23°C and p_{CO2} = 0.038 atm. At 23°C temperature, the final pH of a solution in equilibrium with calcite varies from 6.08 to 6.92, depending on the p_{CO2}.

Simulations show that pH is more acidic in presence of calcite compared to the other solid phases and that it takes more neutral values with the less stable phases (respectively, aragonite, vaterite and monohydrocalcite). Aragonite produces pH values more similar to those produced by calcite while monohydrocalcite produces pH values closer to those produced by vaterite.

The same simulations show that temperature has little effect on the final pH of the solutions in the range between 20 and 25°C. The smallest difference was found between the pH of two solutions at 20 and 25°C containing monohydrocalcite (0.001 pH) while the highest difference was found between the solutions containing vaterite (0.011 pH).

Table 5.1 Theoretical pH values calculated with PHREEQC v.3.0 for the carbonation of $Ca(OH)_2$ under different temperatures, CO_2 partial pressures and resulting solid phases.

	Final pH - PHREEQC simulations at 20°C (initial pH=12.56)			
p_{CO2} /atm	Monohydrocalcite	Vaterite	Aragonite	Calcite
0.750	6.389	6.317	6.139	6.087
0.167	6.805	6.734	6.559	6.508
0.039	7.215	7.154	6.972	6.921

	Final pH - PHREEQC simulations at 23°C (initial pH=12.45)			
p_{CO2} /atm	Monohydrocalcite	Vaterite	Aragonite	Calcite
0.750	6.338	6.310	6.135	6.083
0.167	6.805	6.728	6.555	6.504
0.039	7.214	7.139	6.968	6.917

	Final pH - PHREEQC simulations at 25°C (initial pH=12.37)			
p_{CO2} /atm	Monohydrocalcite	Vaterite	Aragonite	Calcite
0.750	6.388	6.306	6.132	6.08
0.167	6.805	6.724	6.553	6.501
0.039	7.214	7.135	6.966	6.915

5.4. The neutralization of $Ca(OH)_2$

Figure 5.1 shows the potential transient recorded during the carbonation of a thin layer of solution using a partial pressure of CO_2 of 0.167 atm. The figure shows the chronopotentiogram since the beginning of the experiment, just after the palladium electrode was loaded with hydrogen, until the β phase of the palladium hydride was produced.

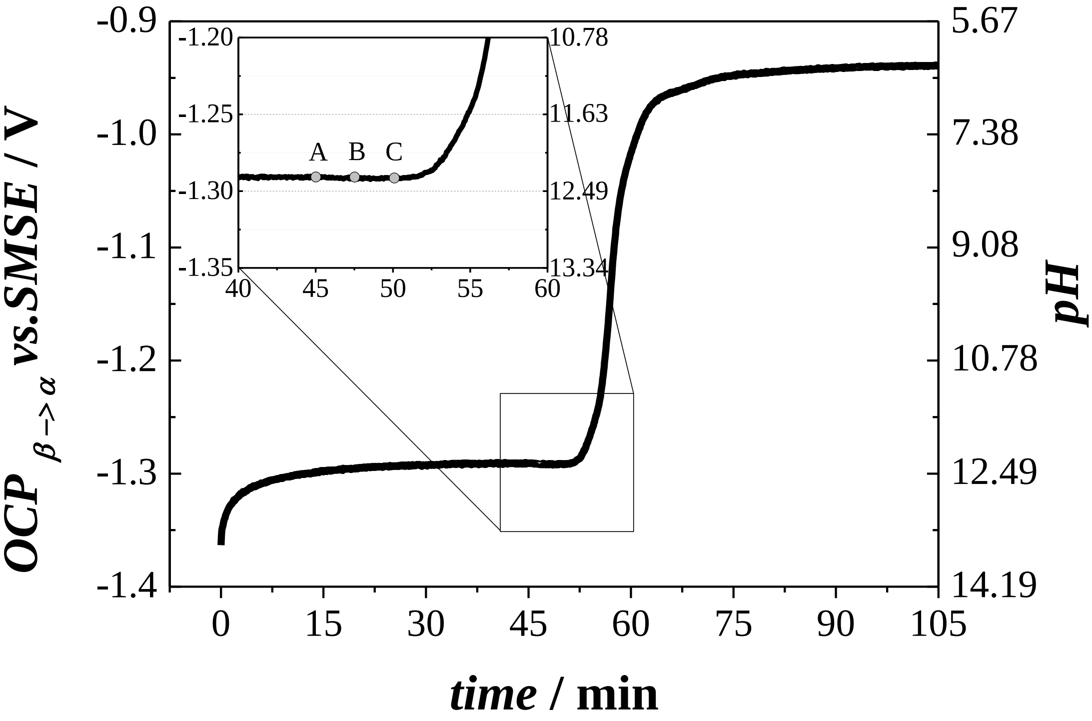

Figure 5.1 Potential transient recorded during the carbonation of a thin layer of solution. The pH axis was calculated from the open circuit potential axis on the left and the calibration curve shown in **Figure 3.5**. The insert shows the same data with A, B and C respectively indicating when the working electrode touched the surface of the porous medium, the removal of the solution and the insertion of the CO_2 in the gas stream. The Pd nanostructured film was electrodeposited (Q_{dep} = 4 C cm^{-2}) onto a 250 µm diameter Pt electrode.

The beginning of the chronopotentiogram shows a rise in potential that corresponds to the transition of the palladium hydride from its β phase ($t < t_1$ in **Figure 3.4**) to the α+β phase. The time in which the electrode was in its β phase is about 30 min. When the palladium hydride reached the α+β phase ($t_2 < t < t_1$ in **Figure 3.4**); the electrode started to work as a pH sensor. During this time wet Ar was blown inside the cell above the solution and, consequently, the solution was in equilibrium with a stable pH defined by the concentration of lime. At the time A, 45 min after the beginning of the experiment, the electrode was moved down to get in contact with the tissue paper and a few minutes later, at time B (about 47 min), the solution was removed from the cell, **Figure 2.3**, in order to obtain a thin layer of solution trapped in the mesh where the pH change was studied. Data recorded show that during this procedure the signal was very stable and that there were no variations in the potential between point A and B, hence the solution trapped in the mesh has the same pH as the bulk solution and the microelectrode is not affected by the removal of the solution above the mesh.

The potential measured from the beginning until the point C of the test corresponds to the pH of the saturated solution of pure $Ca(OH)_2$ as measured by the PdH microelectrode. According to the calibration curve shown in **Figure 3.5**, the pH is 12.45 ($OCP_{\beta\rightarrow\alpha}$ = -1.295 V). This value is quite different from the pH measured with the glass pH meter during the preparation of solution (12.7) but is in perfect agreement with the results of the PHREEQC calculation (12.45; **Table 5.1**). After 50 min from the beginning of the experiment, at the time C, wet $CO_{2(g)}$ was introduced in the gas mixture and blown inside the cell. The inset in **Figure 5.1** shows that a few seconds after CO_2 was introduced, the potential began to rise (and the pH to decrease) until it reached a second plateau. This plateau was due to the stabilization of solution due to the complete consumption of the Ca^{2+} ions by the carbonation reaction as described by the following equation:

$$Ca^{2+}(aq) + CO_3^{2-}(aq) + H_2O(l) \rightleftharpoons CaCO_3(s) + H_2O(l) \quad (39)$$

The reaction between calcium and carbonate ions, in fact, promotes the dissociation of bicarbonate ion and carbonic acid that, in turn, promotes the dissolution of more $CO_{2(g)}$ and the release of protons that neutralize the solution, according to the following equations:

$$CO_2(gas) \rightleftharpoons CO_2(aq) \quad (40)$$

$$CO_2(aq) + H_2O(l) \rightleftharpoons H_2CO_3(aq) \quad (41)$$

$$HCO_3^-(aq) \rightleftharpoons CO_3^{2-}(aq) + H^+(aq) \quad (42)$$

$$CO_3^{2-}(aq) + Ca^{2+}(aq) \rightleftharpoons CaCO_3(s) \quad (43)$$

Once all Ca^{2+} are consumed, the concentrations of all species in the carbonic acid system reach an equilibrium that depends on the partial pressure of CO_2 in the atmosphere surrounding the film of water and on the solid phases produced by carbonation (e.g. calcite or vaterite).

Table 5.2 Experimental pH values recorded at the end of the carbonation of $Ca(OH)_2$ at different p_{CO2} and 23°C

	Final pH - experimental results at 23°C (initial pH=12.45)				
p_{CO2} /atm	1st test	2nd test	3rd test	average	St. Err.
0.750	6.13	6.06	6.17	6.12	0.03
0.167	6.34	6.56	6.47	6.46	0.06
0.039	6.95	6.78	6.85	6.86	0.05

In **Figure 5.1** the second plateau is clearly seen after 90 min from the beginning of the experiment. The pH value corresponding to this plateau is 6.34 (**Table 5.2**). The theoretical pH of a similar system as calculated by PHREEQC assuming formation of calcite is 6.50 (**Table 5.1**). Repetitions of the same test (**Table 5.2**) lead to a mean experimental value of 6.46 ± 0.06. The difference between this mean and the theoretical value is -0.04 pH.

Formation of calcite (mainly) and vaterite (traces) during the experiment is proved by SEM images (**Figure 5.2**) and by XRD data (**Figure 5.3**). The products of the carbonation shown in **Figure 5.2** were obtained after preliminary tests without the gas line shown in **Figure 2.3**. Before the use of the cylinder, some carbonation tests were recorded with CO_2 produced by the sublimation of cardice (solid pellets of frozen CO_2). These experiments were then discarded because of the impossibility to control accurately the sublimation rate and therefore the flux of carbon dioxide introduced into the cell. For these reasons, it was preferred to introduce CO_2 using a gas cylinder and two flow meters. Nevertheless, this picture is important because it shows that without a complete control of the parameters, both phases can nucleate.

With the use of the gas line, tests were carried out with a p_{CO2} of 0.039, 0.167 and 0.750 atm. Results are reported in **Table 5.2** and **Figure 5.4**.

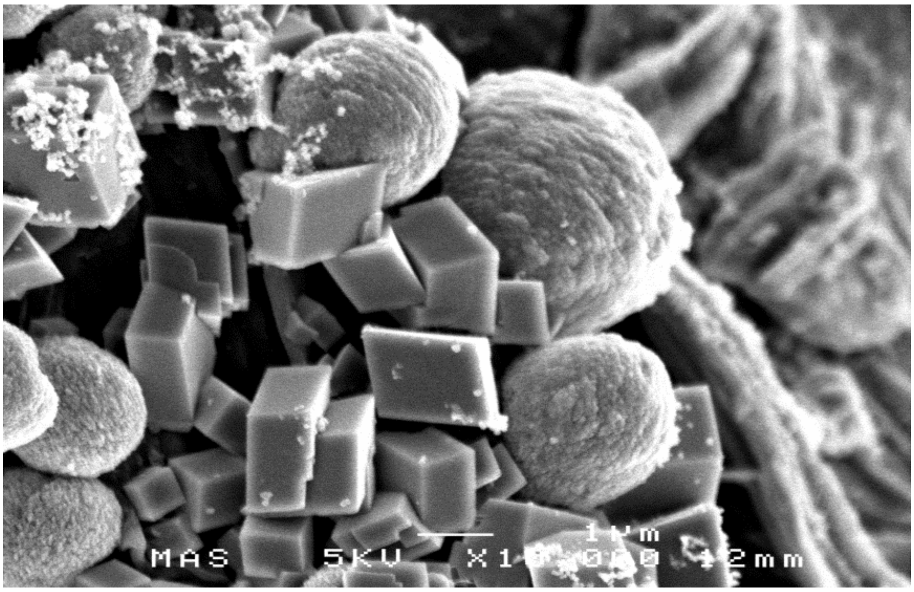

Figure 5.2 FE-SEM images of the cellulose mesh sample with calcite crystals (rhombohedral) and vaterite crystals (spherulites). The sample was previously coated with chromium to avoid charging in the SEM chamber. In this experiment, the carbonation was induced by the sublimation of cardice (solid pellets of CO_2).

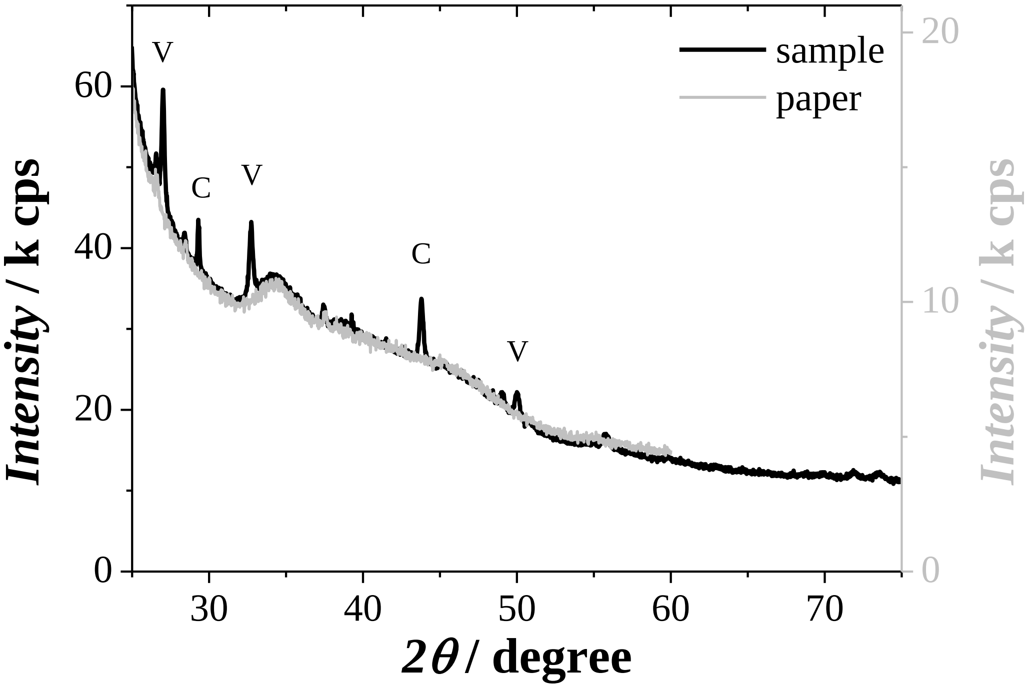

Figure 5.3 Typical diffractograms recorded on the cellulose substrate before (grey) and after (black) carbonation. The peaks confirm the presence of calcite (C) and vaterite (V) crystals on the fibres of the cellulose.

Figure 5.4 shows the calculated equilibrium pH of solutions containing calcite and vaterite, at different p_{CO2} (empty symbols). Results show a decrease in pH with the increase of p_{CO2}. The same plot allows a comparison between the theoretical values and the experimental results (black symbol). Experiments at different p_{CO2} were repeated three times and the mean was plotted together with the related standard error. In almost all cases SEM analysis demonstrated formation of calcite as major solid phase produced by the carbonation (**Figure 5.7**). In only one case both the pH value (**Figure 5.5**) and the SEM image (**Figure 5.6**) suggested the formation of only vaterite. We surmise the crystallization of almost pure vaterite was related to the reaction kinetic because it was obtained in an experiment where the pH variation after the introduction of CO_2 was unexpectedly fast compared with the other measurements. Comparison between the theoretical and experimental values shows that at 0.039 atm p_{CO2} the difference is 0.06 points of pH and at 0.750 atm p_{CO2} the difference is about 0.04. This means that all the pH values determined from the microelectrode potentials are in very good agreement with the theoretical values calculated with PHREEQC.

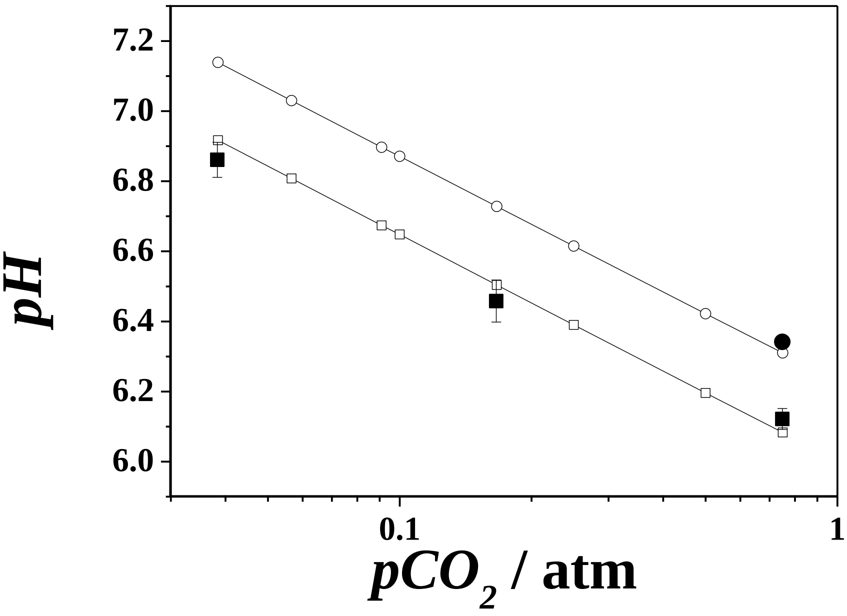

Figure 5.4 Dependence of pH on the p_{CO2}. Theoretical (□) and experimental (■) results for calcite and theoretical (○) and experimental (●) results for vaterite.

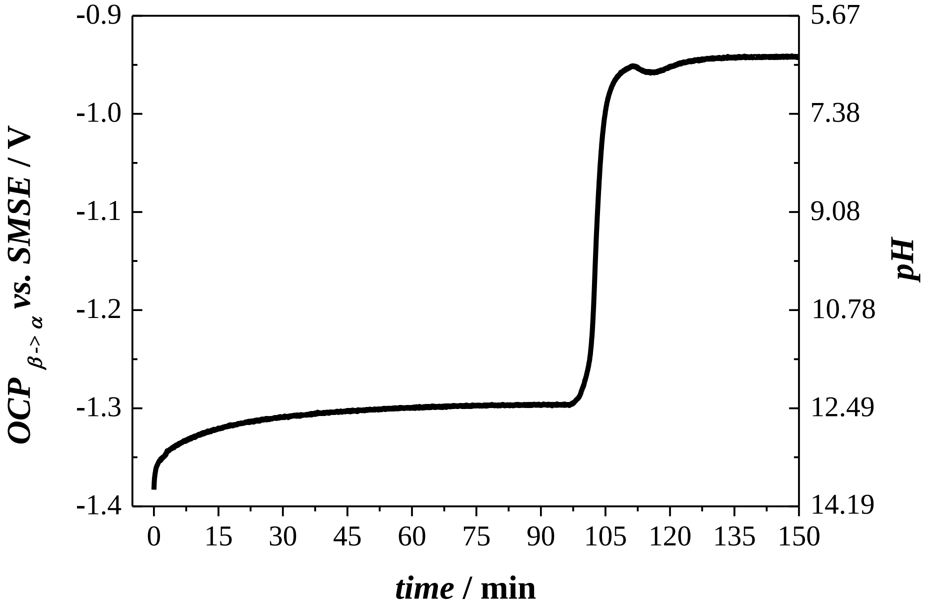

Figure 5.5 Potential transient recorded during the carbonation of vaterite. The pH axis was calculated from the open circuit potential axis on the left and the calibration curve shown in **Figure 3.5**

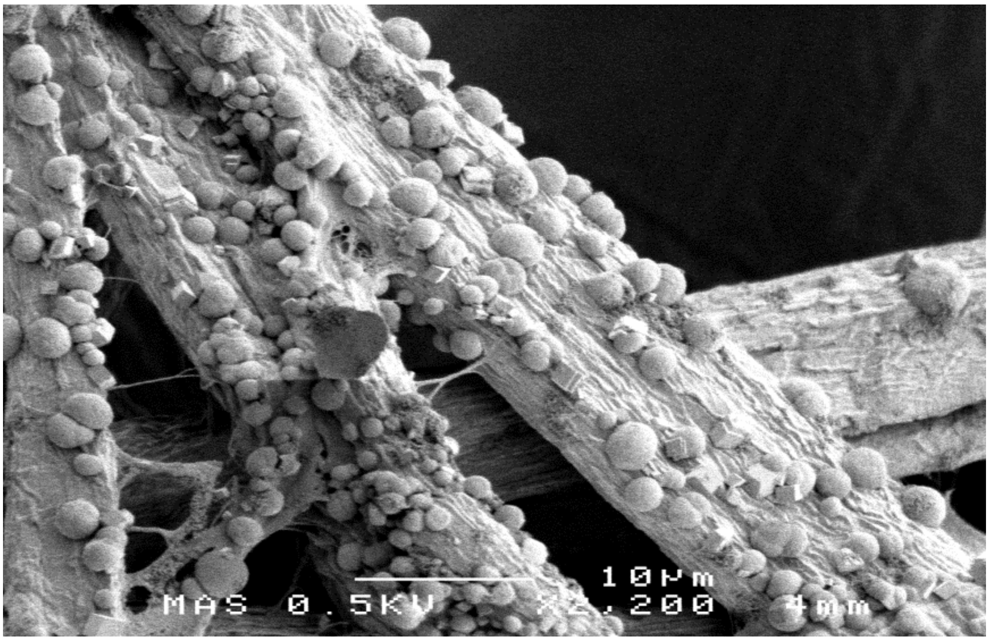

Figure 5.6 FE-SEM images of the cellulose fibres with prevalent vaterite formations.

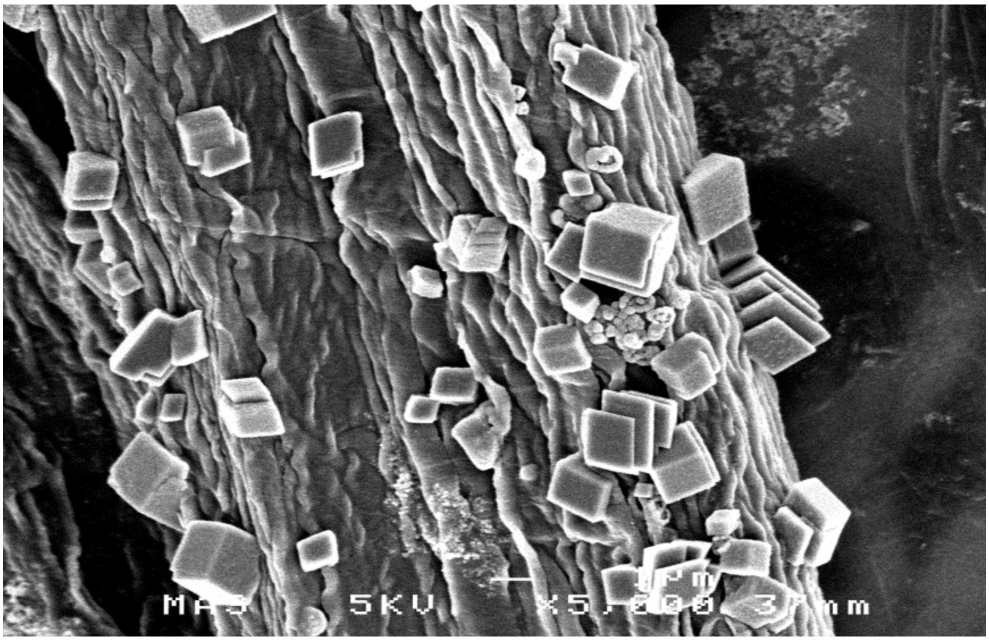

Figure 5.7 FE-SEM images of the cellulose fibres with prevalent calcite crystals.

To check the stability of the potentiometric response the electrode potential was monitored continuously over 24 hr. At regular intervals (typically 4 hr) the Pd nanostructure was galvanostatically reloaded with hydrogen (I = -12.2 μA cm^{-2} for 2 min for a 250 μm diameter electrode) until a H/Pd ratio circa 0.6 corresponding to the beginning of the β PdH phase. A new chronopotentiogram was recorded after each reloading sequence. In all cases the plateau potential was found to be reproducible throughout the 24 hr test.

5.5. Summary

Potentiometric pH microprobes made with nanostructured palladium hydride microelectrodes were exploited to monitor pH variations resulting from a reaction confined in a porous medium. Continuous operation was demonstrated by reloading hydrogen at regular intervals to maintain the correct hydride composition thereby alleviating the need for calibration. These properties were validated by detecting pH transients during the carbonation of $Ca(OH)_2$ within a fibrous mesh. Experimental pHs recorded *in situ* were in excellent agreement with theoretical calculations for the CO_2 partial pressures considered. Results also showed that the electrodes were sufficiently sensitive to differentiate between the formation of vaterite and calcite, two polymorphs of $CaCO_3$. The methodology described is particularly suited to the detection of pH at the surface of solid and porous materials, especially reactions involving high pHs.

6. Conclusions and further work

There are no practical and reliable micro pH sensors with a wide pH range, although a number of microsensors to measure local pH have been studied. In most cases the main disadvantage is obtaining a stable and reproducible potential due to the extremely small size of microelectrodes, especially in the case of potentiometric sensors. This study has demonstrated that pH microsensors made with nanostructured palladium hydride microelectrodes could operate reliably even in very alkaline environments. Their potentiometric response was found to be Nernstian up to pH 14. To our knowledge this is the first report of a pH microelectrode operating reliably at such high pH. The pH electrode is accurate, reliable, precise and reproducible over several hours. It also has the unique property in being able to monitor pH changes over a wide range of time: at regular intervals, when the PdH returns to its α phase, the electrode can be galvanostatically reloaded with hydrogen to take it back its β phase. The potentiometric pH response during the $\alpha+\beta$ phase is rapid, stable, reproducible and almost theoretical in deaerated solutions. The H_1-e Pd hydride microelectrodes show such a reproducible potentiometric response that once calibration is performed, it is possible to conduct measurements without calibration before and after the pH measurements (procedure normally essential for potentiometric micro sensors). We successfully employed the electrodes to monitor the pH changes during the carbonation of a saturated lime solution confined in a porous substrate exposed to a partial pressure of CO_2. The pH detected in situ was found to be in perfect agreement with theoretical calculations. The electrode response proved to be sufficiently sensitive and reproducible to differentiate, on the basis of pH, between the formation of calcite and vaterite, both polymorphs of calcium carbonate, inside the substrate. We believe these nanostructured pH microelectrodes are currently the only analytical tools capable of monitoring high pH in confined places and we expect they will be highly valuable to study geochemical processes involving very alkaline waters.

However, performing experiment in presence of air, it has been noticed that the potentiometric sensor is extremely sensitive to the oxygen: the less oxygen is present in the solution, the longer is the lifetime of the pH electrode and the smaller is the potential offset with respect to the response in absence of oxygen. This feature has been observed also in standard experiments in bulk solution in presence of different concentration of the oxidant, O_2 and ruthenium hexamine (not shown), and it has been confirmed also during SECM experiments: the closer the tip is with respect to the substrate, the smaller is the flux of oxygen diffusing towards the tip and the smaller is the offset. Although the tip is held at zero current, its open circuit potential is negative enough to drive the reduction of oxygen and the quick extraction of hydrogen from the palladium lattice. The combination of these events in a process akin to localised corrosion produces the discharge of the sensor. The smaller is the flux of oxygen, the slower is the discharge and the more negative is the open circuit potential. Regarding the PdH system, our results clearly show that the presence of an oxidant capable of extracting H will significantly affect the pH measurement. The strong tip−substrate dependence makes use of such an electrode in SECM very challenging, as it becomes difficult to relate variations in tip potential to pH. This is particularly relevant when the flux of oxidant toward the tip is high as for example found with small tips or with a substrate capable of regenerating the mediator. The rotating disc electrode experiments confirmed perfectly the SECM and the bulk experiments: the higher the rotation rate, the larger the flux of oxygen at the tip and the more positive the mixed potential is. Extrapolating the potential at no rotation rate, the OCP estimated is within 3 mV of the actual potential measured in absence on any oxygen in the solution.

The observations reported here clearly demonstrate that the potentiometric mode of SECM can be more complicated than anticipated; several remarks can now be made regarding this mode: the tip is not necessarily a passive probe as normally assumed, and one should consider the possibility of redox processes occurring on its surface even when held at zero current. Redox processes may force the tip potential to differ from the expected thermodynamic value by taking a mixed potential if the tip surface is able to promote two Faradaic processes with equal and opposite rates. Furthermore, the potentiometric response can be controlled by diffusion provided one of the species involved in the Faradaic processes reacts with the tip at a diffusion-controlled rate. Under these conditions, the potentiometric approach curve becomes diffusion-controlled and akin to the traditional SECM approach curves found in the amperometric feedback mode. Overall, the tip potential becomes sensitive to the tip−substrate distance and less so to the activity of a target species, as initially intended. These effects must be added to the dependence of the tip potential on Ohmic drop when current flows between other electrodes in the cell. One should not see the above as restrictions; the ability to finely control the mixed potential by simple adjustment of the tip−substrate distance opens new opportunities for the potentiometric mode of SECM.

The potential shift in presence of a controlled amount of oxygen has been extensively studied during this PhD and it can easily be controlled now, therefore the main disadvantage at the moment is the limited lifetime of the sensor in aerated solutions because of the oxidation of sorbed hydrogen by the dissolved oxygen. In order to increase the lifetime of the sensor, three approaches can be taken: (i) the electrodeposited palladium can be protected by a proton permeable membrane (i.e. Nafion) that can slow down the diffusion of oxygen toward the tip. With this coating, both the mixed potential arising from the two independent reactions and the limited lifetime can be fixed. (ii) Another possible solution to lengthen the lifetime is recessing the Pt microdisc electrode before the H_1-e Pd film deposition. The procedure to etch Pt microdisc electrode is well known[242, 309] and it can be easily applied to this problem. In this way, it should be possible to increase the thickness of the nanostructured Pd layer without enlarging the diameter. (iii) Another possibility is to reload in situ the electrode more frequently in order to keep it in the mixed $\alpha+\beta$ phases that allow the measure of the pH. This procedure has been successfully tested with the use of the software NOVA 1.9, but it has never been applied in real experiments, as for example the recording of an SECM pH image. These approaches may lead to apply the PdH electrodes to solutions containing oxidizing species, allowing performing SECM maps in aerated conditions.

Another interesting possibility to develop is the miniaturization of the H_1-e Pd electrode. The smallest size of electrodes used in this study was 10 μm diameter; decreasing the dimension of the electrode would allow the study of more systems at higher spatial resolution. In particular biomedical studies are seeking nano pH probes that would allow measuring the pH on single parts of the human/animal cells. Variations from the neutral pH, in fact, can be due to the early stage of a disease that could be identified by just monitoring the pH of the cell. The miniaturization of the PdH electrode could also be used for pH detection on single crystallographic facets in order to determine, in the case of $Ca(OH)_2$, which is the preferential plane that is subjected to carbonation and to define if the reaction proceeds differently for different facets. Probably the best way to build these electrodes would be to electrodeposit a film of H_1-e Pd on the real tip of a capillary previously pulled with a laser and filled with pyrolytic carbon to have the metallic contact and support for the electrodeposition. Those electrodes could then be loaded with hydrogen to form the correct phase that allows the measure of the pH and be used as punctual pH sensors.

A big step forward would be to understand the entire potential transient during the carbonation reactions and to relate the different gradients to kinetics or to different steps in the carbonation reactions. The experiments in chapter 5 indicate that kinetic informations are available form the transients, but a new gas line design would be required to have a proper control of the time when CO_2 interacts with the lime solution. For the same purpose it would be nice to integrate the PdH-pH sensor with a Raman spectrometer in order to monitor the progression in the reaction by two analytical signals that could be inter-correlated. The design of the cell has to be carefully thought to acquire the spectrum and the pH with the analytical tools on the same area.

Now that the experimental methodology has been established on pure lime, another interesting field would be to measure the progression in the pH during the carbonation in more complex systems like in those in which additives are commonly used in conjunction with lime and cement to enhance some particular propriety of the mortars (i.e. in presence of blast furnace slag, bottle glass, wood ash, hemp and metakaolin). This study will be of particular interest in conjunction with strength measurements for the industry on cements.

Another interesting topic for further work is to study other mixed potential systems (like in corrosion studies) by applying the SECM methodology. For this, the tip would need to consist of the material of interest and the potentiometric response would be monitored for a range of tip−substrate distances above an inert substrate in the presence and absence of oxygen. For instance, the corrosion of a given alloy could be studied by fabricating a SECM tip from the alloy and recording its potentiometric response while approaching an inert surface in aerated solution. Alternatively, the substrate could be made from the sample of interest and the tip from an inert material. For example, the corrosion of a coated metallic surface could be investigated by approaching a submillimetre size polished glass disc toward a micrometre size pinhole, purposely made in the coating to behave as a microdisc.

Further work can also be done by applying the H_1 nanostructure to other potentiometric microsensors. It is known that the potentiometric signal gets worst with decreasing the size of the electrode, but because of their enormous surface active area, the mesoporous films are expected to have behaviour similar to macro electrodes. The work can be started considering metal/metal oxide sensors like for example Pd/PdO_x and Ir/IrO_x. By producing these H_1-e MO_x films the role of the nanostructure in achieving the good potentiometric response can be studied and analysed in details.

7. Appendix

7.1. Thermodynamic considerations on the α+β phase transition potential

In the following section, the complete derivation of the potential in the transition phase is presented on the basis of the treatment previously reported by some authors[193, 199, 203].

As for gas phase conditions, the H in the PdH is in equilibrium with H_2 in the solution, so the following chemical equilibrium is verified:

$$2\,H_{(PdH)} \rightleftharpoons H_{2\,(sol)} \tag{44}$$

therefore

$$2\,\mu_{H\,(PdH)} = \mu_{H_2\,(sol)} \tag{45}$$

$$\mu_{H\,(PdH)} = \mu^0_{H\,(PdH)} + RT\ln a_{H\,(PdH)} \tag{46}$$

$$\mu_{H\,2(sol)} = \mu^0_{H\,2(sol)} + RT\ln\frac{p_{H_2}}{p^\theta} \qquad \text{where } p^\theta = 1\,bar \tag{47}$$

hence

$$2\left(\mu^0_{H\,(PdH)} + RT\ln a_{H\,(PdH)}\right) = \mu^0_{H\,2(sol)} + RT\ln\frac{p_{H_2}}{p^\theta} \tag{48}$$

and

$$RT\ln a_{H\,(PdH)} = \frac{1}{2}\mu^0_{H_2\,(sol)} + \frac{RT}{2}\ln\frac{p_{H_2}}{p^\theta} - \mu^0_{H\,(PdH)} \tag{49}$$

In parallel with the chemical equilibrium, there is the electrochemical equilibrium following the Volmer reaction (19):

$$H^+ + e^- \rightleftharpoons H_{(PdH)} \tag{50}$$

At equilibrium, $\sum\bar{\mu}\,(reactant) = \sum\bar{\mu}\,(product)$, so

$$\bar{\mu}_{H^+\,(sol)} + \bar{\mu}_{e^-\,(PdH)} = \bar{\mu}_{H\,(PdH)} \tag{51}$$

$$\bar{\mu}_{e^-\,(PdH)} = \bar{\mu}_{H\,(PdH)} - \bar{\mu}_{H^+\,(sol)} \tag{52}$$

$$\bar{\mu}_{e^-\,(PdH)} = \mu^0_{H\,(PdH)} + RT\ln a_{H\,(PdH)} + z_H F\Phi_{(PdH)} - \left(\mu^0_{H^+(sol)} + RT\ln a_{H^+(sol)} + z_{H^+}F\Phi_{(sol)}\right) \quad (53)$$

$$\bar{\mu}_{e^-\,(PdH)} = \mu^0_{H\,(PdH)} - \mu^0_{H^+(sol)} + RT\ln\frac{a_{H\,(PdH)}}{a_{H^+(sol)}} + z_H F\Phi_{(PdH)} - z_{H^+}F\Phi_{(sol)} \quad (54)$$

Since $z_H = 0, z_{H^+} = 1$ and

$$\bar{\mu}_{e^-\,(PdH)} = \mu^0_{e^-(PdH)} + z_{e^-}F\Phi_{(PdH)} \quad (55)$$

where $z_{e^-} = -1$, substituting (55) in (54) yelds

$$\mu^0_{e^-(PdH)} - F\Phi_{(PdH)} = \mu^0_{H\,(PdH)} - \mu^0_{H^+(sol)} + RT\ln\frac{a_{H\,(PdH)}}{a_{H^+(sol)}} - F\Phi_{(sol)} \quad (56)$$

Rearranging to bring the potential terms on the left-hand side gives

$$F\left(\Phi_{(PdH)} - \Phi_{(sol)}\right) = \mu^0_{e^-(PdH)} + \mu^0_{H^+(sol)} - \mu^0_{H\,(PdH)} - RT\ln\frac{a_{H\,(PdH)}}{a_{H^+(sol)}} \quad (57)$$

$$\Phi_{(PdH)} - \Phi_{(sol)} = \frac{1}{F}\left(\mu^0_{e^-(PdH)} + \mu^0_{H^+(sol)} - \mu^0_{H\,(PdH)}\right) - \frac{RT}{F}\ln\frac{a_{H\,(PdH)}}{a_{H^+(sol)}} \quad (58)$$

$$\Phi_{(PdH)} - \Phi_{(sol)} = \frac{1}{F}\left(\mu^0_{e^-(PdH)} + \mu^0_{H^+(sol)} - \mu^0_{H\,(PdH)}\right) - \frac{RT}{F}\ln a_{H\,(PdH)} + \frac{RT}{F}\ln a_{H^+(sol)} \quad (59)$$

Substituting (49) in (59),

$$\Phi_{(PdH)} - \Phi_{(sol)} = \frac{1}{F}\left(\mu^0_{e^-(PdH)} + \mu^0_{H^+(sol)} - \mu^0_{H\,(PdH)}\right) - \frac{1}{F}\left(\frac{1}{2}\mu^0_{H_2\,(sol)} + \frac{RT}{2}\ln\frac{p_{H_2}}{p^\theta} - \mu^0_{H\,(PdH)}\right) + \frac{RT}{F}\ln a_{H^+(sol)} \quad (60)$$

$$\Phi_{(PdH)} - \Phi_{(sol)} = \frac{1}{F}\left(\mu^0_{e^-(PdH)} + \mu^0_{H^+(sol)} - \frac{1}{2}\mu^0_{H_2\,(sol)}\right) - \frac{RT}{2F}\ln\frac{p_{H_2}}{p^\theta} + \frac{RT}{F}\ln a_{H^+(sol)} \quad (61)$$

When we consider the potential against SHE, $\mu^0_{e^-(PdH)} + \mu^0_{H^+(sol)} - \frac{1}{2}\mu^0_{H_2\,(sol)} = 0$ because

$$H^+ + e^- \rightleftharpoons \frac{1}{2}H_2 \quad (62)$$

$$\bar{\mu}_{e^-(PdH)} + \bar{\mu}_{H^+(sol)} = \frac{1}{2}\bar{\mu}_{H_2\,(sol)} \tag{63}$$

$$\mu^0_{e^-(PdH)} - F\Phi_{(PdH)} + \mu^0_{H^+(sol)} + RT\ln a_{H^+_{(sol)}} + F\Phi_{(sol)} = \frac{1}{2}\left(\mu^0_{H_2\,(sol)} + RT\ln\frac{p_{H_2}}{p^0}\right) \tag{64}$$

where $a_{H^+} = 1$ and $p_{H_2} = p^0 = 1\ bar$ because it is considered at standard conditions

$$\Phi_{(sol)} - \Phi_{(PdH)} = \frac{1}{F}\left(\frac{1}{2}\mu^0_{H_2\,(sol)} - \mu^0_{H^+(sol)} - \mu^0_{e^-(PdH)}\right) \tag{65}$$

i.e. $E^0 = \frac{1}{F}\left(\frac{1}{2}\mu^0_{H_2\,(sol)} - \mu^0_{H^+(sol)} - \mu^0_{e^-(PdH)}\right)$ (66)

By definition, the standard potential for equilibrium (62) is set as 0 V, therefore $\frac{1}{2}\mu^0_{H_2\,(sol)} - \mu^0_{H^+(sol)} - \mu^0_{e^-(PdH)} = 0$.

Going back to equation (61) and replacing the left-hand side term with $E_{PdH} vs. SHE$ yelds,

$$E_{PdH} vs. SHE = -\frac{RT}{2F}\ln\frac{p_{H_2}}{p^\theta} + \frac{RT}{F}\ln a_{H^+(sol)} \tag{67}$$

Since $pH = -\log a_{H^+(sol)}$ and $\log x = \frac{\ln x}{\ln 10}$,

$$E_{PdH} vs. SHE = -\frac{RT}{2F}\ln\frac{p_{H_2}}{p^\theta} - \frac{2.303\,RT}{F}pH \tag{68}$$

From the paper of Tsuruta *et al.*[203] at 25 °C, the partial pressure of H_2 is 0.02 bar when the PdH is in transition between the β and α phases, therefore equation (63) can be rewritten as follows:

$$E_{PdH} vs. SHE = +0.050\,V - 0.0592\,V\,pH \tag{69}$$

This equation predicts that in standard conditions the potential of the PdH electrode will be +0.050 V with respect to the SHE.

7.2. Electrogeneration of the sample

Deposition of hydroxides by electrogeneration of base has been practised by electrochemists for many years [310]. A few papers have dealt with calcium carbonate formation by an electrochemical driving force and some results have been published [5, 8, 10] regarding the influence of various parameters on the kinetic growth of $CaCO_3$ crystals on an electrode[8, 11, 12]. To study the carbonation reaction[5, 15] occurring in concrete, it is necessary to monitor the processes on pure $Ca(OH)_2$. For this reason we tried the precipitation of $Ca(OH)_2$ induced by an electrochemical driving force in situ. In order to achieve high grade of purity of $Ca(OH)_2$, the nucleation of portlandite crystals in the same electrochemical cell in which the carbonation would later be studied was performed. The shift to basic pH can be obtained by imposing a cathodic reduction on the electrode. The deposition of metal hydroxides has been achieved by different authors by electrogenerating hydroxyl ions to form films directly on the cathodic substrate. Different species for producing hydroxyl anions were proposed in the literature like oxygen[311], water, hydrogen peroxide [312] and nitrate ions [313]. The reduction of all of these species allows a controlled pH value to be reached at the electrode-solution interface. Therese and Kamath [314] investigated the yields of electrodeposited hydroxides obtained from nitrate bath and compared it with that obtained from chloride bath. Since the chloride ions do not participate in any reduction reaction, the yield of hydroxide from a chloride bath should be entirely due to the HER (19). They investigated the synthesis of $Mg(OH)_2$ as a model because it is a stoichiometric compound with a well-defined structure and composition. $Ca(OH)_2$ and $Mg(OH)_2$ have both the metal cation in the s-block. The electrosynthesis of $Mg(OH)_2$ has shown that the yield of hydroxides produced is much higher from a Mg-chloride bath when compared to a Mg-nitrate bath under all deposition conditions. For this reasons, the attempt in the electrogeneration of $Ca(OH)_2$ was carried out in $CaCl_2$ solutions. The yield of the deposition has been also studied in chloride baths at a different pH. The authors have used solutions at pH between 1 and 7. The yield of the reaction reaches a maximum value for $pH > 3$ [314]. The homogeneous nucleation of $Ca(OH)_2$ occurs, under thermodynamic conditions, at pH around 12.8[315]. Water reduction produces OH^- and H_2 simultaneously, so the resulting gas bubbles on a substrate may be not appropriate for precipitate formations. Nobial *et al.* [313] considered the addition of nitrate ions to be a good way to increase the local pH, but the role of nitrate ions and the nature of the reduction products is almost unsolved, since nitrate ion reduction is very complex and involves different mechanisms with a large number of stable intermediates.

For these reasons, we tried to generate calcium hydroxide crystals above the surface of platinum and gold electrodes. The generation of the base by cathodic reduction was performed at the cathode of a divided cell in order to separate the products of the cathodic reaction from those of the anodic reaction. The reference electrode used was a homemade calomel electrode (250 mV *vs*. SHE). The anode was a conventional platinum grid immersed in a solution of 0.1 M KCl. The cathode was the working electrode immersed in a solution of 1 M $CaCl_2$ saturated with oxygen at a pH close to 12 in order to facilitate the reaction. The two solutions were separated by a frit. The solutions used during the experiments related to the electrogeneration of the hydroxides were CO_2 free with the intention not to precipitate calcium carbonate. Before the preparation of the solutions, water was boiled for 20 minutes, the flask was closed and when the water was cooled down at room temperature, it was used for the preparation of the solution. To avoid the diffusion of air in the flask, pure oxygen was bubbled until the compounds had dissolved. The bubbling helped also the homogenization of the solution.

The electrosynthesis has several features which distinguish it from other synthetic methods: (i) it takes place close to the electrode within the electric double layer, which has a very high potential gradient of order of 10^5 mV cm^{-1} [314], (ii) the product is deposited on the electrode in the form of a thin film or a coating, (iii) the synthesis can be performed at low temperature, (iv) the kinetic control can be exercised by controlling the current passed through the cell, and (v) thermodynamic control can be exercised by choosing the applied cell potential. However, being an ambient temperature technique, electrosynthesis may lead to poorly ordered products making an unequivocal structural characterization difficult. For this reason, XRD measurements are prohibitive because of the amorphous impurities. In the design of the electrochemical synthesis, either the potentiostatic and galvanostatic synthesis have been tried:

- Potentiostatic synthesis. In the potentiostatic synthesis, the electrode is polarized to a desired potential with respect to the counter electrode. The cell current usually decays rapidly as the reaction proceeds due to low rates of diffusion of the molecules of oxygen from the bulk to the electrode surface. This method allows the generation of selected single-phase products by the use of the potential applied.

- Galvanostatic synthesis. The galvanostatic synthesis allows having the control over the rate of the reaction leading to deposits with good adhesion and a controlled morphology. The potential of the cell drifts as the reactant activity decreases. This may lead to a multiplicity of products.

Figure 7.1 shows pictures of deposits obtained by the use of the potentiostatic synthesis on a platinum electrode, on the left, and by using a galvanostatic control on a gold electrode, on the right. The pictures presented are those in which the experimental conditions allowed to produce the largest quantity of deposited particles with a correct chemistry. The experimental conditions are reported in the caption. It needs to be stressed that in both these experiments, the particles with the observed habit were measured for their elemental composition with the EDX detector. In those, and in other experiments not reported, the spectrum always reported peaks due to the presence of carbon. Quantitative EDX could not be performed because both the absence of standards of $Ca(OH)_2$ and $CaCO_2$ and the theoretical efficiency of the semiconducting detector for energy lower than 1 keV.

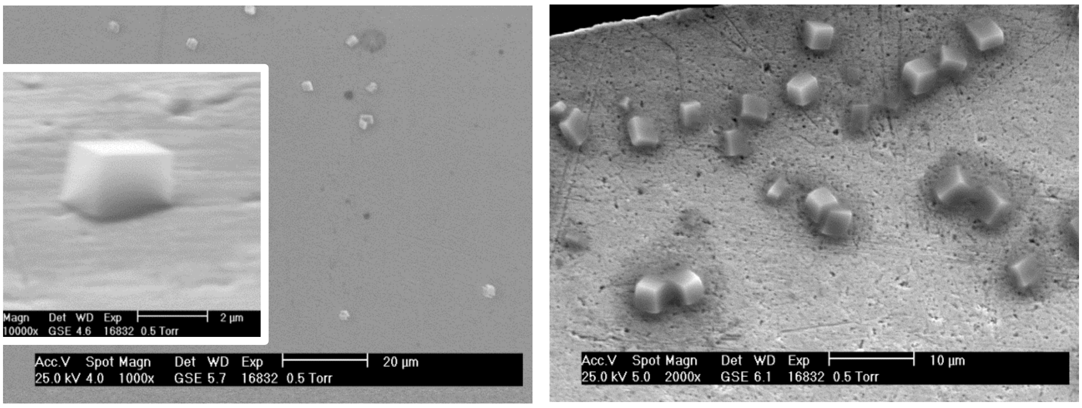

Figure 7.1 ESEM –SEI images of electrogenerated $Ca(OH)_2$ deposited on noble metal surfaces by cathodic reduction. (left) Platinum support, $R_f = 3.8$[280]. The potential was held at $E = -0.4$ V *vs.* SCE for 4 h. (right) Gold support, $R_f = 3.2$[316]. The current density was held at $j = -124$ µA cm^{-2} for 1 h.

After the experiments, the samples were washed with water to remove the electrolyte and then dried in the oven. Even if the materials and the transportation to the SEM chamber were done carefully, the presence of carbon suggests that some carbonation occurred. This may be due to a reorganization of the compound in the low vacuum chamber (0.5 torr) during a local heating of the sample because of the interaction with the electron beam that can provide a dehydration of the specimen and lead to a particular crystal habit of the $CaCO_3$ for these experimental conditions. The presence of a metallic polycrystalline substrate, the low amount of sample produced and the room temperature synthesis are limiting the number of structural analysis techniques to assess which kind of material has been deposited in these set of experiments.

It was therefore expected that the chloride bath would yield calcium hydroxide deposits, however these experiments failed, probably due to the instability of this compound. The production of hydroxyl ions is not the sole determining criterion for the success of this class of reactions. Other factors may also play a crucial role, like kinetic, experimental (shape and distance of the CE) and stability factor of the produced compound (affinity with CO_2).

7.3. Nova 1.9 procedures

7.3.1. Potentiostatic electrodeposition of nanostructured Pd from a template

This procedure allows electrodepositing the palladium metal on the surface of another metallic electrode. If the underneath electrode is a 25 μm diameter platinum microelectrode, in order to electrodeposit 4 C cm^{-2} of palladium, the charge of -19.625×10^{-6} C needs to be passed. To be sure that only the desired amounts of moles of Pd are deposited a cut off needs to be programmed.

```
> Nested procedure
     > Timed procedure
          > Autolab control
               WE(1) Mode Potentiostatic
               WE(1) High stability
               WE(1) Current range 1 μA
               Integrator (1). Integration time 1 s
          > Set potential 0.400 V
          > Set cell ON
          > Wait time 1 s
          > Record signal (> 1 ms)
               Duration (s) 5
               Interval time (s) 0.01
               Estimated number of points 500
               Signal sampler Time, WE(1) Potential, WE(1)
Current, WE(1) Charge
               > Options
                    Automatic current ranging ON
               Corrected time <array> (s)
               Time <array> (s)
```

```
     WE(1) Potential <array> (V)
     WE(1) Current <array> (A)
     WE(1) Charge <array> (C)
     Index <array>
     > E vs t
          X Time (s)
          Y WE(1) Potential (V)
          Z WE(1) Potential (V)
          Show during measurement Yes
          Measurement plot number 1
     > i vs t
          X Time (s)
          Y WE(1) Current (A)
          Z WE(1) Current (A)
          Show during measurement Yes
          Measurement plot number 2
     > Q vs t
          X Time (s)
          Y WE(1) Charge (C)
          Z WE(1) Charge (C)
          Show during measurement Yes
          Measurement plot number 3
> Autolab control
     WE(1) Bandwidth High stability
     WE(1) Current range 1 µA
> Set potential 0.100 V
> Record signals (>1 ms)
     Duration (s) 10000
     Interval time (s) 0.2
     Estimated number of points 50000
```

```
               Signal sampler Time, WE(1) Potential, WE(1)
Current, WE(1) Charge

               > Options

                    Automatic current ranging ON

                    Cutoff on WE(1) Charge when value < -
1.9625E-5 stop complete procedure. Number of detection 1.

               Corrected time <array> (s)

               Time <array> (s)

               WE(1) Potential <array> (V)

               WE(1) Current <array> (A)

               WE(1) Charge <array> (C)

               Index <array>

               > E vs t

                    X Time (s)

                    Y WE(1) Potential (V)

                    Z WE(1) Potential (V)

                    Show during measurement Yes

                    Measurement plot number 1

               > i vs t

                    X Time (s)

                    Y WE(1) Current (A)

                    Z WE(1) Current (A)

                    Show during measurement Yes

                    Measurement plot number 2

               > Q vs t

                    X Time (s)

                    Y WE(1) Charge (C)

                    Z WE(1) Charge (C)

                    Show during measurement Yes

                    Measurement plot number 3
```

```
        > Set cell OFF
```

7.3.2. Galvanostatic loading and OCP determination

This procedure allows intercalating the hydrogen in the metallic bulk of the palladium galvanostatically (by fixing a current) and then measuring the potential at open circuit when the cell is open. It was chosen to select the cell off instead of measuring at no current flowing (galvanostatically i = 0 nA) because there is actually a small current into the circuit that when the cell is off is of order of pA and when i = 0 nA is imposet it is order of ten pA.

```
> Nested procedure
    > Timed procedure
        > Autolab control
            WE(1) Mode Galvanostatic
            WE(1) High stability
            WE(1) Current range 100 nA
        > Set current 0 nA
        > Set cell ON
        > Wait time 1 s
        > Record signal (> 1 ms) galvanostatic
            Duration (s) 10 s
            Interval time (s) 0.5
            Estimated number of points 20
            Signal sampler Time, WE(1) Potential, WE(2) Current
            Options 0 Options
            Corrected time <array> (s)
            Time <array> (s)
            WE(1) Potential <array> (V)
            WE(1) Current <array> (A)
            Index <array>
            > E vs t
```

```
                    X Time (s)
                    Y WE(1) Potential (V)
                    Z WE(1) Potential (V)
                    Show during measurement Yes
                    Measurement plot number 1
               > i vs t
                    X Time (s)
                    Y WE(1) Current (A)
                    Z WE(1) Current (A)
                    Show during measurement Yes
                    Measurement plot number 2
          >Set current -8.0E-08
          >Record signal (> 1 ms) galvanostatic
               Duration (s) 100
               Interval time (s) 0.1
               Estimated number of points 1000
               Signal sampler Time, WE(1) Potential, WE(1)
Current
               Options 0 Options
               Corrected time <array> (s)
               Time <array> (s)
               WE(1) Potential <array> (V)
               WE(1) Current <array> (A)
               Index <array>
               > E vs t
                    X Time (s)
                    Y WE(1) Potential (V)
                    Z WE(1) Potential (V)
                    Show during measurement Yes
                    Measurement plot number 1
```

```
               > i vs t
                    X Time (s)
                    Y WE(1) Current (A)
                    Z WE(1) Current (A)
                    Show during measurement Yes
                    Measurement plot number 2
          > Autolab control
               WE(1) Mode Potentiostatic
               WE(1) Bandwidth High stability
               WE(1) Current range 10 nA
          > Set cell OFF
          > Record signal (> 1 ms)
               Duration (s) 40000
               Interval time (s) 4
               Estimated number of points 10000
               Signal sampler Time, WE(1) Potential, WE(1) Current
               Options
               Corrected time <array> (s)
               Time <array> (s)
               WE(1) Potential <array> (V)
               WE(1) Current <array> (A)
               Index <array>
               > E vs t
                    X Time (s)
                    Y WE(1) Potential (V)
                    Z WE(1) Potential (V)
                    Show during measurement Yes
                    Measurement plot number 4
               > i vs t
```

```
                X Time (s)
                Y WE(1) Current (A)
                Z WE(1) Current (A)
                Show during measurement Yes
                Measurement plot number 2
```

7.3.3. Galvanostatic loading, OCP determination and hydrogen stripping

```
> Nested procedure “Galvanostatic loading and OCP determination”
    > LSV to have Q_H
        > Autolab control
            WE(1) Potentiostatic
            WE(1) Bandwidth High stability
            WE(1) Current range 1 µA
        > OCP determination
            Maximum time (s) 4
            dE/dt limit 1E-6
            Use average OCP No
            OCP value -1.000
            Time <array> (s)
            WE(1) Potential <array> (V)
        > Set cel ON
        > LSV staircase
            Start potential (V) -1.000
            Stop potential (V) -0.100
            Step potential (V) 0.00024
            Scan rate (V/s) 0.1000
            Estimated number of point 2961
            Interval time (s) 0.002400
            Signal sampler Time, WE(1) Potential, WE(1)
Current
```

```
     > Options 1 Option
          Automatic current ranging ON
     Potential applied <array> (V)
     Time <array> (s)
     WE(1) Current <array> (A)
     WE(1) Potential <array> (V)
     Index <array>
> i vs E
     X Potential applied (V)
     Y WE(1) Current (A)
     Z <empty>
     Show during measurements Yes
     Measurements plot 3
> Set cell OFF
```

8. References

1. Bates, R. G., *Determination of pH. Theory and practice.* John Wiley and Sons: New York, 1964.
2. Deslouis, C.; Gabrielli, C.; Keddam, M.; Khalil, A.; Rosset, R.; Tribollet, B.; Zidoune, M., Impedance techniques at partially blocked electrodes by scale deposition. *Electrochimica Acta* 1997, 42, 1219-1233.
3. Gabrielli, C.; Keddam, M.; Khalil, A.; Rosset, R.; Zidoune, M., Study of calcium carbonate scales by electrochemical impedance spectroscopy. *Electrochimica Acta* 1997, 42, 1207-1218.
4. Gabrielli, C.; Keddam, M.; Khalil, A.; Maurin, G.; Perrot, H.; Rosset, R.; Zidoune, M., Quartz crystal microbalance investigation of electrochemical calcium carbonate scaling. *J. Electrochem. Soc.* 1998, 145, 2386-2396.
5. Gabrielli, C.; Maurin, G.; Poindessous, G.; Rosset, R., Nucleation and growth of calcium carbonate by an electrochemical scaling process. *Journal of Crystal Growth* 1999, 200, 236-250.
6. Gabrielli, C.; Jaouhari, R.; Joiret, S.; Maurin, G., In situ Raman spectroscopy applied to electrochemical scaling. Determination of the structure of vaterite. *Journal of Raman Spectroscopy* 2000, 31, 497-501.
7. Tlili, M. M.; Ben Amor, M.; Gabrielli, C.; Joiret, S.; Maurin, G.; Rousseau, P., Characterization of CaCO3 hydrates by micro-Raman spectroscopy. *Journal of Raman Spectroscopy* 2002, 33, 10-16.
8. Tlili, M. M.; Ben Amor, M.; Gabrielli, C.; Joiret, S.; Maurin, G.; Rousseau, P., Study of electrochemical deposition of CaCO3 by in situ Raman spectroscopy - II. Influence of the solution composition. *J. Electrochem. Soc.* 2003, 150, C485-C493.
9. Tlili, M. M.; Benamor, M.; Gabrielli, C.; Perrot, H.; Tribollet, B., Influence of the interfacial pH on electrochemical CaCO3 precipitation. *J. Electrochem. Soc.* 2003, 150, C765-C771.
10. Gabrielli, C.; Jaouhari, R.; Joiret, S.; Maurin, G.; Rousseau, P., Study of the electrochemical deposition of CaCO3 by in situ Raman spectroscopy - I. Influence of the substrate. *J. Electrochem. Soc.* 2003, 150, C478-C484.
11. Devos, O.; Gabrielli, C.; Tribollet, B., Nucleation-growth process of scale electrodeposition - Influence of the mass transport. *Electrochimica Acta* 2006, 52, 285-291.
12. Devos, O.; Jakab, S.; Gabrielli, C.; Joiret, S.; Tribollet, B.; Picart, S., Nucleation-growth process of scale electrodeposition - influence of the magnesium ions. *Journal of Crystal Growth* 2009, 311, 4334-4342.
13. McPolin, D. O.; Basheer, P. A. M.; Long, A. E.; Grattan, K. T. V.; Sun, T., New test method to obtain pH profiles due to carbonation of concretes containing supplementary cementitious materials. *Journal of materials in civil engineering* 2007, 19, 936-946.
14. Lawrence, R. M. H.; Mays, T. J.; Walker, P.; D'Ayala, D., Determination of carbonation profiles in non-hydraulic lime mortars using thermogravimetric analysis. *Thermochimica Acta* 2006, 444, 179-189.
15. Meier, S. A.; Peter, M. A.; Muntean, A.; Bohm, M., Dynamics of the internal reaction layer arising during carbonation of concrete. *Chemical Engineering Science* 2007, 62, 1125-1137.
16. Deslouis, C.; Frateur, I.; Maurin, G.; Tribollet, B., Interfacial pH measurement during the reduction of dissolved oxygen in a submerged impinging jet cell. *Journal of applied electrochemistry* 1997, 27, 482-492.

17. Matsushita, I.; Suzuki, T.; Moriga, T.; Ashida, T.; Nakabayashi, I.; Metson, J., XPS study on the carbonation process of Ca(OH) 2. *Journal of the Ceramic Society of Japan* 1993, 101, 725-727.

18. Lawrence, R. M. H.; Mays, T. J.; Walker, P.; D'Ayala, D., The use of TG to measure different concentrations of lime in non-hydraulic lime mortars. *Journal of Thermal Analysis and Calorimetry* 2006, 85, 377-382.

19. Balen, K. V., Carbonation reaction of lime, kinetics at ambient temperature. *Cement and Concrete Research* 2005, 35, 11.

20. Wild, S.; Khatib, J. M., Portlandite consumption in metakaolin cement pastes and mortars. *Cement and Concrete Research* 1997, 27, 137-146.

21. Moorehead, D. R., Cementation by the carbonation of hydrated lime. *Cement and Concrete Research* 1986, 16, 700-708.

22. Johannesson, B.; Utgenannt, P., Microstructural changes caused by carbonation of cement mortar. *Cement and Concrete Research* 2001, 31, 925-931.

23. Radonjic, M.; Hallam, K. R.; Allen, G. C.; Hayward, R., Mechanism of carbonation in lime-based materials. *Journal of the Building Limes Forum* 2001, 8, 50-64.

24. Beruto, D. T.; Barberis, F.; Botter, R., Calcium carbonate binding mechanisms in the setting of calcium and calcium-magnesium putty-limes. *Journal of Cultural Heritage* 2005, 6, 253-260.

25. Adams, J.; Dollimore, D.; Griffiths, D. L., Thermal analytical investigation of unaltered Ca(OH)(2) in dated mortars and plasters. *Thermochimica Acta* 1998, 324, 67-76.

26. Cultrone, G.; Sebastian, E.; Huertas, M. O., Forced and natural carbonation of lime-based mortars with and without additives: Mineralogical and textural changes. *Cement and Concrete Research* 2005, 35, 2278-2289.

27. Dheilly, R. M.; Tudo, J.; Sebai, Y.; Queneudec, M., Influence of storage conditions on the carbonation of powdered Ca(OH)(2). *Construction and Building Materials* 2002, 16, 155-161.

28. Van Balen, K., Carbonation reaction of lime, kinetics at ambient temperature. *Cement and Concrete Research* 2005, 35, 647-657.

29. Swenson, E. G.; Sereda, P. J., Mechanism of the carbonatation shrinkage of lime and hydrated cement. *Journal of Applied Chemistry* 1968, 18, 111-117.

30. Atzeni, C.; Farci, A.; Floris, D.; Meloni, P., Effect of aging on rheological properties of lime putty. *Journal of the American Ceramic Society* 2004, 87, 1764-1766.

31. Cazalla, O.; Rodriguez-Navarro, C.; Sebastian, E.; Cultrone, G.; De la Torre, M. J., Aging of lime putty: Effects on traditional lime mortar carbonation. *Journal of the American Ceramic Society* 2000, 83, 1070-1076.

32. Parrott, L. J., Durability of building materials and components. In *Assessing carbonation in concrete structures*, Spon, E. F. N., Ed. E. & F.N. Spon: London, 1990; pp 575-586.

33. Dewaele, P. J.; Reardon, E. J.; Dayal, R., Permeability and porosity changes associated with cement grout carbonation. *Cement and Concrete Research* 1991, 21, 441-454.

34. Lo, Y.; Lee, H. M., Curing effects on carbonation of concrete using a phenolphthalein indicator and Fourier-transform infrared spectroscopy. *Building and Environment* 2002, 37, 507-514.

35. Houst, Y. F.; Wittmann, F. H., Influence of porosity and water content on the diffusivity of CO2 and O2 through hydrated cement paste. *Cement and Concrete Research* 1994, 24, 1165-1176.

36. Lanas, J.; Alvarez, J. I., Masonry repair lime-based mortars: Factors affecting the mechanical behavior. *Cement and Concrete Research* 2003, 33, 1867-1876.

37. Vicat, L. J., *Mortars and cements. Reprint of the 1837 edn. translated by J.T.SMITH*. Donhead Publishing Ltd: Shaftsbury, 1997.
38. Elert, K.; Rodriguez-Navarro, C.; Pardo, E. S.; Hansen, E.; Cazalla, O., Lime mortars for the conservation of historic buildings. *Studies in Conservation* 2002, 47, 62-75.
39. Franke, L.; Sisomphon, K., A new chemical method for analyzing free calcium hydroxide content in cementing material. *Cement and Concrete Research* 2004, 34, 1161-1165.
40. Larbi, J. A.; Bijen, J., Effects of water-cement ratio, quantity and fineness of sand on the evolution of lime in set Portland-cement systems. *Cement and Concrete Research* 1990, 20, 783-794.
41. Medici, F.; Rinaldi, G., Poly-amino-phenolic additives accelerating the carbonation of hydrated lime in mortar. *Environmental Engineering Science* 2002, 19, 271-276.
42. El-Turki, A.; Ball, R. J.; Allen, G. C., Chemical and mechanical properties of lime-based mortar materials. *Journal of the Building Limes Forum* 2006, 13, 71-87.
43. Cazalla, O.; Sebastian, E.; Cultrone, G.; Nechar, M.; Bagur, M. G., Three-way ANOVA interaction analysis and ultrasonic testing to evaluate air lime mortars used in cultural heritage conservation projects. *Cement and Concrete Research* 1999, 29, 1749-1752.
44. Earnest, C. M., The modern thermogravimetric approach to the compositional analysis of materials. In *Compositional analysis by thermogravimetry*, Material, A. S. f. T. a., Ed. American Society for Testing and Material: Philadelphia, 1988.
45. Loader, J., *Basic laser Raman spectroscopy*. Heyden: London, 1970.
46. Long, D. A., *Raman spectroscopy*. McGraw Hill: London, 1977.
47. Martinez-Ramirez, S.; Sanchez-Cortes, S.; Garcia-Ramos, J. V.; Domingo, C.; Fortes, C.; Blanco-Varela, M. T., Micro-Raman spectroscopy applied to depth profiles of carbonates formed in lime mortar. *Cement and Concrete Research* 2003, 33, 2063-2068.
48. Kontoyannis, C. G.; Vagenas, N. V., Calcium carbonate phase analysis using XRD and FT-Raman spectroscopy. *Analyst* 2000, 125, 251-255.
49. Dawson, P.; Hadfield, C. D.; Wilkinso.Gr, Polarized infrared and Raman-spectra of Mg(OH)2 and Ca(OH)2. *Journal of Physics and Chemistry of Solids* 1973, 34, 1217-1225.
50. Newman, S. P.; Clifford, S. J.; Coveney, P. V.; Gupta, V.; Blanchard, J. D.; Serafin, F.; Ben-Amotz, D.; Diamond, S., Anomalous fluorescence in near-infrared Raman spectroscopy of cementitious materials. *Cement and Concrete Research* 2005, 35, 1620-1628.
51. Middendorf, B.; Hughes, J. J.; Callebaut, K.; Baronio, G.; Papayianni, I., Investigative methods for the characterisation of historic mortars - Part 1: Mineralogical characterisation. *Materials and Structures* 2005, 38, 761-769.
52. Carlos Rodriguez-Navarro, E. H., and William S. Ginell, Calcium Hydroxide Crystal Evolution upon Aging of Lime Putty. *J. Am. Ceram. Soc.* 1998, 81.
53. Brocken, H. L. P.; Larbi, J. A.; Pel, L.; Van Der Pers, N. M., Composition of mortar as a function of distance to the brick-mortar interface: a study on the formation of cured mortar structure in masonry using NMR, PFM and XRD. *Heron* 1999, 44, 257-270.
54. Leslie, A. B.; Hughes, J. J., Binder microstructure in lime mortars: implications for the interpretation of analysis results. *Quarterly Journal of Engineering Geology and Hydrogeology* 2002, 35, 257-263.
55. Walker, D. D., The microscope and lime. *Proceedings of the IVth International Conference on Cement Microscopy* 1982, 21-48.

56. Sebaibi, Y.; Dheilly, R. M.; Queneudec, M., Study of the water-retention capacity of alime-sand mortar: Influence of the physicochemical characteristics of the lime. *Cement and Concrete Research* 2003, 33, 689-696.

57. Papayianni, I.; Stefanidou, M., The evolution of porosity in lime based mortars. *Proceeding of the 8th Euroseminar on microscopy applied to building materials 4-7 September 2001 Athens* 2001, 451-457.

58. Diamond, S.; Sahu, S.; Thaulow, N., Reaction products of densifted silica fume agglomerates in concrete. *Cement and Concrete Research* 2004, 34, 1625-1632.

59. Marinoni, N.; Pavese, A.; Foi, M.; Trombino, L., Characterisation of mortar morphology in thin sections by digital image processing. *Cement and Concrete Research* 2005, 35, 1613-1619.

60. Shirakawa, M. A.; Beech, I. B.; Tapper, R.; Cincotto, M. A.; Gambale, W., The development of a method to evaluate bioreceptivity of indoor mortar plastering to fungal growth. *International Biodeterioration & Biodegradation* 2003, 51, 83-92.

61. Meyer, K. H.; Sievers, J. F., La perméabilité des membranes I. Théorie de la perméabilité ionique. *Helvetica Chimica Acta* 1936, 19, 649-664.

62. Fetcher, E. S., A Criticism of the Teorell–Meyer–Sievers Theory of Membrane Permeability. *The Journal of Physical Chemistry* 1942, 46, 570-574.

63. Bard, A. J.; Mirkin, M. V., *Scanning Electrochemical Microscopy*. New York, 2001.

64. Hall, D. G., Ion-Selective Membrane Electrodes: A General Limiting Treatment of Interference Effects. *The Journal of Physical Chemistry* 1996, 100, 7230-7236.

65. Dole, M.; Wiener, B. Z., The Theory of the Glass Electrode. IV . Temperature Studies of the Glass Electrode Error. *J. Electrochem. Soc.* 1937, 72, 107-127.

66. Caldwell, P. C., A glass microelectrode suitable for the measurement of the intracellular pH of large cells. *The Journal of physiology* 1954, 124.

67. Caldwell, P. C., An investigation of the intracellular pH of crab muscle fibres by means of micro-glass and micro-tungsten electrodes. *The Journal of physiology* 1954, 126.

68. Haber, F.; Klemensiewicz, Z., Über elektrische Phasengrenzkräft. *Zeitschrift für Physikalische Chemie* 1909, 67, 385.

69. Maj-Zurawska, M.; Hulanicki, A., Non-glass pH Potentiometric Sensors. *Chemia Analityczna* 2009, 54, 1149-1167.

70. Buhlmann, P.; Pretsch, E.; Bakker, E., Carrier-based ion-selective electrodes and bulk optodes. 2. Ionophores for potentiometric and optical sensors. *Chemical Reviews* 1998, 98, 1593-1687.

71. Bakker, E.; Buhlmann, P.; Pretsch, E., Carrier-based ion-selective electrodes and bulk optodes. 1. General characteristics. *Chemical Reviews* 1997, 97, 3083-3132.

72. Walker, J. L., Ion specific liquid ion exchanger micorelectrodes. *Analytical Chemistry* 1971, 43, A89-&.

73. Coon, R. L.; Lai, N. C. J.; Kampine, J. P., Evaluation of a dual-function pH and pCO2 in vivo sensor. *Journal of Applied Physiology* 1976, 40, 625-629.

74. Leblanc, O. H.; Brown, J. F.; Klebe, J. F.; Niedrach, L. W.; Slusarczuk, G. M. J.; Stoddard, W. H., Polymer membrane sensors for continuous intravascular monitoring of blood pH. *Journal of Applied Physiology* 1976, 40, 644-647.

75. Erne, D.; Ammann, D.; Simon, W., Liquid membrane pH electrode based on synthetic proton carrier. *Chimia* 1979, 33, 88-90.

76. Erne, D.; Schenker, K. V.; Ammann, D.; Pretsch, E.; Simon, W., Applicability of carrier based liquid membrane pH electrode to measurements in acidic solutions. *Chimia* 1981, 35, 178-179.

77. Schulthess, P.; Shijo, Y.; Pham, H. V.; Pretsch, E.; Ammann, D.; Simon, W., A hydrogen ion-selective liquid-membrane electrode based on tri-n-dodecyamine as neutral carrier. *Analytica Chimica Acta* 1981, 131, 111-116.

78. Ammann, D.; Lanter, F.; Steiner, R. A.; Schulthess, P.; Shijo, Y.; Simon, W., Neutral carrier based hydrogen-ion selective microelectrode for extracellular and intracellular studies. *Analytical Chemistry* 1981, 53, 2267-2269.

79. Schlue, W. R.; Thomas, R. C., A dual mechanism for intracellular pH regulation by leech neurons. *Journal of Physiology-London* 1985, 364, 327-338.

80. Rawlings, J. M.; Lucas, M. L., Plastic pH electrodes for the measurements of gastrointestinal pH. *Gut* 1985, 26, 203-207.

81. Anker, P.; Ammann, D.; Simon, W., Blood-pH measurement with a solvent polymeric membrane-electrode in comparison with a glass electrode. *Mikrochimica Acta* 1983, 1, 237-242.

82. Opdycke, W. N.; Parks, S. J.; Meyerhoff, M. E., Polymer-membrane pH electrodes as internal elements for potentiometric gas-sensing systems. *Analytica Chimica Acta* 1983, 155, 11-20.

83. Ruzicka, J.; Hansen, E. H., Integrated microconduits for flow-injection analysis. *Analytica Chimica Acta* 1984, 161, 1-25.

84. Hongbo, C.; Hansen, E. H.; Ruzicka, J., Evaluation of critical parameters for measurement of pH by flow-injection analysis-determination of pH in soil extracts. *Analytica Chimica Acta* 1985, 169, 209-220.

85. Kessler, M.; Hoper, J.; Volkholz, H. J.; Sailer, D.; Demling, L., A new glucose electrode for tissue measurements. *Hepato-Gastroenterology* 1984, 31, 285-288.

86. Funck, R. J. J.; Morf, W. E.; Schulthess, P.; Ammann, D.; Simon, W., Bicarbonate-sensitive liquid membrane electrodes based on neutral carriers for hydrogen-ions. *Analytical Chemistry* 1982, 54, 423-429.

87. Trojanowicz, M.; Meyerhoff, M. E., Potentiometric pH detection in suppressed ion chromatography. *Analytical Chemistry* 1989, 61, 787-789.

88. Teltingdiaz, M.; Collison, M. E.; Meyerhoff, M. E., Simplified dual-lumen catheter design for simultaneous potentiometric monitoring of carbon-dioxide and pH. *Analytical Chemistry* 1994, 66, 576-583.

89. Oesch, U.; Brzozka, Z.; Xu, A.; Rusterholz, B.; Suter, G.; Pham Hung, V.; Welti, D.; Ammann, D.; Pretsch, E.; Simon, W., Design of neutral hydrogen ion carriers for solvent polymeric membrane electrodes of selected pH range. *Analytical Chemistry* 1986, 58, 2285-2289.

90. Ma, S. C.; Chaniotakis, N. A.; Meyerhoff, M. E., Response properties of ion-selective polymeric membrane electrodes prepared with aminated and carboxylated polyvinyl-chloride. *Analytical Chemistry* 1988, 60, 2293-2299.

91. Cosofret, V. V.; Buck, R. P.; Erdosy, M., Carboxylated poly(vinyl chloride) as substrate for ion sensors - Effects of native ion-exchange on responses. *Analytical Chemistry* 1994, 66, 3592-3599.

92. Yuan, R.; Chai, Y. Q.; Yu, R. Q., Poly(vinyl chloride) matrix membrane pH electrode based on 4,4'-bis(n,n-dialkylamino)methyl azobenzene with a wide linear pH response range. *Analyst* 1992, 117, 1891-1898.

93. Mi, Y. M.; Green, C.; Bakker, E., Polymeric membrane pH electrodes based on electrically charged ionophores. *Analytical Chemistry* 1998, 70, 5252-5258.

94. Cho, D. H.; Chung, K. C.; Park, M. Y., Hydrogen ion-selective membrane electrodes based on alkyldibenzylamines as neutral carriers. *Talanta* 1998, 47, 815-821.

95. Kuruoglu, D.; Canel, E.; Memon, S.; Yilmaz, M.; Kilic, E., Hydrogen ion-selective poly(vinyl chloride) membrane electrode based on a calix 4 arene. *Analytical Sciences* 2003, 19, 217-221.
96. Boswell, P. G.; Szijjarto, C.; Jurisch, M.; Gladysz, J. A.; Rabai, J.; Buhimann, P., Fluorophilic ionophores for potentiometric pH determinations with fluorous membranes of exceptional selectivity. *Analytical Chemistry* 2008, 80, 2084-2090.
97. Qin, Y.; Bakker, E., Quantitive bindin constants of H+ -selective chromoionophores and anion ionophores in solvent polymeric sensing membranes. *Talanta* 2002, 58, 909-918.
98. Cao, Z.; Gong, F. C.; Li, H. P.; Xiao, Z. L.; Long, S.; Zhang, L.; Peng, S. J., Approach on quantitative structure-activity relationship for design of a pH neutral carrier containing tertiary amino group. *Analytica Chimica Acta* 2007, 581, 19-26.
99. Toth, K.; Nagy, G.; Horrocks, B. R.; Bard, A. J., Investigation of silver iodide-based ion-selective membranes by scanning electrochemical microscopy. *Analytica Chimica Acta* 1993, 282, 239-246.
100. Klusmann, E.; Schultze, J. W., PH-Microscopy: technical application in phosphating solutions. *Electrochimica Acta* 2003, 48, 3325-3332.
101. Liu, B.; Cheng, W.; Rotenberg, S. A.; Mirkin, M. V., Scanning electrochemical microscopy of living cells - Part 2. Imaging redox and acid/basic reactivities. *J. Electroanal. Chem.* 2001, 500, 590-597.
102. Csoka, B.; Kovacs, B.; Nagy, G., Investigation of concentration profiles inside operating biocatalytic sensors with scanning electrochemical microscopy (SECM). *Biosensors & Bioelectronics* 2003, 18, 141-149.
103. Bobacka, J.; Ivaska, A.; Lewenstam, A., Potentiometric ion sensors. *Chemical Reviews* 2008, 108, 329-351.
104. Cattrall, R. W.; Freiser, H., Coated wire ion selective electrodes. *Analytical Chemistry* 1971, 43, 1905-&.
105. Han, W. S.; Yoo, S. J.; Kim, S. H.; Hong, T. K.; Chung, K. C., Behavior of a polypyrrole solid contact pH-selective electrode based on tertiary amine ionophores containing different alkyl chain lengths between nitrogen and a phenyl group. *Analytical Sciences* 2003, 19, 357-360.
106. Han, W. S.; Chung, K. C.; Kim, M. H.; Ko, H. B.; Lee, Y. H.; Hong, T. K., A hydrogen ion-selective poly(aniline) solid contact electrode based on dibenzylpyrenemethylamine ionophore for highly acidic solutions. *Analytical Sciences* 2004, 20, 1419-1422.
107. Lindfors, T.; Ervela, S.; Ivaska, A., Polyaniline as pH-sensitive component in plasticized PVC membranes. *J. Electroanal. Chem.* 2003, 560, 69-78.
108. Han, W. S.; Park, M. Y.; Chung, K. C.; Cho, D. H.; Hong, T. K., Enhanced electrochemical performance of poly(aniline) solid-contact pH electrodes based on alkyldibenzylamine. *Analytical Sciences* 2000, 16, 1145-1149.
109. Han, W. S.; Park, M. Y.; Cho, D. H.; Hong, T. K.; Lee, D. H.; Park, J. M.; Chung, K. C., The behavior of a poly(aniline) solid contact pH selective electrode based on N,N,N ',N '-tetrabenzylethanediamine ionophore. *Analytical Sciences* 2001, 17, 727-732.
110. Masalles, C.; Borros, S.; Vinas, C.; Teixidor, F., Simple PVC-PPy electrode for pH measurement and titrations. *Analytical and Bioanalytical Chemistry* 2002, 372, 513-518.
111. Lakard, B.; Herlem, G.; Lakard, S.; Guyetant, R.; Fahys, B., Potentiometric pH sensors based on electrodeposited polymers. *Polymer* 2005, 46, 12233-12239.

112. Lakard, B.; Segut, O.; Lakard, S.; Herlem, G.; Gharbi, T., Potentiometric miniaturized pH sensors based on polypyrrole films. *Sensors and Actuators B-Chemical* 2007, 122, 101-108.

113. Leopold, S.; Herranen, M.; Carlsson, J. O.; Nyholm, L., In situ pH measurement of the self-oscillating Cu(II)-lactate system using an electropolymerised polyaniline film as a micro pH sensor. *J. Electroanal. Chem.* 2003, 547, 45-52.

114. Zine, N.; Bausells, J.; Ivorra, A.; Aguilo, J.; Zabala, M.; Teixidor, F.; Masalles, C.; Vinas, C.; Errachid, A., Hydrogen-selective microelectrodes based on silicon needles. *Sensors and Actuators B-Chemical* 2003, 91, 76-82.

115. Liao, W. Y.; Weng, C. H.; Lee, G. B.; Chou, T. C., Development and characterization of an all-solid-state potentiometric biosensor array microfluidic device for multiple ion analysis. *Lab on a Chip* 2006, 6, 1362-1368.

116. Cosofret, V. V.; Erdosy, M.; Johnson, T. A.; Buck, R. P.; Ash, R. B.; Neuman, M. R., Microfabricated sensor arrays sensitive to pH and K+ for ionic distribution measurements in the beating heart. *Analytical Chemistry* 1995, 67, 1647-1653.

117. Maminska, R.; Wroblewski, W., Solid-state microelectrodes for flow-cell analysis based on planar back-side contact transducers. *Electroanalysis* 2006, 18, 1347-1353.

118. Bergveld, P., Thirty years of ISFETOLOGY - What happened in the past 30 years and what may happen in the next 30 years. *Sensors and Actuators B-Chemical* 2003, 88, 1-20.

119. Bergveld, P., Development of an ion-sensitive solid-state device for neurophysiological measurements. *Ieee Transactions on Biomedical Engineering* 1970, BM17, 70-&.

120. Sobczynska, D.; Torbicz, W., ZrO2 gate pH-sensitive field-effect transistor. *Sensors and Actuators* 1984, 6, 93-105.

121. Duroux, P.; Emde, C.; Bauerfeind, P.; Francis, C.; Grisel, A.; Thybaud, L.; Armstrong, D.; Depeursinge, C.; Blum, A. L., The ion sensitive field-effect transistor (ISFET) pH electrode-A new sensor for long-term ambulatory pH monitoring. *Gut* 1991, 32, 240-245.

122. Oyama, N.; Hirokawa, T.; Yamaguchi, S.; Ushizawa, N.; Shimomura, T., Hydrogen-ion selective microelectrode prepared by modifying an electrode with polymers. *Analytical Chemistry* 1987, 59, 258-262.

123. Caflisch, C. R.; Pucacco, L. R.; Carter, N. W., Manufacture and utilization of antimony pH electrodes. *Kidney International* 1978, 14, 126-141.

124. Caldwell, P. C., Studies on the internal pH of large muscle and nerve fibres. *Jour Physiol* 1958, 142, 22-62.

125. Sjoberg, F.; Nilsson, G.; Gustafsson, U., New approach for elucidating the oxygen sensitivity and calibration of the antimony electrode. *Medical & Biological Engineering & Computing* 1997, 35, 207-210.

126. Kinoshita, E.; Ingman, F.; Edwall, G.; Thulin, S.; Glab, S., Polycristalline ans monocristalline antimony, iridium and palladium as electrode material for pH-sensing electrodes. *Talanta* 1986, 33, 125-134.

127. Glab, S.; Edwall, G.; Jongren, P. A.; Ingman, F., Effects of some complex-forming ligands on potential of antimony pH-sensors. *Talanta* 1981, 28, 301-311.

128. Pandolfino, J. E.; Ghosh, S.; Zhang, Q.; Heath, M.; Bombeck, T.; Kahrilas, P. J., Slimline vs. glass pH electrodes: what degree of accuracy should we expect? *Alimentary Pharmacology & Therapeutics* 2006, 23, 331-340.

129. Ha, Y.; Wang, M., Capillary melt method for micro antimony oxide pH electrode. *Electroanalysis* 2006, 18, 1121-1125.

130. Ha, Y.; Wang, M., An antimony oxide pH electrode for tissue culture medium. *Rare Metal Materials and Engineering* 2006, 35, 261-263.

131. Horrocks, B. R.; Mirkin, M. V.; Pierce, D. T.; Bard, A. J.; Nagy, G.; Toth, K., Scanning Electrochemical Microscopy. 19. Ion-selective potentiometric microscopy. *Analytical Chemistry* 1993, 65, 1213-1224.

132. Toth, K.; Nagy, G.; Wei, C.; Bard, A. J., Novel application of potentiometric microelectrodes-Scanning potentiometric microscopy. *Electroanalysis* 1995, 7, 801-810.

133. Honda, T.; Murase, K.; Hirato, T.; Awakura, Y., pH measurement in the vicinity of a cathode evolving hydrogen gas using an antimony microelectrode. *Journal of Applied Electrochemistry* 1998, 28, 617-622.

134. Murase, K.; Honda, T.; Hirato, T.; Awakura, Y., Measurement of pH in the vicinity of a cathode during the chloride electrowinning of nickel. *Metallurgical and Materials Transactions B-Process Metallurgy and Materials Processing Science* 1998, 29, 1193-1198.

135. Higashi, K.; Fukushima, H.; Urakawa, T.; Adaniya, T.; Matsudo, K., Mechanism of the electrodeposition of Zinc-alloys containing a small amount of cobalt. *J. Electrochem. Soc.* 1981, 128, 2081-2085.

136. Antonenko, Y. N.; Bulychev, A. A., Measurement of local pH changes near bilayer lipid-membrane by means of a pH microelectrode and a protonophore-dependent membrane potential-Comparison of the methods. *Biochimica Et Biophysica Acta* 1991, 1070, 279-282.

137. Ogata, Y.; Uchiyama, S.; Hayashi, M.; Yasuda, M.; Hine, F., Studies of the pH of the membrane-surface in a laboratory chloralkali cell. *Journal of Applied Electrochemistry* 1990, 20, 555-558.

138. Izquierdo, J.; Nagy, L.; Varga, A.; Santana, J. J.; Nagy, G.; Souto, R. M., Spatially resolved measurement of electrochemical activity and pH distributions in corrosion processes by scanning electrochemical microscopy using antimony microelectrode tips. *Electrochimica Acta* 2011, 56, 8846-8850.

139. Izquierdo, J.; Nagy, L.; Santana, J. J.; Nagy, G.; Souto, R. M., A novel microelectrochemical strategy for the study of corrosion inhibitors employing the scanning vibrating electrode technique and dual potentiometric/amperometric operation in scanning electrochemical microscopy: Application to the study of the cathodic inhibition by benzotriazole of the galvanic corrosion of copper coupled to iron. *Electrochimica Acta* 2011, 58, 707-716.

140. Izquierdo, J.; Nagy, L.; Bitter, I.; Souto, R. M.; Nagy, G., Potentiometric scanning electrochemical microscopy for the local characterization of the electrochemical behaviour of magnesium-based materials. *Electrochimica Acta* 2013, 87, 283-293.

141. Marzouk, S. A. M.; Ufer, S.; Buck, R. P.; Johnson, T. A.; Dunlap, L. A.; Cascio, W. E., Electrodeposited iridium oxide pH electrode for measurement of extracellular myocardial acidosis during acute ischemia. *Analytical Chemistry* 1998, 70, 5054-5061.

142. Shao, M. H.; Huang, R. S.; Fu, Y.; Hu, R. G.; Lin, C. J., Investigation on the formation mechanism of Ce conversion films on 2024 aluminum alloy. *Acta Physico-Chimica Sinica* 2002, 18, 791-795.

143. Chen, D. C.; Zhen, J. S.; Fu, C. Y., Preparation of Ir/IrOx pH electrode based on melt-oxidation and its response mechanism investigation. *Transactions of Nonferrous Metals Society of China* 2003, 13, 1459-1464.

144. Quan, H. M.; Kim, W.; Chung, K. C.; Park, J. M., Surface renewable hydrogen ion-selective polymeric composite electrode containing iridium oxide. *Bulletin of the Korean Chemical Society* 2005, 26, 1565-1568.

145. Korotcov, A.; Huang, Y. S.; Tsai, D. S.; Tiong, K. K., Growth and characterization of well aligned densely packed IrO2 nanocrystals on sapphire via reactive sputtering. *Journal of Physics-Condensed Matter* 2006, 18, 1121-1136.

146. Chen, C. A.; Chen, Y. M.; Huang, Y. S.; Tsai, D. S.; Tiong, K. K.; Du, C. H., Growth and characterization of V-shaped IrO(2) nanowedges via metal-organic vapor deposition. *Nanotechnology* 2008, 19.

147. Martinez, C. C. M.; Madrid, R. E.; Felice, C. J., Electrochemical and geometrical characterization of iridium oxide electrodes in stainless steel substrate. *Sensors and Actuators B-Chemical* 2008, 133, 682-686.

148. Wipf, D. O.; Ge, F. Y.; Spaine, T. W.; Bauer, J. E., Microscopic measurement of pH with iridium oxide microelectrodes. *Analytical Chemistry* 2000, 72, 4921-4927.

149. Bezbaruah, A. N.; Zhang, T. C., Fabrication of anodically electrodeposited iridium oxide film pH microelectrodes for microenvironmental studies. *Analytical Chemistry* 2002, 74, 5726-5733.

150. Nadappuram, B. P.; McKelvey, K.; Al Botros, R.; Colburn, A. W.; Unwin, P. R., Fabrication and Characterization of Dual Function Nanoscale pH-Scanning Ion Conductance Microscopy (SICM) Probes for High Resolution pH Mapping. *Analytical chemistry* 2013, 85.

151. Tolosa, V. M.; Wassum, K. M.; Maidment, N. T.; Monbouquette, H. G., Electrochemically deposited iridium oxide reference electrode integrated with an electroenzymatic glutamate sensor on a multielectrode array microprobe. *Biosensors & Bioelectronics* 2013, 42, 256-260.

152. Fog, A.; Buck, R. P., Electronic semiconducting oxides as pH sensors. *Sensors and Actuators* 1984, 5, 137-146.

153. Vanhoudt, P.; Lewandowski, Z.; Little, B., Iridium oxide pH microelectrode. *Biotechnology and Bioengineering* 1992, 40, 601-608.

154. da Silva, G. M.; Lemos, S. G.; Pocrifka, L. A.; Marreto, P. D.; Rosario, A. V.; Pereira, E. C., Development of low-cost metal oxide pH electrodes based on the polymeric precursor method. *Analytica Chimica Acta* 2008, 616, 36-41.

155. Ges, I. A.; Ivanov, B. L.; Schaffer, D. K.; Lima, E. A.; Werdich, A. A.; Baudenbacher, F. J., Thin-film IrOx pH microelectrode for microfluidic-based microsystems. *Biosensors & Bioelectronics* 2005, 21, 248-256.

156. Suzuki, H.; Morimoto, K., Micro analysis system for pH and protease activities with an integrated sample injection mechanism. *Biosensors & Bioelectronics* 2006, 22, 86-93.

157. Colombo, C.; Kappes, T.; Hauser, P. C., Coulometric micro-titrator with a ruthenium dioxide pH-electrode. *Analytica Chimica Acta* 2000, 412, 69-75.

158. Koncki, R.; Mascini, M., Screen-printed ruthenium dioxide electrodes for pH measurements. *Analytica Chimica Acta* 1997, 351, 143-149.

159. Kreider, K. G.; Tarlov, M. J.; Cline, J. P., Sputtered thin-film pH electrodes of platinum, palladium, ruthenium and iridium oxides. *Sensors and Actuators B-Chemical* 1995, 28, 167-172.

160. Pocrifka, L. A.; Goncalves, C.; Grossi, P.; Colpa, P. C.; Pereira, E. C., Development of RuO2-TiO2 (70-30) mol% for pH measurements. *Sensors and Actuators B-Chemical* 2006, 113, 1012-1016.

161. Pan, C. W.; Chou, J. C.; Sun, T. P.; Hsiung, S. K., Development of the tin oxide pH electrode by the sputtering method. *Sensors and Actuators B-Chemical* 2005, 108, 863-869.

162. Pan, C. W.; Chou, J. C.; Sun, T. P.; Hsiung, S. K., Development of the real-time pH sensing system for array sensors. *Sensors and Actuators B-Chemical* 2005, 108, 870-876.

163. Yang, G. C.; Chou, J. C.; Sun, T. P.; Hsiung, S. K., Study on the multi-sensing system based on the tin oxide pH electrode. *Rare Metal Materials and Engineering* 2006, 35, 221-224.

164. Yamamoto, K.; Shi, G.; Zhou, T.; Xu, F.; Zhu, M.; Liu, M.; Kato, T.; Jin, J.-Y.; Jin, L., Solid-state pH ultramicrosensor based on a tungstic oxide film fabricated on a tungsten nanoelectrode and its application to the study of endothelial cells. *Analytica Chimica Acta* 2003, 480, 109-117.

165. Luo, J. L.; Lu, Y. C.; Ives, M. B., Microelectrodes for the study of localized corrosion. *J. Electroanal. Chem.* 1992, 326, 51-68.

166. Kolar, M.; Doliska, A.; Svegl, F.; Kalcher, K., Tungsten - Tungsten Trioxide Electrodes for the Long-term Monitoring of Corrosion Processes in Highly Alkaline Media and Concrete-based Materials. *Acta Chimica Slovenica* 2010, 57, 813-820.

167. Dimitrakopoulos, L. T.; Dimitrakopoulos, T.; Alexander, P. W.; Logic, D.; Hibbert, D. B., A tungsten oxide coated wire electrode used as a pH sensor in flow injection potentiometry. *Analytical Communications* 1998, 35, 395-398.

168. Kriksunov, L. B.; Macdonald, D. D.; Millett, P. J., Tungsten tungsten-oxide pH sensing electrode for high-temperature aqueous environments. *J. Electrochem. Soc.* 1994, 141, 3002-3005.

169. Lima, A. C.; Jesus, A. A.; Tenan, M. A.; Silva, A.; Oliveira, A. F., Evaluation of a high sensitivity PbO2 pH-sensor. *Talanta* 2005, 66, 225-228.

170. Razmi, H.; Heidari, H.; Habibi, E., pH-sensing properties of PbO2 thin film electrodeposited on carbon ceramic electrode. *Journal of Solid State Electrochemistry* 2008, 12, 1579-1587.

171. Eftekhari, A., pH sensor based on deposited film of lead oxide on aluminum substrate electrode. *Sensors and Actuators B-Chemical* 2003, 88, 234-238.

172. Liu, C. C.; Bocchicchio, B. C.; Overmyer, P. A.; Neuman, M. R., Palladium-palladium oxide miniature pH electrode. *SCIENCE* 1980, 207, 188-189.

173. Kim, J. Y.; Lee, Y. H., Pd-PdO pH microprobe for local pH measurements. *Biotechnology and Bioengineering* 1989, 34, 131-136.

174. Grubb, W. T.; King, L. H., Palladium-palladium oxide pH electrodes. *Analytical Chemistry* 1980, 52, 270-273.

175. Kinoshita, E.; Ingman, F.; Edwall, G.; Glab, S., An examination of the palladium-palladium oxide system and its utility for pH-sensing electrodes. *Electrochimica Acta* 1986, 31, 29-38.

176. Bloor, L. J.; Malcolmelawes, D. J., An electrochemical preparation of palaldium oxide pH sensors. *J. Electroanal. Chem.* 1990, 278, 161-173.

177. Lewis, F. A.; Magennis, J. P.; McKee, S. G.; Ssebuwufu, P. J. M., Hydrogen chemical potentials and diffusion coefficients in hydrogen diffusion membranes. *Nature* 1983, 306, 673-675.

178. Lewis, F. A.; Kandasamy, K.; Baranowski, B., The uphill diffusion of hydrogen - Strain-gradient-induced effects in palladium alloy membranes. *International Journal of Hydrogen Energy* 1988, 13, 439-442.

179. Flanagan, T. B.; Oates, W. A., The palladium-hydrogen system. *Annual Review of Materials Science* 1991, 21, 269-304.

180. Lukaszewski, M.; Czerwinski, A., The method of limited volume electrodes as a tool for hydrogen electrosorption studies in palladium and its alloys. *Journal of Solid State Electrochemistry* 2011, 15, 2489-2522.

181. Fernandez, M. B.; Tonetto, G. M.; Crapiste, G. H.; Ferreira, M. L.; Damiani, D. E., Hydrogenation of edible oil over Pd catalysts: A combined theoretical and experimental study. *Journal of Molecular Catalysis a-Chemical* 2005, 237, 67-79.

182. Korin, E.; Soifer, L.; Mogilyanski, D.; Bettelheim, A., Preparation of a novel Pd hydride electrode based on polymer embedded nanosized Pd incorporated in porous carbon substrate. *Electrochemical and Solid State Letters* 2004, 7, A484-A487.

183. Blagojević, V. A.; Minić, D. J.; Novakovic, J. C.; Minic, D. M., Hydrogen Energy - Challenges and Perspectives. In *Hydrogen Economy: Modern Concepts, Challenges and Perspectives*, Minic, P. D., Ed. InTech: Serbia, 2012.

184. Züttel, A., Materials for hydrogen storage. *Materials Today* 2003, 6, 24-33.

185. Barton, J. C.; Lewis, F. A., Determination of the hydrogen content of palladium and palladium alloys from measurements of electrode potential and electrical resistance: A review. *Talanta* 1963, 10, 237-246.

186. Grden, M.; Kotowski, J.; Czerwinski, A., The study of electrochemical palladium behavior using the quartz crystal microbalance - II. Basic solutions. *Journal of Solid State Electrochemistry* 2000, 4, 273-278.

187. Grden, M.; Kotowski, J.; Czerwinski, A., Study of electrochemical palladium behavior by the quartz crystal microbalance. I. Acidic solutions. *Journal of Solid State Electrochemistry* 1999, 3, 348-351.

188. Lukaszewski, M.; Czerwinski, A., Electrochemical quartz crystal microbalance study on carbon oxides adsorption in the presence of electrosorbed hydrogen on Pd alloys with Pt and Rh. *Electrochimica Acta* 2006, 51, 4728-4735.

189. Grasjo, L.; Seo, M., Measurement of absorption of hydrogen and deuterium into palladium during electrolysis by a quartz crystal microbalance. *J. Electroanal. Chem.* 1990, 296, 233-239.

190. Gabrielli, C.; Grand, P. P.; Lasia, A.; Perrot, H., Study of the hydrogen/palladium system by fast quartz microbalance techniques. *Electrochimica Acta* 2002, 47, 2199-2207.

191. Rose, A.; Maniguet, S.; Mathew, R. J.; Slater, C.; Yao, J.; Russell, A. E., Hydride phase formation in carbon supported palladium nanoparticle electrodes investigated using in situ EXAFS and XRD. *Phys. Chem. Chem. Phys.* 2003, 5, 3220-3225.

192. Zhang, W. S.; Zhang, Z. F.; Zhang, Z. L., Some problems on the resistance method in the in situ measurement of hydrogen content in palladium electrode. *J. Electroanal. Chem.* 2002, 528, 1-17.

193. Vasile, M. J.; Enke, C. G., The Preparation and Thermodynamic Properties of a Palladium-Hydrogen Electrode. *J. Electrochem. Soc.* 1965, 112, 865-870

194. Dobson, J. V., Potentials of palladium hydride reference electrode between 25 degrees and 195 degrees C. *J. Electroanal. Chem.* 1972, 35, 129-135.

195. Dobson, J. V.; Snodin, P. R.; Thirsk, H. R., EMF-Measurement of cells employing metal-metal oxide electrodes in aqueous chloride and sulfate electrolytes at temperatures between 25-250 degrees C. *Electrochimica Acta* 1976, 21, 527-533.

196. Goffe, R. A.; Tseung, A. C., Internally charged palladium hydride reference electrode. 1. Effect of charging current-density on long-term stability. *Medical & Biological Engineering & Computing* 1978, 16, 670-676.

197. Kelly, J. F. D.; Goffe, R. A.; Tseung, A. C. C., Internally charged palladium hydride reference electrode. 2. Automatically controlled palladium hydride electrode. *Medical & Biological Engineering & Computing* 1981, 19, 333-339.

198. Webster, T. A.; Goluch, E. D., Electrochemical detection of pyocyanin in nanochannels with integrated palladium hydride reference electrodes. *Lab on a Chip* 2012, 12, 5195-5201.

199. Macdonald, D. D.; Wentrcek, P. R.; Scott, A. C., The measurement of pH in aqueous systems at elevated temperatures using palladium hydride electrodes. *J. Electrochem. Soc.* 1980, 127, 1745-1751.
200. Schwing, J. P.; Rogers, L. B., Comparison of different palladium-hydrogen electrodes as pH indicators. *Analytica Chimica Acta* 1956, 15, 379-388.
201. Stock, J. T.; Purdy, W. C.; Williams, T. R., The palladium electrode in aqueous and nonaqueous titrimetry. *Analytica Chimica Acta* 1959, 20, 73-78.
202. Jasinski, R., Palaldium hydride pH electrode for use in buffered fluoride etch solutions. *J. Electrochem. Soc.* 1974, 121, 1579-1584.
203. Tsuruta, T.; Macdonald, D. D., Measurement of pH and redox potential in boric-acid lithium hydroxide buffer solutions at elevated temperatures. *J. Electrochem. Soc.* 1981, 128, 1199-1203.
204. Dobson, J. V.; Brims, G., The measurement by the (alpha+beta) palladium hydride electrode of the approximate pH of phosphate and acetate buffer solution at elevated temperatures and pressures. *Electrochimica Acta* 1987, 32, 149-153.
205. Wolfe, R. C.; Weil, K. G.; Shaw, B. A.; Pickering, H. W., Measurement of pH gradients in the crevice corrosion of iron using a palladium hydride microelectrode. *J. Electrochem. Soc.* 2005, 152, B82-B88.
206. Imokawa, T.; Williams, K. J.; Denuault, G., Fabrication and characterization of nanostructured Pd hydride pH microelectrodes. *Analytical Chemistry* 2006, 78, 265-271.
207. Fleischmann, M.; Hiddleston, J. N., A palladium-hydrogen probe electrode for use as a microreference electrode. *journal of physics e scientific instruments* 1968, 1, 667-668.
208. Lasia, A., On the mechanism of the hydrogen absorption reaction. *J. Electroanal. Chem.* 2006, 593, 159-166.
209. Lynch, J. F.; Flanagan, T. B., Investigation of dynamic equilibrium between chemisorbed and absorbed hydrogen in palladium-hydrogen system. *Journal of Physical Chemistry* 1973, 77, 2628-2634.
210. Duncan, H.; Lasia, A., Mechanism of hydrogen adsorption/ab sorption at thin Pd layers on Au(111). *Electrochimica Acta* 2007, 52, 6195-6205.
211. Birry, L.; Lasia, A., Effect of crystal violet on the kinetics of H sorption into Pd. *Electrochimica Acta* 2006, 51, 3356-3364.
212. Mitsui, T.; Rose, M. K.; Fomin, E.; Ogletree, D. F.; Salmeron, M., Dissociative hydrogen adsorption on palladium requires aggregates of three or more vacancies. *Nature* 2003, 422, 705-707.
213. Bartlett, P. N.; Gollas, B.; Guerin, S.; Marwan, J., The preparation and characterisation of H-1-e palladium films with a regular hexagonal nanostructure formed by electrochemical deposition from lyotropic liquid crystalline phases. *Phys. Chem. Chem. Phys.* 2002, 4, 3835-3842.
214. Grden, M.; Lukaszewski, M.; Jerkiewicz, G.; Czerwinski, A., Electrochemical behaviour of palladium electrode: Oxidation, electrodissolution and ionic adsorption. *Electrochimica Acta* 2008, 53, 7583-7598.
215. Baldauf, M.; Kolb, D. M., A hydrogen adsorption and absorption study with ultrathin Pd overlayers on Au(111) and Au(100). *Electrochimica Acta* 1993, 38, 2145-2153.
216. Baldauf, M.; Kolb, D. M., Formic acid oxidation on ultrathin Pd films on Au(hkl) and Pt(hkl) electrodes. *Journal of Physical Chemistry* 1996, 100, 11375-11381.
217. Czerwinski, A.; Marassi, R.; Zamponi, S., The absorption of hydrogen and deuterium in thin palladium electrodes. 1. Acidic solutions. *J. Electroanal. Chem.* 1991, 316, 211-221.

218. Czerwinski, A.; Kiersztyn, I.; Grden, M., The study of hydrogen sorption in palladium limited volume electrodes (Pd-LVE) - Part II. Basic solutions. *J. Electroanal. Chem.* 2000, 492, 128-136.

219. Koss, U.; Lukaszewski, M.; Hubkowska, K.; Czerwinski, A., Influence of rhodium additive on hydrogen electrosorption in palladium-rich Pd-Rh alloys. *Journal of Solid State Electrochemistry* 2011, 15, 2477-2487.

220. Attard, G. S.; Bartlett, P. N.; Coleman, N. R. B.; Elliott, J. M.; Owen, J. R.; Wang, J. H., Mesoporous platinum films from lyotropic liquid crystalline phases. *SCIENCE* 1997, 278, 838-840.

221. Marwan, J. The electrodeposition and electrochemical properties of nanostructured (H_1-e) metal films. PhD, University of Southampton, Southampton, 2002.

222. Bartlett, P. N.; Marwan, J., The effect of surface species on the rate of H sorption into nanostructured Pd. *Phys. Chem. Chem. Phys.* 2004, 6, 2895-2898.

223. Denuault, G.; Milhano, C.; Pletcher, D., Mesoporous palladium - the surface electrochemistry of palladium in aqueous sodium hydroxide and the cathodic reduction of nitrite. *Phys. Chem. Chem. Phys.* 2005, 7, 3545-3551.

224. Duncan, H.; Lasia, A., Hydrogen adsorption/absorption on Pd/Pt(111) multilayers. *J. Electroanal. Chem.* 2008, 621, 62-68.

225. Duncan, H.; Lasia, A., Separation of hydrogen adsorption and absorption on Pd thin films. *Electrochimica Acta* 2008, 53, 6845-6850.

226. Zhang, W. S.; Zhang, X. W.; Zhao, X. G., Voltammograms of thin layer Pd vertical bar H(D) electrodes in the coexistence of alpha and beta phases. *J. Electroanal. Chem.* 1998, 458, 107-112.

227. Lee, J. W.; Pyun, S. I., Anomalous behaviour of hydrogen extraction from hydride-forming metals and alloys under impermeable boundary conditions. *Electrochimica Acta* 2005, 50, 1777-1805.

228. Lukaszewski, M.; Grden, M.; Czerwinski, A., Hydrogen electrosorption in Pd-Pt-Rh alloys. *J. Electroanal. Chem.* 2004, 573, 87-98.

229. Rosamilia, J. M.; Abys, J. A.; Miller, B., Electrochemical hydrogen insertion into palladium and palladium nickel thin-films. *Electrochimica Acta* 1991, 36, 1203-1208.

230. Lewis, F. A., *The palladium hydrogen system*. Academic Press: London, 1967.

231. Aben, P. C.; Burgers, W. G., Surface structure and electrochemical potential of palladium while absorbing hydrogen in aqueous solution 1962, 58, 1989-1992.

232. Amemiya, S.; Bard, A. J.; Fan, F. R. F.; Mirkin, M. V.; Unwin, P. R., Scanning Electrochemical Microscopy. *Annual Review of Analytical Chemistry* 2008, 1, 95-131.

233. Bard, A. J.; Denuault, G.; Lee, C.; Mandler, D.; Wipf, D. O., Scanning electrochemical microscopy - A new tecnique for the characterization and modification of surfaces. *Accounts of Chemical Research* 1990, 23, 357-363.

234. Baltes, N.; Heinze, J., Imaging Local Proton Fluxes through a Polycarbonate Membrane by Using Scanning Electrochemical Microscopy and Functionalized Alkanethiols. *Chemphyschem* 2009, 10, 174-179.

235. Bard, A. J.; Fan, F. R. F.; Kwak, J.; Lev, O., Scanning electrochemical microscopy - Introduction and principles. *Analytical Chemistry* 1989, 61, 132-138.

236. Kwak, J.; Bard, A. J., Scanninc electrochemical microscopy - Theory of the feedback mode. *Analytical Chemistry* 1989, 61, 1221-1227.

237. Kwak, J.; Bard, A. J., Scanning electrochemical microscopy - Apparatus and two-dimentional scans of conductive and insulating substrates. *Analytical Chemistry* 1989, 61, 1794-1799.

238. Engstrom, R. C.; Strasser, V. A., Characterization of electrochemically pretreated glassy-carbon electrodes. *Analytical Chemistry* 1984, 56, 136-141.

239. Engstrom, R. C.; Weber, M.; Werth, J., Distribution of electrochemical activity on graphite epoxy surfaces. *Analytical Chemistry* 1985, 57, 933-936.

240. Engstrom, R. C.; Weber, M.; Wunder, D. J.; Burgess, R.; Winquist, S., Measurements within the diffusion layer using a microelectrode probe. *Analytical Chemistry* 1986, 58, 844-848.

241. Engstrom, R. C.; Meaney, T.; Tople, R.; Wightman, R. M., Spatiotemporal description of the diffusion layer with a microelectrode probe. *Analytical Chemistry* 1987, 59, 2005-2010.

242. Liu, H. Y.; Fan, F. R. F.; Lin, C. W.; Bard, A. J., Scanning electrochemical and tunneling ultramicroelectrode microscope for high-resolution examination of electrode surfaces in solution. *Journal of the American Chemical Society* 1986, 108, 3838-3839.

243. Evans, S. A. G.; Brakha, K.; Billon, M.; Mailley, P.; Denuault, G., Scanning electrochemical microscopy (SECM): localized glucose oxidase immobilization via the direct electrochemical microspotting of polypyrrole-biotin films. *Electrochem. Commun.* 2005, 7, 135-140.

244. Horrocks, B. R.; Schmidtke, D.; Heller, A.; Bard, A. J., Scanning electrochemical microscopy. 24. Enzyme ultramicroelectrodes for the measurement of hydrogen-peroxide at surfaces. *Analytical Chemistry* 1993, 65, 3605-3614.

245. Shao, Y. H.; Mirkin, M. V.; Fish, G.; Kokotov, S.; Palanker, D.; Lewis, A., Nanometer-sized electrochemical sensors. *Analytical Chemistry* 1997, 69, 1627-1634.

246. Yang, Y. F.; Denuault, G., Scanning electrochemical microscopy (SECM): study of the formation and reduction of oxides on platinum electrode surfaces in Na2SO4 solution (pH=7). *J. Electroanal. Chem.* 1998, 443, 273-282.

247. Yang, Y. F.; Denuault, G., Scanning electrochemical microscopy (SECM) study of pH changes at Pt electrode surfaces in Na2SO4 solution (pH 4) under potential cycling conditions. *Journal of the Chemical Society-Faraday Transactions* 1996, 92, 3791-3798.

248. Yang, Y.-F.; Denuault, G., Scanning electrochemical microscopy (SECM) : study of the adsorption and desorption of hydrogen on platinum electrodes in Na2SO4 solution (pH = 7). *J. Electroanal. Chem.* 1996, 418, 99-107.

249. Klusmann, E.; Schultze, J. W., pH-microscopy - theoretical and experimental investigations. *Electrochimica Acta* 1997, 42, 3123-3134.

250. Paik, C. H.; White, H. S.; Alkire, R. C., Scanning electrochemical microscopy detection of dissolved sulfur species from inclusions in stainless steel. *J. Electrochem. Soc.* 2000, 147, 4120-4124.

251. Hess, C.; Borgwarth, K.; Ricken, C.; Ebling, D. G.; Heinze, J., Scanning electrochemical microscopy: Study of silver deposition on non-conducting substrates. *Electrochimica Acta* 1997, 42, 3065-3073.

252. Ammann, E.; Mandler, D., Local deposition of gold on silicon by the scanning electrochemical microscope. *J. Electrochem. Soc.* 2001, 148, C533-C539.

253. Tel-Vered, R.; Bard, A. J., Generation and detection of single metal nanoparticles using scanning electrochemical microscopy techniques. *Journal of Physical Chemistry B* 2006, 110, 25279-25287.

254. Mandler, D.; Bard, A. J., A new approach to the high-resolution electodeposition of metals via the feedback mode of the scanning electrochemcial microscope. *J. Electrochem. Soc.* 1990, 137, 1079-1086.

255. Valenti, G.; Bardini, L.; Bonazzi, D.; Rapino, S.; Marcaccio, M.; Paolucci, F., Creation of Reactive Micro Patterns on Silicon by Scanning Electrochemical Microscopy. *Journal of Physical Chemistry C* 2010, 114, 22165-22170.

256. de Abril, O.; Mandler, D.; Unwin, P. R., Local cobalt electrodeposition using the scanning electrochemical microscope. *Electrochemical and Solid State Letters* 2004, 7, C71-C74.
257. Radtke, V.; Hess, C.; Souto, R. M.; Heinze, J., Electroless, electrolytic and galvanic copper deposition with the Scanning Electrochemical Microscope (SECM). *Zeitschrift Fur Physikalische Chemie-International Journal of Research in Physical Chemistry & Chemical Physics* 2006, 220, 393-406.
258. Radtke, V.; Hess, C.; Heinze, J., Metal deposition by inducing a microgalvanic cell with the scanning electrochemical microscope (SECM). *Zeitschrift Fur Physikalische Chemie-International Journal of Research in Physical Chemistry & Chemical Physics* 2007, 221, 1221-1236.
259. Malel, E.; Colleran, J.; Mandler, D., Studying the localized deposition of Ag nanoparticles on self-assembled monolayers by scanning electrochemical microscopy (SECM). *Electrochimica Acta* 2011, 56, 6954-6961.
260. Fedorov, R. G.; Mandler, D., Local deposition of anisotropic nanoparticles using scanning electrochemical microscopy (SECM). *Phys. Chem. Chem. Phys.* 2013, 15, 2725-2732.
261. Shohat, I.; Mandler, D., Deposition of nickel-hydroxide structures using the scanning electrochemical microscope. *J. Electrochem. Soc.* 1994, 141, 995-999.
262. Veleva, L.; Diaz-Ballote, L.; Wipf, D. O., An in situ electrochemical study of electrodeposited nickel and nickel-yttrium oxide composite using scanning electrochemical microscopy. *J. Electrochem. Soc.* 2003, 150, C1-C6.
263. Nowall, W. B.; Wipf, D. O.; Kuhr, W. G., Localized avidin/biotin derivatization of glassy carbon electrodes using SECM. *Analytical Chemistry* 1998, 70, 2601-2606.
264. Shiku, H.; Takeda, T.; Yamada, H.; Matsue, T.; Uchida, I., Microfabbrication and characterization of diaphorase-patterned surfaces by scanning electrochemical microscopy. *Analytical Chemistry* 1995, 67, 312-317.
265. Shiku, H.; Uchida, I.; Matsue, T., Microfabrication of alkylsilanized glass substrate by electrogenerated hydroxyl radical using scanning electrochemical microscopy. *Langmuir* 1997, 13, 7239-7244.
266. R. M. Souto, S. V. L. a. S. G., Microscopy: Science, Technology, Applications and Education. A. Méndez-Vilas and J. Díaz (Eds.) ed.; (Eds.), A. M.-V. a. J. D., Ed. Lisbon, 2010.
267. Macpherson, J. V.; Unwin, P. R., A novel-apprach to the study of dissolution kinetics using the scanning electrochemcial microscope-Theory and application to copper-sulfate pentahydrate dissolution in acqueous sulfuric-acid-solutions. *Journal of Physical Chemistry* 1994, 98, 1704-1713.
268. Macpherson, J. V.; Unwin, P. R., Oscillatory dissolution on an ionic single crystal surface observed with the scanning electrochemical microscope. *Journal of Physical Chemistry* 1994, 98, 11764-11770.
269. Macpherson, J. V.; Unwin, P. R., Scanning electrochemical microscope induced dissolution-rate law and reaction-rate imaging for dissolution of the (010) face of potassium ferrocyanide trihydrate in nonstoichiometric aqueous-solutions of the lattice ions. *Journal of Physical Chemistry* 1995, 99, 3338-3351.
270. Bard, A. J.; Mirkin, M. V., *Scanning Electrochemical Microscopy-Second Edition*. Taylor & Francis Group: Boca Raton, FL, 2012.
271. Csoka, B.; Mekhalif, Z., Carbon paste-based ion-selective dual function microelectrodes for SECM measurements. *Electrochimica Acta* 2009, 54, 3225-3232.
272. Tanabe, H.; Yamamura, Y.; Misawa, T., In situ ionic imaging for pitting corrosion sites on austenitic stainless steels with scanning electrochemical microscopy. In

Passivation of Metals and Semiconductors, Heusler, K. E., Ed. Transtec Publications Ltd: Zurich-Uetikon, 1995; Vol. 185-, pp 991-1000.

273. El-Giar, E.; Wipf, D. O., Microparticle-based iridium oxide ultramicroelectrodes for pH sensing and imaging. *J. Electroanal. Chem.* 2007, 609, 147-154.

274. Beynon, R.; Easterby, J. Buffers solutions: A recipe calculator for thermodynamically correct buffers for pH control. http://www.liv.ac.uk/buffers/buffercalc.html.

275. Bartlett, P. N., In *Biosensors: a pratical approach*, Oxford University Press: 1990; p 47.

276. Denuault, G., Microelectrodes. *Chemistry & Industry* 1996, 678-680.

277. Yasin, H. Controlled Electrodeposition of Metal Nanocentres for Catalysis. PhD, University of Southampton, Southampton, 2010.

278. Mitchell, D. J.; Tiddy, G. J. T.; Waring, L.; Bostock, T.; McDonald, M. P., Phase-behavior of polyoxyethylene surfactants with water - Mesophase structures and partial miscibility (cloud points). *Journal of the Chemical Society-Faraday Transactions I* 1983, 79, 975-1000.

279. Zhong, Y.; Xu, C. L.; Kong, L. B.; Li, H. L., Synthesis and high catalytic properties of mesoporous Pt nanowire array by novel conjunct template method. *Applied Surface Science* 2008, 255, 3388-3393.

280. Biegler, T.; Rand, D. A. J.; Woods, R., Limiting oxygen coverage on platinized platinum - Relevance to determination of real platinum area by hydrogen adsorption. *J. Electroanal. Chem.* 1971, 29, 269-&.

281. Rand, D. A. J.; Woods, R., Study of dissolution of platinum, palladium, rhodium and gold electrodes in 1 M sulfuric acid by cyclic voltammetry. *J. Electroanal. Chem.* 1972, 35, 209-218.

282. Popov, K. I.; Maksimovic, M. D.; Totovski, D. C.; Nakic, V. M., Some aspects of current density distribution in electrolytic cells. 1. Dendritic growth of cadmium at the cathode edge in galvanostatic electrodeposition. *Surface Technology* 1983, 19, 173-180.

283. Ives, D. J. G.; Janz, G. J., *Reference Electrodes*. Academic Press, New York: 1961.

284. Wolfe, R. C.; Weil, K. G.; Pickering, H. W., Electrochemical Probes for Metal/Electrolyte System Characterization during Crevice Corrosion†. *The Journal of Physical Chemistry B* 2004, 108, 14298-14304.

285. Imokawa, T. Fabrication and Characterization of Nanostructured Palladium Hydride Microelectrode pH Sensors. PhD, University of Southampton, Southampton, 2003.

286. Lukaszewski, M.; Grden, M.; Czerwinski, A., Comparative study on hydrogen electrosorption in palladium and palladium-noble metal alloys. *Journal of New Materials for Electrochemical Systems* 2006, 9, 409-417.

287. Lukaszewski, M.; Hubkowska, K.; Czerwinski, A., Comparative study on the influence of temperature, electrode potential and alloy bulk composition on hydrogen electrosorption into Pd-Pt and Pd-Au alloys. *J. Electroanal. Chem.* 2011, 651, 131-142.

288. Lukaszewski, M.; Hubkowska, K.; Czerwinski, A., Electrochemical absorption and oxidation of hydrogen on palladium alloys with platinum, gold and rhodium. *Phys. Chem. Chem. Phys.* 2010, 12, 14567-14572.

289. Lukaszewski, M.; Klimek, K.; Zurowski, A.; Kedra, T.; Czerwinski, A., Kinetics and mechanism of hydrogen electrosorption in palladium-based alloys. *Solid State Ionics* 2011, 190, 18-24.

290. Czerwinski, A.; Kiersztyn, I.; Grden, M., Temperature influence on hydrogen sorption in palladium limited-volume electrodes (Pd-LVE). *Journal of Solid State Electrochemistry* 2003, 7, 321-326.

291. Czerwinski, A.; Kiersztyn, I.; Grden, M.; Czapla, J., The study of hydrogen sorption in palladium limited volume electrodes (Pd-LVE) I. Acidic solutions. *J. Electroanal. Chem.* 1999, 471, 190-195.

292. Williams, K. J. Development of nanostructured palladium microelectrode for pH monitoring in scanning electrochemical microscopy. University of Southampton, 2008.

293. Flanagan, T. B.; Oates, W. A., The effect of hysteresis on the phase-diagram of Pd-H. *Journal of the Less-Common Metals* 1983, 92, 131-142.

294. Gabrielli, C.; Grand, P. P.; Lasia, A.; Perrot, H., Investigation of Hydrogen Adsorption and Absorption in Palladium Thin Films. *J. Electrochem. Soc.* 2004, 151, A1937-A1942.

295. Cornut, R.; Lefrou, C., A unified new analytical approximation for negative feedback currents with a microdisk SECM tip. *J. Electroanal. Chem.* 2007, 608, 59-66.

296. Burke, L. D.; Casey, J. K., The electrocatalytic behavior of palladium in acid and base. *Journal of Applied Electrochemistry* 1993, 23, 573-582.

297. Burke, L. D.; Casey, J. K., An examination of electrochemical-behaviour of palladium electrodes in acid. *J. Electrochem. Soc.* 1993, 140, 1284-1291.

298. Burke, L. D.; Casey, J. K., An examination of electrochemical-behaviour of palladium in base. *J. Electrochem. Soc.* 1993, 140, 1292-1298.

299. Birkin, P. R.; Elliott, J. M.; Watson, Y. E., Electrochemical reduction of oxygen on mesoporous platinum microelectrodes. *Chemical Communications* 2000, 1693-1694.

300. Power, G. P.; Ritchie, I. M., Mixed potential measurements in the elucidation of corrosion mechanisms. 1. Introductory theory. *Electrochimica Acta* 1981, 26, 1073-1078.

301. Selzer, Y.; Turyan, I.; Mandler, D., Studying heterogeneous catalysis by the scanning electrochemical microscope (SECM): The reduction of protons by methyl viologen catalyzed by a platinum surface. *Journal of Physical Chemistry B* 1999, 103, 1509-1517.

302. Park, J. H.; Zhou, H. J.; Percival, S. J.; Zhang, B.; Fan, F. R. F.; Bard, A. J., Open Circuit (Mixed) Potential Changes Upon Contact Between Different Inert Electrodes-Size and Kinetic Effects. *Analytical Chemistry* 2013, 85, 964-970.

303. Dole, M.; Wiener, B. Z., The Theory of the Glass Electrode. IV . Temperature Studies of the Glass Electrode Error. *J. Electrochem. Soc.* 1937, 72, 107-127.

304. Dobson, J. V., The Pallap Hode Electrode System. *Platinum Metals Review* 1981, 25, 72-73.

305. Parkhurst, D. L.; Appelo, C. A. J. *Description of input and examples for PHREEQC version 3—A computer program for speciation, batch-reaction, one-dimensional transport, and inverse geochemical calculations*; U.S. Geological Survey: Denver, 2013; p 497.

306. Cizer, O.; Rodriguez-Navarro, C.; Ruiz-Agudo, E.; Elsen, J.; Van Gemert, D.; Van Balen, K., Phase and morphology evolution of calcium carbonate precipitated by carbonation of hydrated lime. *Journal of Materials Science* 2012, 47, 6151-6165.

307. http://mineral.gly.bris.ac.uk/AqueousGeochemistry/AAGPractical1.pdf.

308. www.geo.utexas.edu/courses/376m/PHREEQC%20Files/get_goin.pdf.

309. Gewirth, A. A.; Craston, D. H.; Bard, A. J., Fabrication and characterization of microtips for insitu scanning tunneling microscopy. *J. Electroanal. Chem.* 1989, 261, 477-482.

310. McHenry, E. J., *Electrochemica Tecnology* 1967, 5, 275.

311. Pletcher, D.; Sotiropoulos, S., Cathodic reduction of oxygen in water and media of low ionic-strength. *Journal of the Chemical Society-Faraday Transactions* 1995, 91, 457-462.

312. Pauporte, T.; Lincot, D., Hydrogen peroxide oxygen precursor for zinc oxide electrodeposition I. Deposition in perchlorate medium. *J. Electrochem. Soc.* 2001, 148, C310-C314.
313. Nobial, M.; Devos, O.; Mattos, O. R.; Tribollet, B., The nitrate reduction process: A way for increasing interfacial pH. *J. Electroanal. Chem.* 2007, 600, 87-94.
314. Therese, G. H. A.; Kamath, P. V., Cathodic reduction of different metal salt solutions Part I: synthesis of metal hydroxides by electrogeneration of base. *Journal of Applied Electrochemistry* 1998, 28, 539-543.
315. Klein, D. H.; Smith, M. D., Homogeneous nucleation of calcium hydroxide. *Talanta* 1968, 15, 229-&.
316. Cadle, S. H.; Bruckenstein, S., Ring-disk electrode study of the anodic behavior of gold in 0.2M sulfuric acid. *Analytical Chemistry* 1974, 46, 16-20.